Machine Learning Algorithms and Molecular Dynamics Models for Predicting Nano-scale and Bulk Thermal Properties

by

Vahid Rashidi

A dissertation submitted in partial fulfillment
of the requirements for the degree of
Doctor of Philosophy
(Mechanical Engineering)
in the University of Michigan
2018

Doctoral Committee:

Professor Kevin P. Pipe, Chair
Professor John Kieffer
Professor Katsuo Kurabayashi
Associate Professor Pramod Sangi Reddy

Vahid Rashidi

vrashidi@umich.edu

ORCID iD: 0000-0003-0507-006X

To My Parents

ACKNOWLEDGEMENTS

First and foremost I would like to thank my advisor Prof. Kevin Pipe. I am really grateful for all the support he has provided me these past few years. Without his support, I might not have been able to work on the research topics that I am very passionate about. He is very encouraging and supportive of new research ideas, which I have found very critical for developing an entrepreneurial mindset.

I would like to thank the distinguished members of my committee, Prof. John Kieffer, Prof. Pramod Reddy, and Prof. Katsuo Kurabayashi. I have learned a lot from each one of them over the past few years, either in classes I took with them or from scientific discussions we had. It has been an honor to know them, and I am very grateful to have had the opportunity of working with them. This thesis would not have been possible without their help and scientific knowledge.

Next, I would like to thank my parents, my wife, and my siblings who have given me their unconditional support during my studies. I am very grateful for each and everyone of them. Their presence makes my life so much better.

I would like to thank all of my lab-mates, current and past, that have made this journey much fun. I am really grateful for all the scientific conversations we have had and all of the help they have provided to me during my studies.

I would like to thank my friends who have supported me, helped me, and guided me throughout my journey so far.

Finally, I want to thank all the people whose support made this research possible.

TABLE OF CONTENTS

LIST OF FIGURES

Figure

LIST OF TABLES

Table

LIST OF APPENDICES

Appendix

ABSTRACT

The engineering of nano-scale thermal transport mechanisms in a material can strongly influence its macro-scale behavior, with important implications for many thermal management applications. Atomistic computational methods in which the motion of individual atoms can be tracked offer a powerful means to study these mechanisms in circumstances for which performing experiments is challenging or impractical.

In this thesis, we first apply computational methods to study nano-scale heat transfer at strained interfaces between crystalline semiconductor structures. Such interfaces are important because of their applications in strained silicon transistors, thermoelectric materials, and lattice-mismatched epitaxial structures that are important for emerging applications (e.g., GaN on silicon). The strain at the interface disturbs the local lattice structure, which in turn alters phonon properties. We find that interfacial bonds between silicon and germanium atoms in a superlattice structure can introduce new vibrational modes in the system that reduce the interface thermal boundary resistance.

We then examine the relationships between bonding and thermal properties in the context of polymer chains, where inefficient inter-chain thermal coupling presents a bottleneck to macro-scale heat transfer. We consider various bonding/interaction types including covalent bonds, vdW and electrostatic interactions, and ionic interactions. We find that non-bonding interactions can have a significant impact on heat transfer in crosslinked polymers. For example, short crosslinkers can bring chains closer to each other and thereby increase inter-chain thermal conductance by non-bonding interactions. The understanding we gain by computational analysis is shown

to resolve literature discrepancies regarding the effects of crosslinkers on heat transfer in polymers.

Finally, we develop a machine learning framework to compute the complex underlying relationships between a materials basic physical properties (e.g., lattice structure), its local environmental properties (e.g., temperature), and its thermal properties. Our results show a ∼five-fold reduction in simulation time versus current methods such as molecular dynamics or density functional theory. We also show how physical rules may be encoded in this and similar algorithms for materials property prediction such that the algorithm is not allowed to explore function spaces where physical rules do not hold. This inclusion of physical rules in the algorithm reduces the amount of data needed to train the algorithm, with broad applicability to machine learning of other material properties for which the feature size is large relative to available training data. These finding and models could pave the way toward more rapid design of engineered materials with desired thermal, mechanical, and electrical properties.

CHAPTER I

Background on Nano-scale Heat Transfer

The past few decades have been very fruitful for several industries, in particular for the electronics industry and the polymer industry. Evidence for this can be seen in the development of powerful computer processors based on nano-size silicon transistors that can handle computations up to several Gigahertz (GHz). However, in areas such as silicon electronics, advances are becoming increasingly difficult because of material limitations and design challenges. High power density in small-scale devices is one of these challenges that leads to high device temperatures [110, 127]. High device temperatures due to Joule heating that results from electrical currents in devices such as transistors and light emitters is a significant roadblock to further size reduction, performance improvement, reliability, and energy efficiency. In order to overcome these challenges, understanding the heat transfer mechanisms at different length-scales and materials is crucially important. This understanding will help us to design advanced materials with desired properties to tackle these challenges. These advanced materials could take the form of either completely unprecedented materials or an engineered form of already existing materials.

Macro-scale heat transfer in materials happens through three different mechanisms, namely, conduction, convection, and radiation. First, convective heat transfer is the transport of energy through transport of bulk quantities of material. Second,

radiation is heat transfer though electromagnetic waves excited from the materials at temperatures above absolute zero Kelvin. Third, conduction is transport of energy through vibration of atoms around their equilibrium position or the movement of electrons in the material [61].

Conduction is the main heat transfer mechanism in electronic devices and most of materials in solid state at relatively low temperatures (300K). Thermal conductivity is a material property that measures the rate of heat conduction in the material. The most widely used equation to model 1D macro-scale conduction using thermal conductivity is known as Fourier's law of conduction (Equation 1.1) [61].

$$Q = k\frac{dT}{dx} \tag{1.1}$$

where Q is the heat flux through the material, k is thermal conductivity of the material, T is the temperature, and x is the longitudinal dimension.

Although this equation is very useful for macro-scale conduction, it breaks down for nano-scale conduction regimes, where the medium may not be considered continuous and thermal transport mechanisms transition to ballistic rather than diffusive. An example of this break down is in silicon nanowires [134] or single chain polymers [133], where the length of the wire becomes comparable to the mean free path of phonons, wave like motion of atoms around their equilibrium positions. Thus, understanding the nano-size effects on heat transfer in materials becomes increasingly important for nano-engineering of materials for electronic devices.

Two major classes of electronic devices can be defined: those based on crystalline semiconductors that form covalent bonds between their atoms (e.g., silicon, germanium, and gallium arsenide), and those based on organic semiconductors (e.g., conducting polymers and small-molecules). Each of these classes of devices has its own thermal challenges. Inorganic semiconductor materials typically have relatively high thermal conductivity. Thus, devices made of inorganic semiconductors are often

capable of operating at high powers and/or high frequencies [119]. These devices usually have at least one nano-size dimension. In general, as the size of devices gets smaller, the heat flux (heat transfer per area) through them gets larger, which leads to high temperatures. Additionally, many of these devices include complex hetero-structures in which numerous layers are sandwiched together, leading to numerous interfaces [171]. This large number of interfaces could lead to a large net thermal resistance. On the other hand, polymers (usually used for low power and low frequency applications) suffer from an inherently low thermal conductivity. Most polymers have a thermal conductivity on the order of 0.1 W/mK [60, 78]. This low thermal conductivity has limited their applications in certain areas. A enhancement in thermal conductivity of certain polymers could improve their application in plastics industry [202] and photovoltaic applications [55].

In this thesis, numerical methods are used to study nano-scale heat transfer in materials in order to better understand heat transfer at the interface of crystalline semiconductor materials as well as heat transfer in polymers. This understanding will allow us to design high thermal conductivity polymers that can be used in plastics industry or organic electronic devices. Furthermore, to overcome some of the challenges associated with time consuming numerical methods used in study of thermal conductivity, machine learning algorithms are developed as another tool for calculating thermal properties of materials at a much faster pace. In addition to enabling us to more rapidly predict material properties, these algorithms allow us to better understand the relationships between thermal conductivity and other material properties.

1.1 Nano-scale Heat Transfer and Numerical Methods

Thermal transport plays an important role in the performance of many devices. For example, as shown in Equation 1.2, the figure of merit (ZT, which shows the

energy conversion efficiency of the device) of thermoelectric devices, which directly convert thermal energy to electricity, is inversely related to the thermal conductivity of a material. This relation shows that to achieve a higher figure of merit for thermoelectric materials, a lower thermal conductivity is required [80].

$$ZT = \frac{\sigma S^2 T}{k} \tag{1.2}$$

where ZT is the figure of merit of the thermoelectric device, σ is the electrical conductivity of the material, S is the Seebeck coefficient of the material (which is a measure of the thermoelectric voltage created between two points of a material in response to a 1K temperature difference imposed between those two points), T is the temperature at which the device is operating, and finally k is the thermal conductivity of the thermoelectric material.

Thermal transport impacts the design of other electronic devices. For example, in electronic switches, the rate of power consumption is related to the following parameters shown in the equation below [94].

$$P \propto CV^2 f \tag{1.3}$$

where P is the power dissipation of the device, C is the capacitance of the switch that is being turned on and off, V is the voltage at the device, and finally f is the frequency of switching. Based on Equation 1.3, increasing the switching frequency will increase the power consumption in the device. This increased power consumption in turn will lead to a temperature rise in the device that can affect its performance and reliability. Additionally, heat dissipation in other electronic devices (except light emitters) follows the following relation:

$$P = VI \tag{1.4}$$

where P is power dissipation, V is voltage of the device, and I is current passing through the device. Thus, for devices that use high voltages or currents, thermal management becomes crucially important. Thus, understanding of nano-scale heat transfer is crucially important for designing these devices for robust operation and reliability.

Nano-scale conductive heat transfer can be classified into two main categories. The first category is composed of nano-scale effects that occur due to size reductions in the materials. This is because for nano-size devices, the mean free path of heat carriers becomes comparable to length scales of the device. Low thermal conductivity of silicon/germanium nanowires is an example where nano-structuring of the material alters the thermal properties [65]. The second category is heat transfer in materials due to their inherent structure. Most amorphous polymers are an example of such materials. They inhibit a low thermal conductivity regardless of their size. Figure 1.1 shows the different nano-scale conductive heat transfer occurrences.

In order to study nano-scale heat transfer in materials, several experimental, analytical, and numerical methods have been developed. Two of the experimental techniques developed to measure nano-scale thermal properties of materials are the three omega (3ω) method [14] and the time domain thermo-reflectance method (TDTR) [19, 15]. Although these experimental methods have very valuable applications, they come with drawbacks such as relatively expensive equipment, a time consuming data collection process, the inability to measure all of nano-scale properties of materials, difficulty in separating the effects of different parameters, and more.

Conversely, numerical and analytical methods not only allow us to separate the effects of different parameters, but also allow us to measure the majority of material thermal properties. In addition, numerical methods allow us to test simple non-physical systems and parameters in order to identify trends and physical insights faster. Numerical models are also very helpful towards explaining experimental obser-

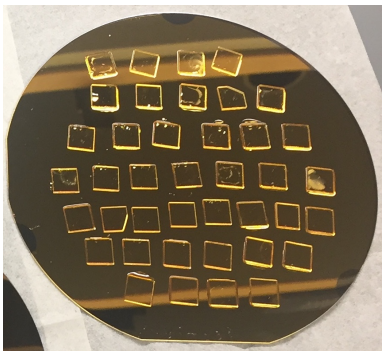

(a) Silicon wafer, k∼150 W/mK

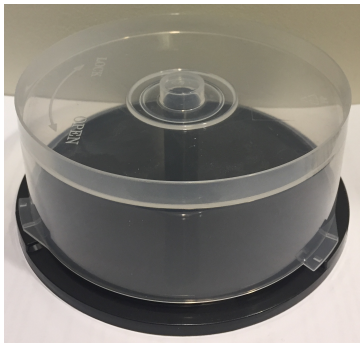

(b) Plastic container, k∼0.2W/mK

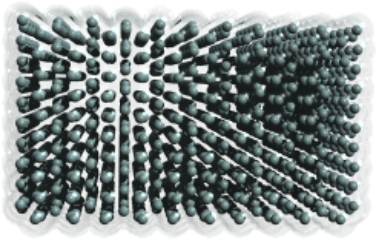

(c) Silicon thin film with thickness of a few micro meters, k∼10s of W/mK

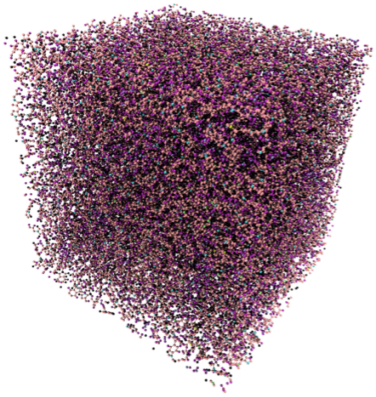

(d) Thin film plastic material (simulated), k∼0.2W/mK

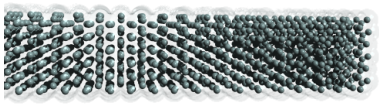

(e) Silicon nanowire, k<10W/mK

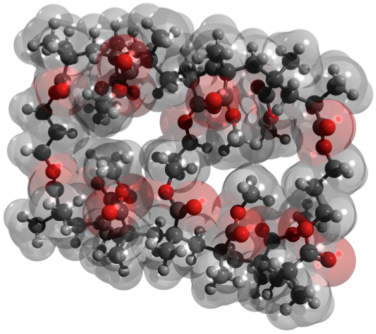

(f) Polymer thin film, k∼0.2W/mK

Figure 1.1: Areas where nano-effects control heat transfer. Figures on the left side, show nano-size effects on heat transfer of crystalline silicon due to miniaturization of the sample. Figures on the right show that thermal conductivity of polymers that are inherently controlled by their nano-size properties. For these materials regardless of their size, heat transfer is controlled primarily by their internal structure.

vations, where access to nano-scale material properties is difficult [132]. For example, because thermal boundary resistance (TBR) is related to the nano-scale structure of the materials at their junction, it is difficult to achieve a rigorous understanding of heat transfer at the junction of materials through fabricated interfaces; this is because such interfaces have numerous parameters that influence their nano-scale structure, which are difficult to reliably control experimentally. Some of these parameters include roughness at the interface, thickness of material slabs, crystalline structure at the interface, defects at the interface or inside the materials, and the strength of bonding at the interface. Therefore, computational techniques such as molecular dynamics, which are suitable for parametric studies, are helpful to distinguish the effects of each pertinent parameter.

Although molecular dynamics is the main tool for studying nano-scale heat transfer in this thesis, it should be noted that several analytical models such as the acoustic mismatch model (AMM) [76] and the diffuse mismatch model (DMM) [163] are also useful tools to study nano-scale heat transfer phenomena. Since AMM and DMM give a relatively simple view of heat transfer at the interface, a short description is provided below followed by a detailed description of the molecular dynamics method.

1.1.1 Acoustic Mismatch Model and Diffuse Mismatch Model

As previously stated, phonons, are the main heat carriers in dielectric materials. When two dielectric materials come in contact, because of the difference between their phonon spectra, heat carriers face a thermal resistance at the junction of materials. Thus, the interface will not fully transmit all of the phonons that are traveling through the materials. AMM [76] and DMM [163] have been developed to model heat transfer at the interface and calculate the amount of thermal boundary conductance. The AMM model assumes that transmission of phonons at the interface follows a specular reflection model. While this assumption is reasonable for low frequency

phonons, it breaks down for high frequency phonons [163]. This divergence from the specular reflection model happens because in the case of high frequency phonons, the wavelength of traveling phonons is close to the atomic spacing in the materials, and thus the assumption of a continuum is no longer valid [163]. DMM was developed to capture this shortcoming of AMM. Instead of a fully specular transmission model, DMM assumes that the probability of transmission for a phonon at the interface is related to the relative density of that phonon in the two materials that constitute the junction [163]. Figure 1.2 shows the difference in how AMM and DMM models treat a phonon that reaches the interface. More detailed description of these models are reported in [163, 76, 135]

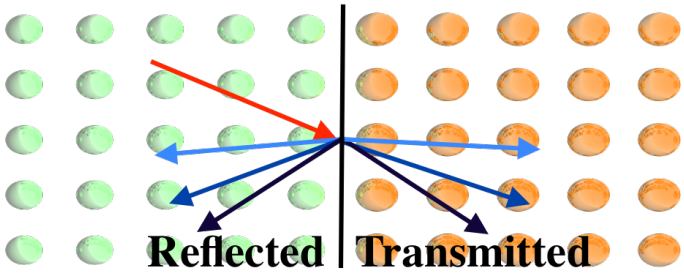

(a)

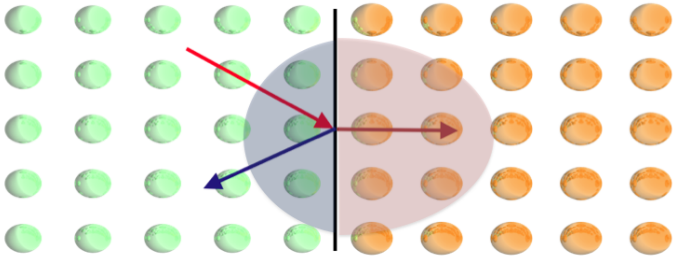

(b)

Figure 1.2: Figure 1.2(a) shows the possible results that the AMM can predict once a phonon reaches the interface. Figure 1.2(b) shows the possible results that the DMM predicts for a phonon that incidents on the interface. The probability of reflection or transmission in DMM depends on the density of that phonon in the two materials.

1.1.2 Molecular Dynamics

The all-atom molecular dynamics method is a simulation technique in which the constituent atoms of a system are explicitly modeled with properties such as mass and Coulombic charge. These atoms are then arranged in a structure that closely represents the physical morphology of the material. Figure 1.3 is an example of atoms arranged in an MD simulation to represent a single polymer chain. Each sphere is an atom and the bonds between the atoms are shown as cylinders.

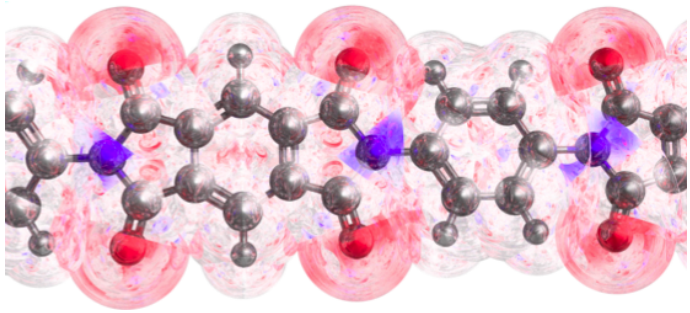

Figure 1.3: A schematic view of a polymer chain modeled using molecular dynamics. Atoms in MD simulations are considered point masses, as shown in the figure with the spheres. Covalent bonds between the atoms are shown as cylinders. The bubbles around the atoms show the radius of effectiveness of their non-bonding interactions.

Molecular dynamics is based on classical physics. This means that the movement of particles in the simulation follows Newton's laws of motion. Equation 1.5) shows the second law of Newton used to model the motion of atoms.

$$\vec{F} = m\vec{a} \tag{1.5}$$

where F is the net force vector acting on a particle, m is the mass of the particle, and a is the acceleration vector of the particle. Additionally, in molecular dynamics, the entire structure of an atom is modeled as a single point mass. Thus, the electronic structure of the atoms is not explicitly modeled in this thesis; the angular momentum of individual atoms is zero. This simplification helps us to simulate systems faster than through density functional theory, where all or part of the elec-

tronic structure is modeled. However, this simplification will limit the applicability of molecular dynamics. For example, molecular dynamics will not be able to calculate the phonon-electron scattering in electrically conductive materials. For such cases, density functional theory methods that model the electronic structure and hence electron transport in the system are suitable. Materials studied in this thesis are mostly dielectrics and pure semiconductors, which do not possess a high electrical conductivity, thus contributions of electrons to heat transfer are negligible [134, 133]. After defining the atoms in the simulation, we need to introduce the interatomic interactions between them. The definition of these interactions is done through a numerical model, commonly known as a force field.

There are many force fields that are developed for different material classes in different conditions. Usually force fields are designed such that they can reproduce certain material properties that are acquired through experiments. In this thesis, the details of force fields and the equations that describe them are detailed in Appendix A. After defining the interatomic interactions, the differential equations that govern the dynamics of the system are solved using numerical methods. In this thesis, velocity verlet, which is a reversible integration method, is used to solve the equations of motion of the atoms. More details about this algorithm and its derivation can be found here [164]. After proper integration of equations of motion, the trajectory of atoms over time is acquired. This trajectory can be analyzed to get useful material properties. For example, the thermal conductivity of materials can be calculated by analyzing these atomic trajectories.

As described above, molecular dynamics has the capability to capture the motion of atoms, and thereby provide valuable insights about heat transfer in the materials. Unlike AMM and DMM, molecular dynamics makes no special assumptions about the phonon transport at the interface and is able to capture anharmonic effects near the interface. Additionally, molecular dynamics is able to calculate the strain field

in the material and the strain relaxation length near the interface. Additionally, for more complicated systems such as polymers, molecular dynamics can distinguish the effects of each pertinent parameter and for that reason it is used in this thesis to study heat transfer in polymers. However, the time consuming process of simulations, lack of available force fields for all of the materials, and the difficult process of gaining insight from large amounts of data that are created during the simulation, are some practical drawbacks of molecular dynamics and other numerical methods such as density functional theory.

In order to address some of these drawbacks, data driven methods such as machine learning have shown promising results [67, 123, 160, 209, 140, 178, 34, 129, 50, 109, 124, 193, 20, 10, 36, 12]. Machine learning based force fields are an example of recent efforts to overcome these challenges [67, 36, 12]. In this thesis, machine learning algorithms have been developed to more rapidly predict the thermal properties of materials. The algorithms are custom designed for predictions of thermal properties with physical rules encoded in them such that function spaces that lead to non-physical results are avoided. A more detailed description of machine learning algorithms is provided in chapter IV.

1.2 Outline of this Thesis

This thesis is ordered in the following manner:

Chapter 2 discusses the effects of strain and interface bonds between silicon and germanium in semiconducting hetero-structures and superlattices. The strain in hetero-structures happens due to the lattice mismatch between the materials. This strain disturbs the atomic order of the materials at the interface and hence affects the phonon transport at the interface of the two materials. First, the strain relaxation length near the interface is calculated using molecular dynamics methods. Then, the effect of this relaxed strain on heat transfer of the structure is compared with

the effects of uniform strain, i.e. non-relaxed strain, throughout the material. In addition, the effects of formation of silicon-germanium bonds at the interface are studied. The results show that for superlattices at very small period lengths, where the density of interface bonds is significantly increased, thermal conductivity of the interface increases. Our phonon density of states analysis confirms formation of strong vibrational peaks in the material that do not belong to either pure silicon or pure germanium. The density of these modes gets stronger as the density of the interface bonds increases. These new vibrational modes provide a new channel for heat transfer in the superlattice and hence they reduce the thermal boundary resistance at the interface of materials at small period lengths. These findings could be used to engineer materials thermal properties through controlling the interface bonds.

Chapter 3 provides the results for the effects of different bondings between the polymer chains on heat transfer in polymers. First, thermal conductance between single polymer chains cross-linked with various cross-linking species is calculated. The contributions of non-bonding interactions, vdW and electrostatic interactions, and cross-linker covalent bonds are calculated and compared. The results show that strong non-bonding interactions have a large impact on heat transfer between the polymer chains. Thus, short cross-linking agents that bring the chains closer to each other result in a higher inter-chain thermal conductance. These results help understand the discrepant results reported in the literature for heat transfer in cross-linked polymers [78, 87, 167, 189, 190, 75, 114, 195, 84]. Furthermore, wave transport simulations show that vibrational modes in the presence of non-bonding interactions travel significantly faster in polymer chains compared to the case where only covalent bonds transfer the wave. This higher propagation velocity in the presence of non-bonding interactions is due to the long-range nature of these interactions compared to covalent bonds. For example, in a coiled polymer chain, the phonon has to travel through all of the covalent bonds in the backbone of the polymer to get transferred

from one end of the chain to the other. However, vdW and electrostatic interactions between atoms at the two ends of the chain can transfer heat both directly and through the backbone atoms. Thus, to design cross-linked polymers with the desired thermal properties, the length of the cross-linker should be considered as one of the most important factors along with other factors that are discussed in chapter 3 such as: the strength of the non-bonding interactions, the number of atoms in the monomer of the polymer, and the side chain size of the polymers.

In addition to the effects of covalent, vdW, and electrostatic interactions, the effects of ionic bonds between the polymer chains and sodium ions are reported in chapter 3. Near double enhancement in thermal conductivity of the polymer is observed upon formation of ionic bonds. The analysis shows that the polymer chains are stretched in the presence of ionic bonds and the density of the polymer is increased. Both of these effects contribute to enhanced thermal conductivity of the polymer system with ionic bonds.

Chapter 4 provides a new numerical method to predict the thermal conductivities of materials using machine learning algorithms. In this method, physical rules are encoded in the machine learning algorithm. The implementation of these physical rules prohibits the algorithm from exploring certain non-physical function spaces that are known a priori would break physical rules. For example, for prediction of phonon lifetimes, a strictly non-negative constraint must be implemented in the algorithm such that the algorithm would not be able to predict a negative value for phonon lifetime.

Chapter 5 provides concluding remarks and future work directions that can be derived from this thesis.

CHAPTER II

Contributions of Interface Bonds and Strain Relaxation Length to Thermal Transport in Hetero-structures

2.1 Introduction

Silicon and germanium are two commonly used materials in electronic devices. As mentioned in the previous section, heat transfer in crystalline silicon and germanium is highly affected when sample size is reduced to micro or nano-meter ranges [134]. Additionally, when two materials come in contact, the very narrow interface region between the two materials, can affect the rate of heat transfer in the structure. The formation of a junction at the interface of the two materials can also introduce strain in the constituent materials of the structure, which may have significant impact on thermal, electrical, and mechanical properties of the structure.

Recently, engineering strain in the lattice structure of materials has been used to enhance the electron mobility in devices (e.g., strained-silicon transistors) [6]. Another example of strain engineering applications is through integrating heterogeneous materials with different lattice constants, such as GaN-based devices on silicon substrates [28]. In addition to the previous devices, thermal management in superlattices, which are made of periodic hetero-structures, becomes important due to the numer-

ous interfaces that these devices have. Superlattices have a wide range of applications in thermoelectric devices [175], semiconductor lasers [18, 169], and transistors [4]. For example, in the previous section, we show that thermal conductivity of thermoelectric devices is a fundamental parameter in controlling their operations.

Generally, thermal conductivity of superlattices made of dissimilar materials reduces as the period length of the superlattice decreases. This is believed to be due to an increase in the number of interfaces for shorter period lengths [69]. However, a few studies have reported an increase in the thermal conductivity for superlattices with very short period lengths. This increase in thermal conductivity for short period lengths has been attributed to phonon coherence in the structure [65, 26]. However, in addition to phonon coherence effects, there may be other factors that contribute to the increased thermal conductivity at the short period lengths. One of these factors is a more uniform lattice structure at small period lengths. Mismatch between the lattice sizes of epitaxial structures creates residual strain in the structure that is at the maximum size at the junction of the two materials, and relaxes away from the junction [11]. The effects of this strain on optical [158, 77, 120] and electrical [181] properties of materials have been previously studied. Due to the changes in spacing between the atoms caused by strain,, the vibrational spectrum of materials is affected, and the thermal properties of hetero-structures may also be affected. Previous studies have examined the impact of strain and stress on heat transfer in bulk materials and interfaces [203, 191, 187]. For example, thermal conductivity of silicon decreased by a factor of $\sim$0.82, when an isotropic tensile strain of $\sim$3% was imposed on the material [90]. On the other hand, both experimental and numerical studies have shown that applying compressive stress on interfaces can increase the thermal conductance of the structure [64, 154]. For superlattices with a period length that is shorter than the strain relaxation length, the strain in the structure does not fully relax. This strain leads to a more uniform lattice structure, which potentially could reduce the

phonon scattering, since phonons experience less variation in acoustic impedance of the two materials. Furthermore, as the number of interfaces increases, the density of interfacial bonds between the two materials in the structure increases. These interfacial bonds introduce new interfacial vibrational modes in the structure (which may have vibrational characteristics intermediate between those of the superlattices two constituent materials). These new vibrational modes are expected to play a role in heat transfer in superlattices by providing additional channels for phonon transport at the interfaces.

In this chapter we assess the effects of variable strain and increased density of interface bonds on heat transfer in hetero-structures and superlattices. First, we use an energy minimization process in order to accurately calculate the strain relaxation in materials. Next, we use molecular dynamics simulations to predict thermal properties of the structures. The strain relaxation lengths calculated here through energy minimization process is in good agreement with previous experimental results. Additionally, we calculate the phonon density of states (PDOS) for the materials in the superlattice. This analysis allows us to compare the differences in the PDOS of superlattices with various period lengths, thereby allowing us to study the contributions of interfacial bonds on heat transfer in the structure. More information is provided in article [134].

2.2 Simulation Technique

In order to calculate the thermal conductivity of materials in MD, there are two main methods. The first method is equilibrium molecular dynamics (EMD), which is based on the Green-Kubo formalism [42]. The Green-Kubo method allows us to calculate thermal conductivity of materials in three directions during only one simulation. The second method is non-equilibrium molecular dynamics (NEMD), which is a direct method to calculate thermal conductivity. The algorithm to calculate

thermal conductivity using NEMD is similar to experimental techniques, where a temperature gradient is measured across the material, while a heat flux is applied to the material. NEMD allows us to calculate thermal conductivity of the material in a single direction during each simulation. The governing equation of Green-Kubo method [42] is shown in Equation 2.1.

$$k = \frac{1}{3Vk_bT^2}\int_0^t < J(0).J(t) > dt \tag{2.1}$$

where k is thermal conductivity of material, V is volume, k_b is the Boltzmann constant, T is the temperature of the system, J is the heat flux, and $< . >$ denotes the autocorrelation function. The amount of heat flux in the system is related to the movement and position of atoms in the system. Non-equilibrium molecular dynamics is commonly used for thermal transport calculations in one to three dimensional systems [134, 143, 100, 197, 96, 200, 174, 9, 25, 173, 136, 154, 205]. As previously mentioned, in this method, a temperature gradient is created across the material. Subsequently, thermal conductance (TC) in the material is calculated using Fourier's law of conduction as described in Equation 2.2 [96, 134, 143, 188, 192].

In this chapter, we use a non-equilibrium molecular dynamics (NEMD) technique [105]. The Stillinger-Weber (SW) force field [162] is used to introduce the interatomic interactions between the atoms. The initial location of atoms is set such that a piecewise constant strain field is created in both materials, similar to previous studies [87, 22]. We use non-periodic boundary conditions in all directions to model thermal transport in nanorod structures. Additionally, this boundary condition allows the strain to relax in the system. In order to relax the strain, a steepest descent (SD) energy minimization technique is used before the dynamic simulations. The criteria used to stop energy minimization is when either the normalized change of the potential energy of the entire system is less than 10^{-12} or the change in the total force vector is

less than 10^{-12} (Kcal/molÅ). We fix the four most-outward layers of atoms in place to prevent the atoms sublimating into a vacuum during dynamic simulation. We use a time step of one femtosecond [65] to capture the fastest atomic motions in the system. In order to thermalize the system, we first use a Langevin thermostat [145]. We start the thermal relaxation process by first setting the temperature to 5 K for 0.1 ns. Next, we increase the temperature to 50 K for 0.2 ns. Then, we set the temperature to 500 K for 0.7 ns. Next, in order to create a temperature gradient, we use an NVE ensemble (constant number of particles, volume, and energy), while we pump heat in one end of the system and remove the same amount of heat from the other end. We let the system evolve for 6.5 ns. After this time, the temperature in the system has stabilized. Next, we let the system evolve for one more nanosecond, in order to derive the thermal conductivity and/or thermal boundary resistance (TBR). Figure 2.1 shows a schematic of the single junction simulation cell used in this study. The temperature profile of the system is averaged over the final one nanosecond, which achieves a good statistical average. We use Fourier's law to calculate the thermal boundary resistance, according to the following equation [105]:

$$TBR = \frac{Q}{\Delta T} \tag{2.2}$$

where Q is the heat flux passing through the interface, and ΔT is the difference between the temperature of materials at the interface.

Previous studies on heat transfer in multilayer or two layer hetero-junctions with considerable lattice mismatch have not fully considered the strain relaxation length effects on thermal transport [87, 22, 208]. Since strain changes the lattice structure of the material, considering the lattice variation could be crucial for calculating optical, thermal, or electrical properties. Usually, for molecular dynamics (MD) simulations, a piece-wise constant strain is considered for both materials in contact. The downside of using a piece-wise strain across the two materials is that the effects of varying

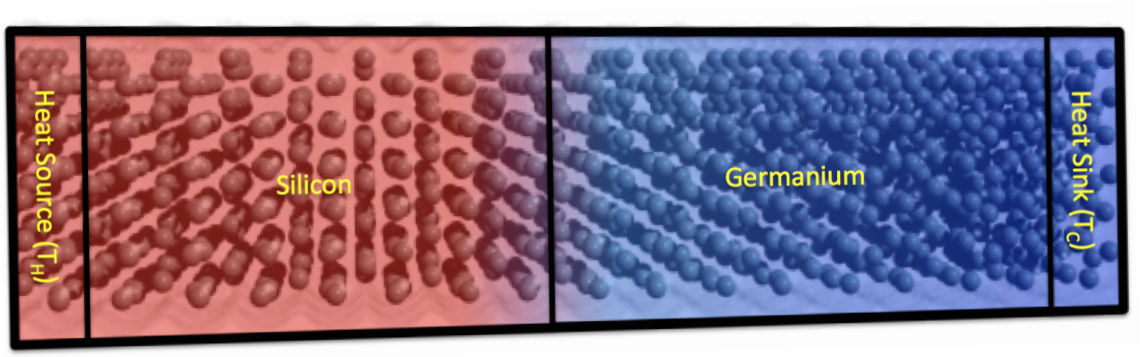

Figure 2.1: A schematic view of a single junction hetero-structure simulation cell used in this study

material properties such as phonons, which may significantly impact heat transfer, are ignored.

In order to calculate the strain in our simulations, at each time step, we calculate the position of the center of mass of each atomic layer. Next, we calculate the change in distance between the center of mass of the two adjacent layers. In order to calculate the strain, we compare this change in distance with respect to the interlayer distance of the pure materials at room temperature. The following equation is used to calculate the strain (Eq. 2.3).

$$\varepsilon_{x,mn} = \frac{\left(\frac{\sum(x_{m,i}) - \sum(x_{n,j})}{(y*z*2)}\right)}{SL} \tag{2.3}$$

where $\varepsilon_{x,mn}$ is the strain in the x direction between adjacent layers m and n , y and z are the number of cross sectional atomic unit cells, i and j are the atom numbers in the m and n layers respectively. SL represents the distance between the two layers in the pure material at room temperature.

So as to verify the accuracy of our simulations and the force field used, we calculate the lattice constants and thermal conductivities of pure silicon and germanium. For these simulations, we use periodic boundary conditions, and the Green-Kubo method [42, 105] to calculate the thermal conductivities. We average 21 calculations. The results are shown in Tables 2.1 and 2.2. Our results are in good agreement with

literature values [5, 90, 150]. All MD simulations have been done using the LAMMPS (http://lammps.sandia.gov) package [125].

Table 2.1: Calculation of silicon and germanium lattice constants in order to verify the validity of the force field and simulation method.

Material	Lattice Constant (Å)
Silicon	5.433
Germanium	5.655

Table 2.2: Calculation of silicon and germanium thermal conductivities in order to verify the validity of the force field and simulation method.

Material	Thermal Conductivity (W/mK)
Silicon	107±32
Germanium	59±12

2.3 Results and Discussions

We calculate the strain relaxation in a single Si/Ge hetero-junction. Next, we study the effects of this strain relaxation on interfacial heat transfer. Finally, we examine the effects of interface bonds on heat transfer in superlattices. Our simulation cell for this study consists of 10×10×288 unit cells. The atoms are arranged in the diamond cubic lattice structure.

2.3.1 Calculation of Relaxed Strain Profile in Si/Ge Bi-layer Structure

We first create hetero-structures with piece-wise constant strain in the materials. Next, we use an energy minimization step to relax the strain in the material prior to dynamical simulation. The initial piece-wise constant strain profile used here is similar to previous studies [87, 22], and is in the direction parallel to the interface. After minimizing the potential energy of the system, we observe that most of the strain relaxes in a few nano-meters away from the interface (∼2 nm). Figure 2.2 shows the

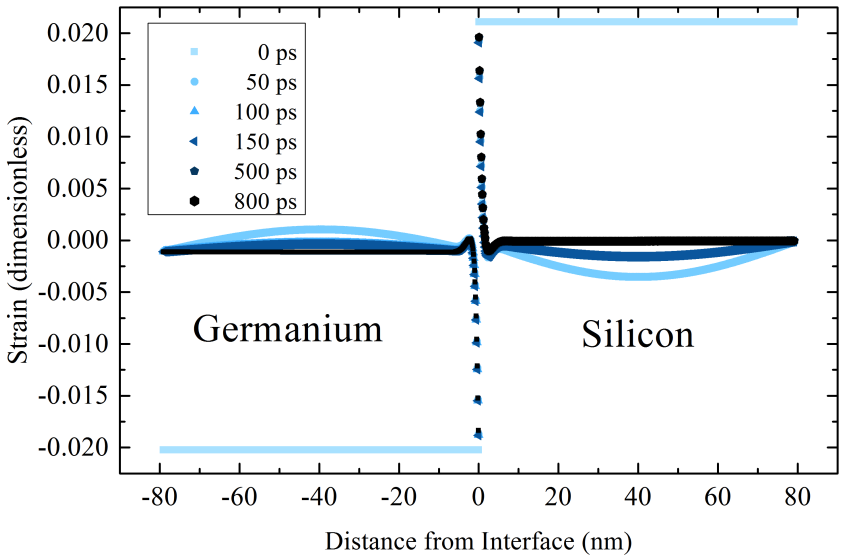

Figure 2.2: Strain profile in the direction parallel to the interface during strain relaxation process as a function of time during the process.

the strain profile in the material as a function of time as the algorithm approaches the minimum in potential energy. Our strain relaxation length at the junction is in good agreement with previous experimental results [11, 182]. This relaxed strain profile could be used to study mechanical, optical, electrical, and thermal properties of Si/Ge hetero-junctions.

2.3.2 Effects of Strain Relaxation on TBR

Due to the change in the material and strain at the interface of the two materials, we anticipate a high rate of phonon scattering near the interface of the two materials. This high rate of scattering leads to a thermal boundary resistance at the interface of the two materials. In order to study this effect, after the systems described in the previous section reach equilibrium, we use NEMD to study TBR at the interface of materials. TBR is calculated using Equation 2.2. We simulate TBR in systems with constant piece-wise strain profile and relaxed strain profile. The results for TBR for these two different strain conditions are shown in Table 2.3. We observed that the

TBR values calculated for both strain conditions do not have a significant difference. This observation suggests that TBR values are mostly affected by the lattice properties near the interface and not the lattice strain relaxation length. We believe that the slightly higher TBR values for the systems with relaxed strain conditions are due to higher rates of phonon scattering near the interface of the two materials. This is because of the sharp transition of the lattice structure at the interface.

Table 2.3: Calculations of TBR at different temperatures for different strain conditions

Strain and Temperature Conditions	TBR (W/m^2K)
Piecewise constant strain (600K)	(2.85±0.02)e-9
Relaxed strain (600K)	(2.96±0.13)e-9
Piecewise constant strain (500K)	(2.91±0.09)e-9
Relaxed strain (500K)	(3.07±0.17)e-9
Piecewise constant strain (300K)	(3.62±0.05)e-9
Relaxed strain (300K)	(3.77±0.09)e-9

Since literature values for TBR at the interface of hetero-junction nanowires are not available, we compare the magnitude and the trend of our results with literature values for TBR between hetero-junction sheets of silicon and germanium [87].

2.3.3 Effects of Strain and Interface Bonds on Thermal Conductivity of Si/Ge Nano-wire Superlattices

In the previous part, we found that the strain relaxation length in a Si/Ge heterostructure is a few nanometers away from the interface. We also showed that TBR at the interface of the two materials is not significantly affected by the strain far from the interface. It is interesting to consider the effects of strain relaxation on heat transfer in superlattices that have a period length on the order of strain relaxation length. These type of superlattices have potential application in thermoelectric materials [175]. To study this effect, we model Si/Ge nanorod superlattices of various period lengths with a total length of ∼160nm. The cross-sectional area of the superlattices is 4.43 nm ×

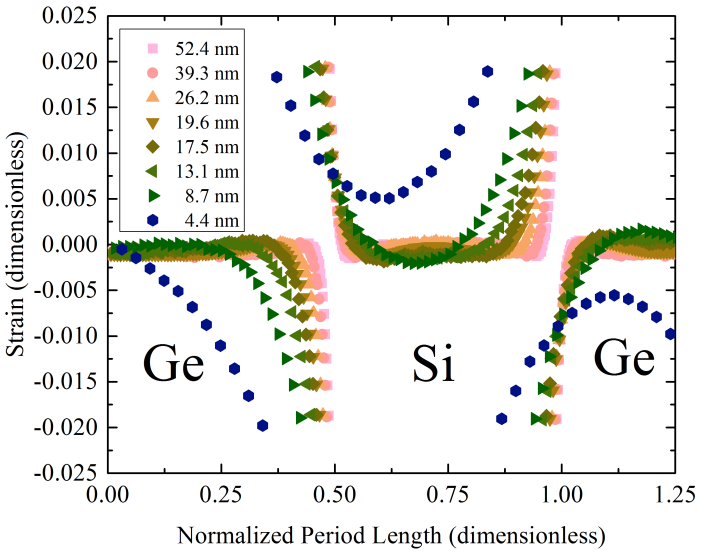

Figure 2.3: Calculation of strain profiles in superlattices with different period lengths. In order to better illustrate the strain profile, we have normalized the period lengths of all superlattices.

4.43 nm. We relax the strain in the structure using the energy minimization technique that was previously described. The relaxed strain profiles are shown in Figure 2.3. Figure 2.4 illustrates strain profiles in a superlattice with a period length of 20 nm. In Figure 2.5 we have shown the average lateral lattice constant in superlattices with very short period lengths. This figure shows that lattice constant does not vary significantly for short period lengths. This indicates that for short period lengths, there is less phonon scattering at the interface of the two materials.

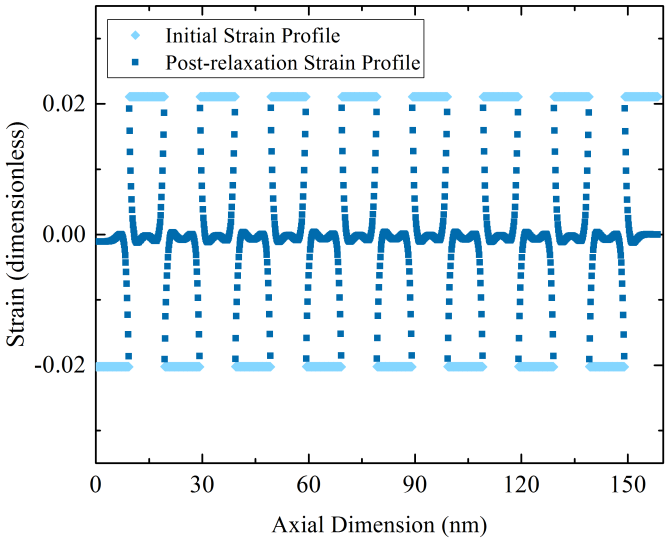

Figure 2.4: Calculation of strain relaxation profiles before and after relaxation in eight periods of a superlattice with a period length of 20nm.

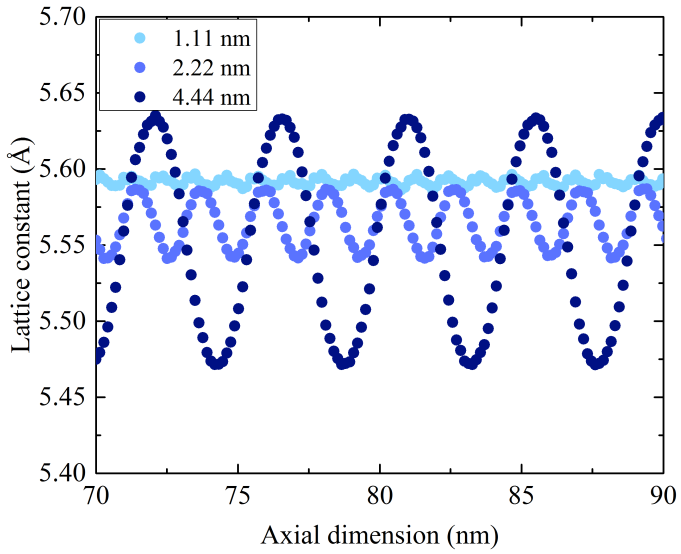

Figure 2.5: Calculation of relaxed lattice constant profiles for superlattices with very small period lengths.

We study heat transfer in superlattices with either relaxed strain profiles or piecewise constant strain profiles. We expect the thermal conductivities of Si/Ge super-

lattices with short period lengths to be similar, regardless of the strain relaxation condition in the structure. We also anticipate the thermal conductivities of short period lengths to be similar, regardless of strain relaxation condition used. This is because the strain does not fully relax in short period lengths for either type of strain conditions used. Figure 2.6 shows the thermal conductivity values for superlattices with various period lengths and strain conditions. We observe a minimum in thermal conductivity of superlattices with respect to the period length. Previous studies have also reported a similar minimum in thermal conductivity of superlattices at short period lengths [65, 26]. This minimum thermal conductivity have been attributed to phonon coherence effects in the materials[65]. Interestingly, period lengths of superlattices for which the thermal conductivity starts to increase as the period length decreases, is very similar to the strain relaxation length of the two materials. This short period length leads to a lattice structure that is more uniform across the structure. This uniform lattice structure scatters phonons less, and thus will attribute to enhanced thermal conductivity of the structure.

To calculate the thermal boundary resistance per interface for different superlattices, we first model silicon and germanium nanowires with a length of 159.7 nanometers. We calculate the thermal conductivities of these nanowires to be 24.75 W/mK and 16.49 W/mK, respectively. Previous studies also show that the thermal conductivities of silicon nanowires are length dependent [185]. Using these values, we back-calculate the TBR values for each interface in various superlattices. The results are reported in Figure 2.7. We observe that decreasing the period length results in a reduction in the TBR values.

Additionally, we calculated the number of bonds between silicon and germanium atoms (which happen at the interface) in different superlattices. We report the density of these interface bonds compared to the total number of bonds in the structure in Figure 2.8. We observe that for superlattices with short period lengths the density

of interface bonds significantly increases. Thus, these bonds have an important effect on thermal conductivities of superlattices with short period lengths.

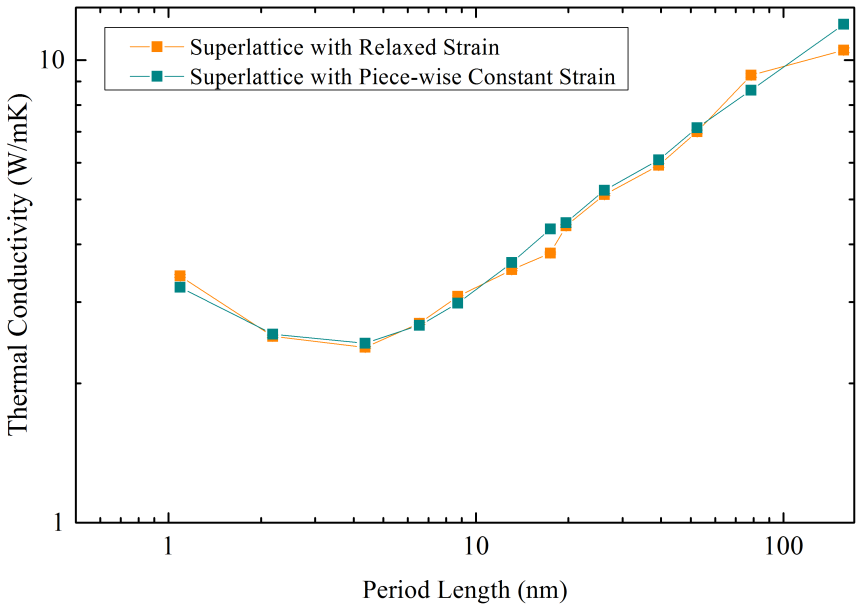

Figure 2.6: Calculation of thermal conductivity of superlattices as a function of period length.

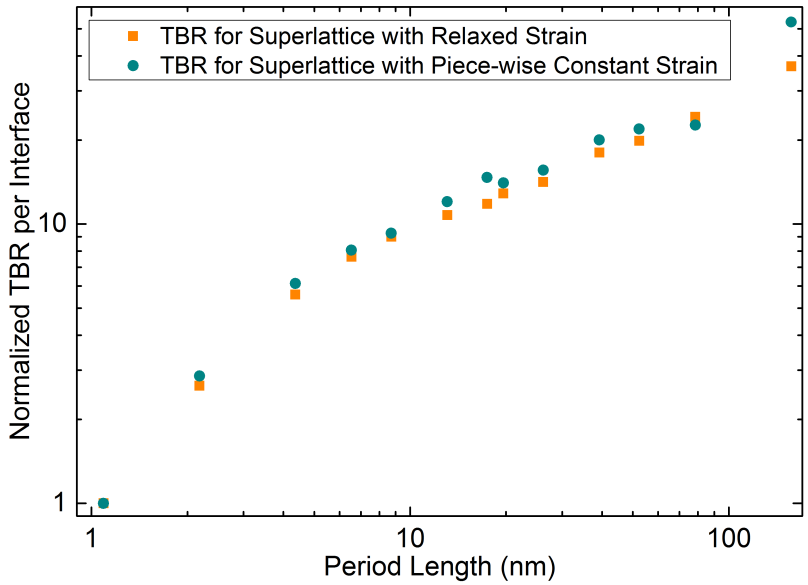

Figure 2.7: Calculation of average TBR per interface for superlattices as a function of period lengths.

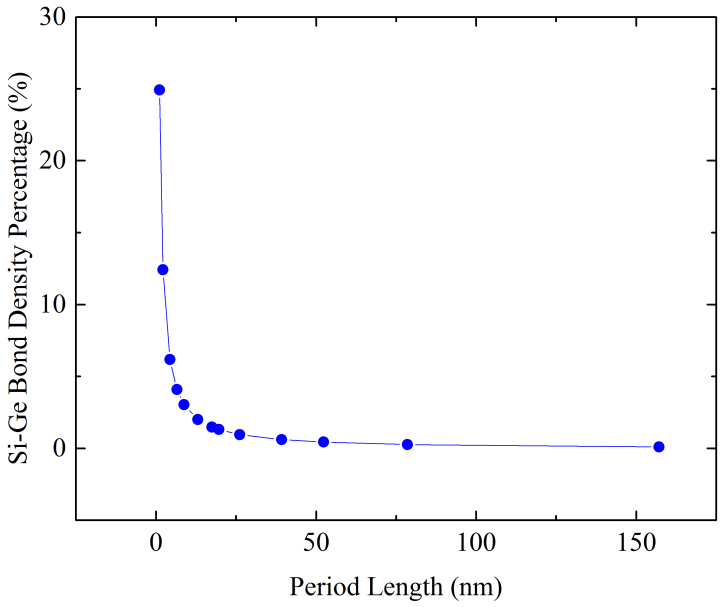

Figure 2.8: Density of silicon-germanium bonds at the interfaces vs. period length of the superlattice for superlattice structures studied.

We use the Fourier transform of the velocity autocorrelation function in order to calculate the phonon density of states (PDOS), for superlattices with various period lengths. These PDOS values allow us to understand the mechanisms of heat transfer in superlattices with short period lengths. Previous studies have used the Fourier transform of velocity autocorrelation function to calculate the PDOS of nanowires [73, 148]. These results are shown in Figure 2.9.

Our calculations show that the PDOS of both materials shows a new vibrational peak between 12 THz and 15THz for period lengths smaller than the strain relaxation length. These vibrational peaks appear because of an increase in the density of interface bonds for small period lengths. These new vibrational modes introduce new pathways for heat transfer in the superlattice structure, since these new vibrational modes exist in both silicon and germanium. Thus, the interface is transparent to these modes and these modes can support the propagation of vibrational modes in the system.

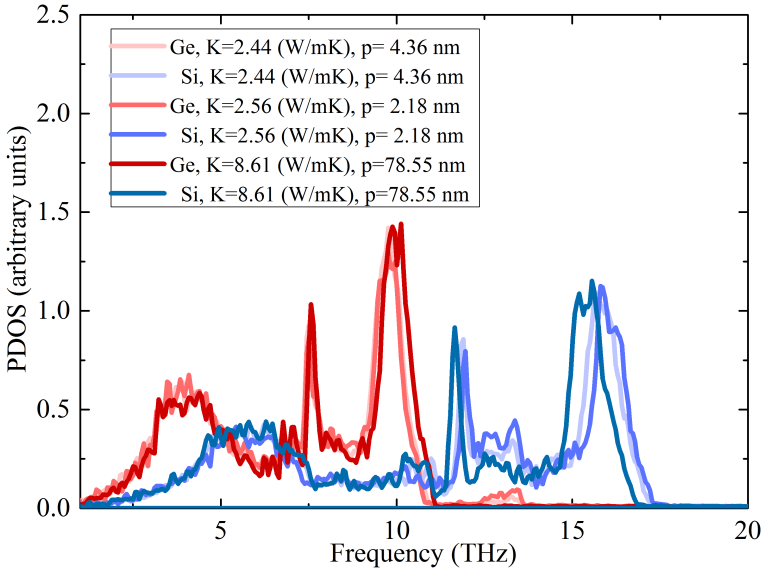

Figure 2.9: Calculation of phonon density of states (PDOS) of silicon and germanium in superlattices with different period lengths. Since the vibrational properties of a lattice depend on the characteristics of the bonds between the atoms, thermal conductivity of superlattices with different densities of interfacial bonds can differ.

CHAPTER III

Nano-scale Heat Transfer in Cross-linked and Ionic Bonded Organic Polymers

3.1 Introduction and Motivation

The unique properties of polymers have caused these materials to gain considerable interest for applications in devices such as organic field effect transistors and other electronic devices [83, 66], thermoelectric devices [33, 156, 80, 147, 13], photovoltaic devices [35], photonic devices [59], and thermal devices [118]. Moreover, polymers have applications in lithography and patterning [165], drug delivery[142], and plastics products [151, 58]. Some notable properties of polymers that contribute to their unique and broad usability are as follows: reduced cost, low melting temperature, mechanical flexibility, abundance of material available, wide variety of polymeric material options, and greater ease in fabrication. As stated in Chapter I, the rate of heat transfer in materials affects their application in many devices. This impact of heat transfer on device reliability is also true for devices made of polymers [180, 55]. For example, solar cells [55] and the plastics industry [202] could benefit from enhancement in thermal conductivity of polymers (the thermal conductivity of most amorphous polymers is on the order of 0.1 W/mK [60, 78]). In contrast, for some applications, lower thermal conductivity is desired, such as for a thermoelectric device intended for achieving

a better figure of merit[194]. Previous computational studies [40, 29, 60, 202, 199, 200] and experimental studies [139, 159, 30, 177, 155, 17, 41, 176, 16, 207] have repeatedly shown and supported that, in the direction of chain alignment, the thermal conductivity of aligned linear polymer chains is significantly higher than that of bulk amorphous polymers. This high thermal conductivity in the direction of chains has been attributed to a relatively large thermal transport by covalent bonds [7, 60, 155]. Concurrently, it is predominantly believed that the low thermal conductivities of amorphous bulk polymers are because of weak inter-chain forces such as van der Waals (vdW) interactions [78] creating a bottleneck for flow of heat in polymers. A previous study showed that vdW interactions are an order of magnitude less efficient at transferring heat than covalent bonds [38].

Traditionally, mechanisms to enhance thermal transport in polymers have been based on the inclusion of thermally conductive fillers[92, 102, 184]. However, enhancing inter-chain interactions [81, 78, 87, 198, 186] has emerged more recently as a method to control the thermal conductivity of polymers without needing conductive fillers. The enhancement in inter-chain interactions can take different forms, such as through the formation of hydrogen bonds between polymer chains [198, 81], the formation of ionic bonds between chains [152], or the formation of covalent bonds between polymer chains [78]. A common synthesis approach for polymers is through crosslinking of polymer chains through covalent bonds, a method that would seem to be a compelling way to enhance their thermal conductivity[78, 87, 167, 189, 190, 75]. However, significant discrepancies have been found within computational and experimental studies of thermal conductivity in crosslinked polymers. For instance, experimental studies demonstrated 50% enhancement of thermal conductivity for polyethylene samples[87] at high crosslinking densities and approximately 30% enhancement for polystyrene at 20% crosslinking density[190], while computational studies predicted a threefold enhancement in the bulk thermal conductivity of polyethylene upon

crosslinking[78] and almost no change in the thermal conductivity of polystyrene at 20% crosslinking density. Furthermore, other studies measured or predicted only a very small enhancement[78] in thermal conductivity upon crosslinking, or even a reduction in thermal conductivity[114, 195, 84]. In a study conducted by Yu et al.[195], experimental results showed a nearly 30% reduction in the thermal conductivity of polyethylene upon crosslinking. Numerical simulations by Ni et al.[114] also suggested that crosslinking 10% of the carbon atoms in polyethylene chains results in a 44.2% reduction in bulk thermal conductivity. Given the many applications of crosslinked polymers[121, 161, 142, 59, 116, 53, 122, 146, 170, 54, 138, 46] and the importance of thermal conductivity to many of these applications, it is critically important to build a comprehensive understanding of the effects of crosslinking on thermal transport.

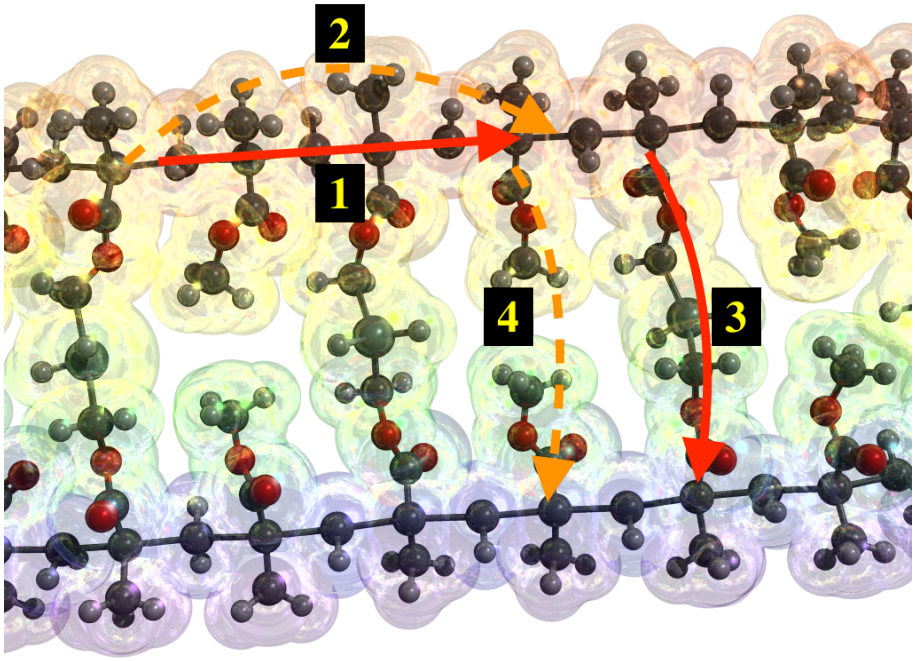

Figure 3.1: Shown are four possible thermal transport mechanisms in polymers: 1) Thermal transport along polymer chains through covalent bonds, 2) Thermal transport along chains through non-bonding interactions (the bubbles around the atoms illustrate the radius of effectiveness[168] of vdW interactions), 3) Thermal transport between polymer chains through covalent bonds, and 4) Thermal transport between polymer chains through non-bonding interactions. Electron drift is not considered, since it is negligible in electrically insulating polymers[95].

Thermal conduction occurs through four mechanisms in electrically insulating crosslinked polymers, as shown in Figure 3.1. These mechanisms are often closely coupled and can affect each other. For example, the spacing between linked polymer chains is strongly influenced by the length of the crosslinking agent that connect the chains. In turn, this spacing has great influence on the heat flow between the chains via non-bonding interactions. Therefore, when designing polymers with desired thermal characteristics, it is crucial to distinguish the contributions of bonding and non-bonding interactions. In addition to length, the vibrational properties of a crosslinker (as directed by chemical structure, mass, and geometry) are anticipated to have an important effect on thermal transport. For example, the crosslinked polyethylene polymer studied by Ni et al.[114], Yu et al.[195], and Kikugawa et al.[78] each used a different crosslinking agent to connect the polymer chains and they all reported different thermal conductivity values.

In this chapter, heat transfer in crosslinked and ionically bonded polymers are studied. The results in this chapter show that thermal conductance between polymer chains is strongly influenced by length of the crosslinker. While it has been traditionally presumed that crosslinkers increase heat transfer by providing thermal shunts between chains, we demonstrate that crosslinkers increase heat transfer predominantly by increasing non-bonding interactions between the chains, and not through the creation of thermal shunts. Shorter crosslinkers reduce inter-chain distances between polymers more productively than longer ones. For this reason, enhancement of thermal transport between the polymer chains could be most effective via short crosslinkers. Additionally, the results in this chapter show that heat transfer in polymers increases upon introduction of ionic bonds between the chains. This increase in thermal conductivity is accompanied by an increase in the radius of gyration of polymers in the system, as well as an increase in the density of the system. More information is provided in article [133] (Part of material in this chapter were reproduced

in part with modification from [133]).

3.2 System Preparation and Simulation Procedure

The molecular dynamics method was described in Chapter I as a tool to study heat transfer in nano-size systems. It should also be noted that although molecular dynamics simulations do not consider electron flow through the material, because polymers studied in this thesis are not electrically conductive, the thermal transport due to electron drift is negligible [95]. Thus, given the small size of polymer chains and the ability of molecular dynamics to capture the main heat transfer mechanisms in polymers, molecular dynamics is used in this study.

In order to investigate heat transfer in polymers, we used the non-equilibrium molecular dynamics (NEMD) technique described in previous chapter in section 2.2. NEMD was chosen because of the difficulty in defining the direction of polymer chains during simulations, and because we are interested in overall thermal boundary conductance at the interface, rather than a directional thermal conductance. In this work, thermal transport in PMMA (polymethyl methacrylate) polymer chains was studied. Two PMMA polymer chains were crosslinked with different crosslinking agents and with varying degrees of crosslinking (0%, 35%, 50%, 65%, and 100%). Each PMMA chain consisted of 20 monomers (an icosamer) (similar to Figure 3.2), and two ends of each polymer chain were terminated with a single hydrogen atom. The varying degree of crosslinking allows us to gain insights about the impact of highest possible crosslinking density while we are able to draw broader conclusions for all degrees of crosslinking. PMMA was chosen due to the high number of atoms in its monomer (15 atoms per monomer); this allows us to investigate the impact of non-bonding interactions. In section 3.3.4, heat transfer in polyethylene (PE) chains and polyvinyl alcohol (PVA) chains are also studied to generalize the results to other polymers. Figure 3.2 represents the structure of two crosslinked PMMA polymer chains used in

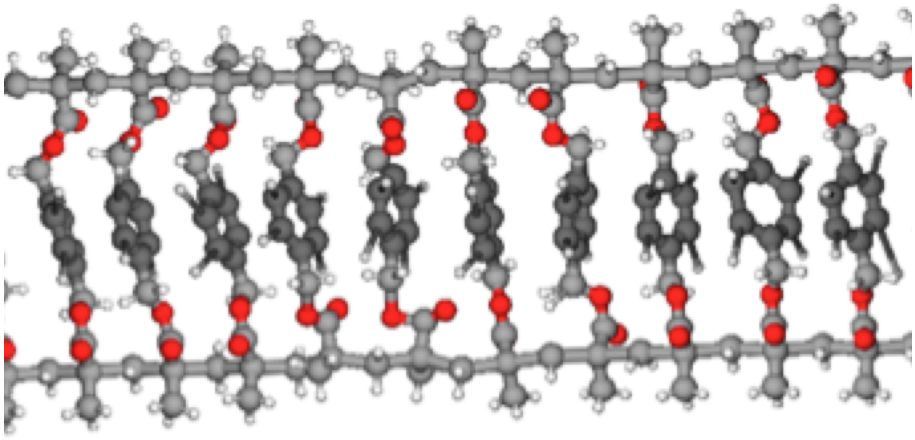

Figure 3.2: Schematic view of two PMMA chains 100% crosslinked by benzene-1,4-diyl crosslinkers.

this study. In this figure the polymer chains are 100% crosslinked by benzene-1,4-diyl crosslinkers.

After creating the simulation box and organizing the atoms inside it, the steepest descent minimization technique was used to minimize the initial energy in the system. The minimization step was followed by a 0.5 ps relaxation step under NVE conditions (constant number of atoms, volume and energy) to release all of thermal stress in the system. For all simulations, a 1 fs time step was used in order to capture the fastest molecular motions in the system, unless indicated differently. Next, four terminal hydrogen atoms at the end of the chains were fixed in order to control the chain endpoints and avoid rotational movement and coiling in the polymer chains. Next, the system was evolved as an NVT ensemble (constant number of atoms, constant volume and constant temperature) for 1.5 ns at 300 K using the Langevin[144] thermostat. This step was followed by another 1.5 ns relaxation step at 300K using the Nose-Hoover [115, 62] thermostat. Using these several steps relaxation scheme, the system reaches thermal equilibrium at 300K. In order to show thermal relaxation, temperature and potential energy profiles of some of the systems during simulations are reported in Figure 3.3.

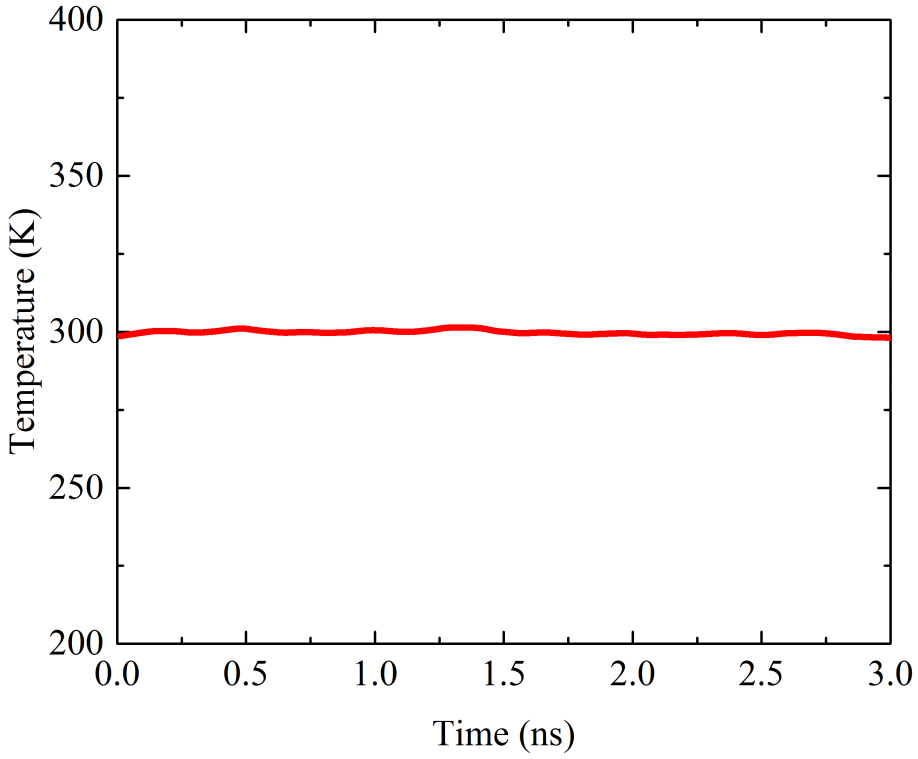

Figure 3.3: Average temperature during relaxation for a system 75% cross-linked with CH_2

After relaxation, in order to use the NEMD method to calculate the thermal conductance at the interface of the two polymer chains, we need to create a temperature gradient between the chains. In order to establish a temperature difference between the chains, "heat" was pumped into one chain, while the same amount of "heat" was extracted from the other chain. This addition and removal of "heat" at the heat source and heat sink happens at the same rate in order to keep the total energy of the system constant, as well as allow the system to reach a steady state situation. In order for this newly imposed temperature gradient in the system to reach steady state situation, the system was evolved for 3 ns to reach equilibrium. System temperature profiles during relaxation step are reported in Figure 3.4. For all relaxation steps, free non-periodic boundary conditions were used. Boundaries were fixed after

the relaxation step in order to collect the trajectory data of atoms for inter-chain distance analysis. Fixing boundaries eliminated the need to calculate and account for box size during each time step during the simulation. For simulation of PMMA polymer chains, the OPLS force field was used to introduce the inter-atomic interactions [72, 74, 23]. The OPLS force field was used since it has been successfully used for thermal property predictions in the past [201, 79, 27, 85, 2, 43]. The parameters for this force field are reported in Appendix A. Equations 3.1, 3.2, 3.3, and 3.4 show the mathematical representations of this force field [72]. Additionally, in order to ensure that our results are independent of the choice of force field, different force fields were used for PVA and PE simulations. The details of these force fields and their parameters are reported in the Appendix A. Regardless of the force field used for polymers, the conclusions are consistent as reported in the following sections of this chapter.

$$E_{tot} = E_{non-bonding} + E_{bonding} + E_{bending} + E_{torsions} \tag{3.1}$$

$$E_{non-bonding} = 4\epsilon((\frac{\sigma}{r_{ij}})^{12} - (\frac{\sigma}{r_{ij}})^{6}) + \frac{1}{4\pi\epsilon_0}\frac{q_i q_j}{r_{ij}} \tag{3.2}$$

$$E_{bonding} = \frac{1}{2}k_{bond}(r_{ij} - r_{ij}^0)^2 \tag{3.3}$$

$$E_{bending} = \frac{1}{2}k_{bend}(\theta_{ijk} - \theta_{ijk}^0)^2 \tag{3.4}$$

$$E_{torsion} = \Sigma^4{}_{i=1} K_n(1 - (-1)^i cos(n\phi)) \tag{3.5}$$

where ϵ and σ are the Lennard Jones potential parameters, r_{ij} is the vector between atoms i and j, q_i and q_j are charges of atoms i and j, respectively, ϵ_0 is the dielectric constant of vacuum, $k_{bonding}$ is the bond stiffness, $k_{bending}$ is the angle stiffness, θ_{ijk} is

the angle between atoms i, j, and k, K_n is the OPLS dihedral parameter, and ϕ is the dihedral angle.

Since non-periodic boundary conditions were used in the simulations, and the size of the system was relatively small, special care was required so that energy drift in the system could be avoided. One of the measures taken here to avoid energy drift in the system, is to set a cut-off value for the non-bonding interactions that is longer than the length of the simulation box. This large cut-off distance will ensure that all non-bonding interactions between the atoms in the system are accounted for. For inter-chain distance calculations, the difference in positions of centers of mass of chains are compared and averaged over a period of time. Similar to Chapter II, LAMMPS package was used to carry out all of the simulations [126]. Polymer structures and simulation files were prepared using Avogadro[57], VMD[68], and Polymer Modeler (available at nanoHUB[56]). Figures of polymer systems were created with POVray [1] using Kirke [179]. Kirke package was also used for polymer topology analysis.

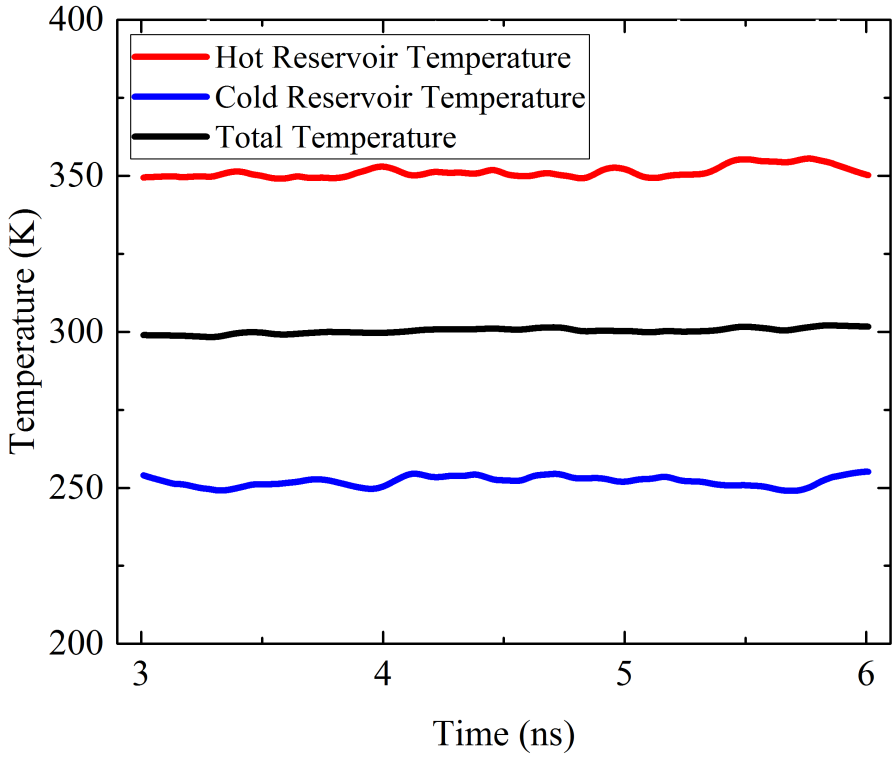

Figure 3.4: System temperature profile during creation of temperature gradient in the system.

Equilibrium values for bulk density and thermal conductivity of three polymers studied in this chapter are calculated using their perspective force fields, in order to ensure that the force fields are suitable for the prediction of thermal properties of these polymers. Thermal conductivity of PAA is calculated and confirmed in the respective section. The results for these validations are shown in Table 3.1. Our results are in good agreement with experimental values for these parameters.

Table 3.1: Calculation of density and thermal conductivity of bulk polymers for validation of force fields. k is thermal conductivity

Material	Calculated k (W/mK)	Expected k (W/mK)	Density (g/cm^3)	Expected Density (g/cm^3)
PMMA	0.22+/-0.02	0.20+/-0.01 [186]	1.12	1.17-1.20 [103]
PVA	0.35+/-0.05	0.31+/-0.02 [186]	1.14	1.21-1.31 [103]
PE	0.37+/-0.06	0.35+/-0.00 [204]	0.85	0.91-0.93 [103]

3.3 Analysis of Simulation Results and Discussion

In this section, results are broken down in various sub-sections to illustrate the effects of each parameter on heat transfer in polymers. First, the effect of crosslinking on heat transfer and acoustic wave propagation between two polymer chains is discussed. Second, the effects of crosslinking density on heat transfer between the chains are illustrated. Third, the effects of vibrational density of states of crosslinkers on heat transfer between polymer chains are studied. Forth, the effects of enhanced non-bonding interactions and chain entanglement on heat transfer in polymer chains are discussed. Finally, the effect of ionic bonding on heat transfer in bulk polymers is studied.

3.3.1 Heat Transfer and Wave propagation in Crosslinked Polymers

In order to elucidate the contributions of covalent bonds between crosslinking agents to heat transfer in polymers, a system of crosslinked PMMA polymer chains were simulated here. The specifications of the systems and simulation methods are reported in the previous section. The simulation results in this section help us to understand the discrepancies in the thermal conductivity values reported for crosslinked polymers in the literature [78, 87, 167, 189, 190, 114, 195, 84]. First, a system with 100% crosslinking density is studied in order to illustrate the highest impact of crosslinking on heat transfer between polymer chains. It is worth noting that such high crosslinking densities can frequently be found in epoxies and resins[24], while a PMMA polymer system with 100% crosslinking density may not be realistically feasible. However, this high crosslinking density is chosen for the purpose of understanding the theoretical maximum impact that crosslinkers could have on heat transfer in polymers. In addition to 100% crosslinked PMMA systems, thermal conductance between polymer chains with a lower density of crosslinking is studied in the following sections in order to show that the main results are not dependent on the polymer crosslink-

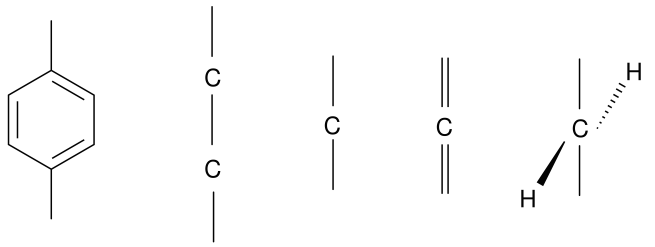

Figure 3.5: Chemical structure representation of crosslinker agents used in this study. From left to right: benzene-1,4-diyl crosslinker, double carbon chain, single carbon with single bonds, single carbon with double bonds (allene), and CH_2 crosslinker (carbene). Mass of carbon atoms in benzene-1,4-diyl crosslinkers are chained to create new crosslinkers with lower total mass in order to study the effect of mass on thermal transport. Carbon atoms in the benzene ring each had either the same mass as a regular carbon atom, half of the mass of carbon atom for "light benzene-1,4-diyl", or twice the mass of carbon atom for "heavy benzene-1,4-diyl". A similar approach was taken to study the effect of bond stiffness on heat transfer between polymer chains by using singly or doubly bonded carbon atoms as crosslinkers.

ing density. Another pertinent parameter on heat transfer between polymer chains that has been considered is the type of crosslinkers used. Crosslinkers with a range of different shapes, masses, bond strengths, lengths, and vibrational characteristics are accounted for in this study (shown in Figure 3.5). Figure 3.5 was created using [8]. Although most of the crosslinking agents studied here are real physical structures, some unphysical crosslinking structures are also studied. These non-physical crosslinkers are studied in order to enable us to isolate the effects of different parameters on heat transfer between polymers. For example, "light benzene-1,4-diyl" (which is a benzene-1,4-diyl crosslinker in which the mass of carbon atoms are halved) is studied in order to show the impact of the mass of the crosslinker on heat transfer between the chains in comparison to the case where regular benzene-1,4-diyl is used to connect the chains.

In addition to varying the structure of the crosslinking agent, the effects of each bonding type are isolated in the simulations by selectively turning them on or off. This selective inclusion of atomic interactions is done by either including or excluding them in the force field calculations. Selectively choosing the bonding types in the

system allow us to determine the relative extent to which covalent bonds or non-bonding interactions governed the thermal conductance between polymer chains. All non-bonding interactions in the system were included in the first set of simulations to achieve the total thermal conductance between the chains, whereas in another set of simulations the non-bonding interactions of the crosslinking agents were removed (i.e., the vdW and Coulombic interactions that the atoms of the crosslinking agent can create were removed). Lastly, all non-bonding interactions in the system were removed in the final set of simulations.

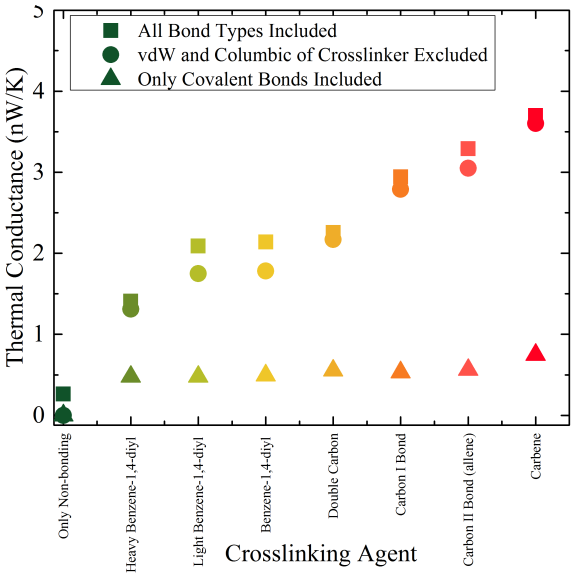
All Bond Types Included
vdW and Columbic of Crosslinker Excluded
Only Covalent Bonds Included
Thermal Conductance (nW/K)
0
1
2
3
4
5
Only Non-bonding
Heavy Benzene-1,4-diyl
Light Benzene-1,4-diyl
Benzene-1,4-diyl
Double Carbon
Carbon I Bond
Carbon II Bond (allene)
Carbene
Crosslinking Agent

(a)

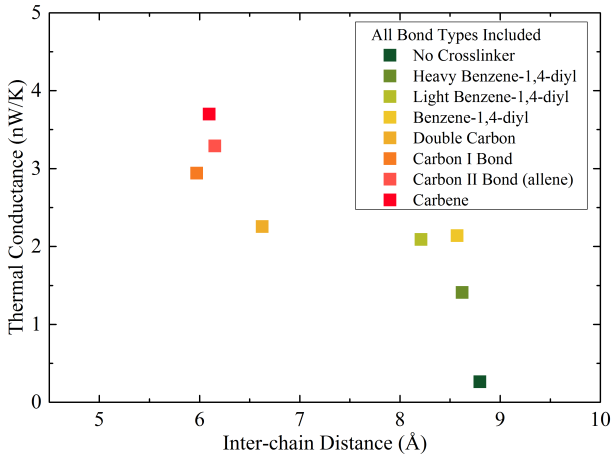
All Bond Types Included
No Crosslinker
Heavy Benzene-1,4-diyl
Light Benzene-1,4-diyl
Benzene-1,4-diyl
Double Carbon
Carbon I Bond
Carbon II Bond (allene)
Carbene
Thermal Conductance (nW/K)
0
1
2
3
4
5
5
6
7
8
9
10
Inter-chain Distance (Å)

(b)

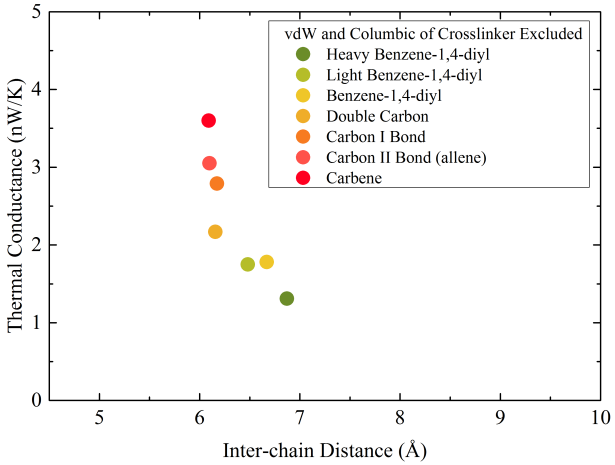
vdW and Columbic of Crosslinker Excluded
Heavy Benzene-1,4-diyl
Light Benzene-1,4-diyl
Benzene-1,4-diyl
Double Carbon
Carbon I Bond
Carbon II Bond (allene)
Carbene
Thermal Conductance (nW/K)
0
1
2
3
4
5
5
6
7
8
9
10
Inter-chain Distance (Å)

(c)

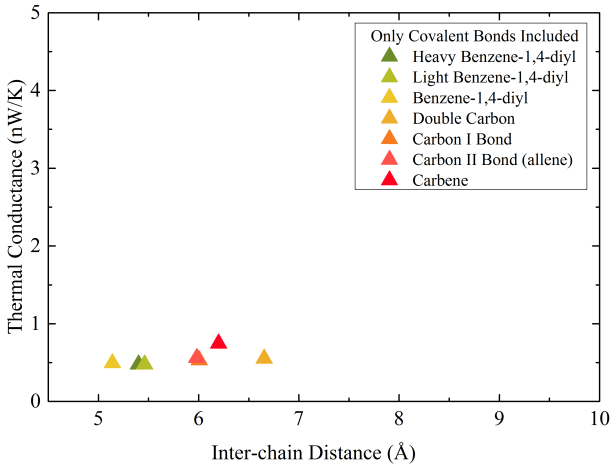

(d)

Figure 3.5: Inter-chain thermal conductance for different conditions in bonding. (a) Thermal conductance between polymer chains with different crosslinking agents under different conditions for non-bonding interactions. A considerable drop in thermal transport between the chains is observed when non-bonding interactions are completely removed from the system (triangles). (b) Inter-chain thermal conductance when all non-bonding and bonding interactions are present. (c) Inter-chain thermal conductance when non-bonding interactions of the crosslinking agents are removed from the system. In this case only atoms in the polymer chains can interact through non-bonding interactions. (d) Inter-chain thermal conductance when all of the non-bonding interactions are excluded from the system. Once all of the non-bonding interactions are removed from the system, the chains get closer to each other because of the absence of the repulsive portion of the non-bonding interactions.

The results for thermal conductance between the chains for these various bonding situations are shown in Figure 3.6(a). Since non-bonding interactions are strongly dependent on inter-chain distance, the results of Figure 3.6(a) are plotted against their respective inter-chain distances. These plots are shown in Figures 3.6(b),3.6(c),3.6(d).

As shown in Figures 3.6(b) and 3.6(c), generally, thermal conductance between chains is inversely related to the inter-chain distance, thereby enhanced as inter-chain distance is reduced. This is only true for cases in which non-bonding interactions are present. A similar relation is not observed for cases where only covalent bonds transfer heat in the system (Figure 3.6(d)). As shown in the Equation 3.2, non-bonding interactions are a function of inter-chain distance. Thus, inter-chain distance severely

affects the strength of inter-chain non-bonding interactions. The highest thermal conductance between the chains is observed in the chains that are crosslinked with CH_2 crosslinkers. This increase in thermal conductance between the chains can be explained by the enhanced non-bonding interactions between the chains. The change in the inter-chain distance is caused by the short length of the CH_2. The polymer chains crosslinked with CH_2 are at an inter-chain distance that is smaller than the effective distance for non-bonding interactions (2.5 times greater than the Lennard Jones σ parameter, which is usually used in molecular dynamics simulations as a cut-off for vdW forces [168]. Beyond this point the vdW forces are very weak and negligible.). Thus, for the system crosslinked with CH_2, non-bonding interactions are important and significantly contribute to inter-chain thermal transport.

Once all non-bonding interactions are removed, the covalent bonds that crosslinkers create between the polymer chains are the only heat transfer pathway between the chains. As shown in Figure 3.6(d), the removal of non-bonding interactions causes a notable reduction in thermal conductance between the polymer chains. Such a drastic reduction in inter-chain thermal conductance proposes that enhancement in inter-chain non-bonding interactions account for the majority of heat transfer between the crosslinked polymers.

Consequently, our work has made it evident that a crosslinking agent that draws the polymer chains closer together has a higher influence on inter-chain thermal conductance in polymers. Furthermore, a natural question that arises from our analysis so far is whether the portion of heat that is being transferred through the crosslinker covalent bonds is affected by the inter-chain distance or not. In other words, is it possible that the reduction in thermal conductance observed in Figure 3.6(d) is because of a reduction in heat transfer through covalent bonds caused by a reduction in inter-chain distance?

To examine this hypothesis, we calculated the inter-chain thermal conductance

between polymer chains crosslinked with carbene as a function of inter-chain distance in the absence of non-bonding interactions. In order to control the inter-chain distance for the system, the chains are moved with respect to each other to create different inter-chain distances. This manual adjustment of inter-chain distance simulates the situation in which the inter-chain distance was larger in the presence of non-bonding interactions. Adjusting the inter-chain distance in this manner will result in some tensile stress in the system. These results are reported in Figure 3.6. The results of these simulations show that when non-bonding interactions are removed, there is no evident relation between the inter-chain thermal conductance and the inter-chain distance. Therefore, the results in both Figures 3.6(d) and 3.6 together show that the inter-chain heat transfer through a crosslinkers covalent bonds is not a function of inter-chain distance. Therefore, it can be deduced that the difference in thermal conductances observed between Figure 3.6(b) and Figure 3.6(d) is mainly caused by the removal of non-bonding interactions.

The results obtained here can be compared with previous studies on heat transfer through non-bonding and bonding interactions. For example, results of a previous study by Eiermann[38] suggest that covalent bonds can transfer heat at a 10 fold higher rate than vdW interactions. However, it should be noted that the Eirmanns results apply to heat transfer through a single vdW bond in comparison to heat transfer through a single covalent bond. This is different than our simulations. Our simulations account for contributions of all possible non-bonding interactions in the system (as mentioned in the previous section, we set a cut-off for non-bonding interactions that is longer than the size of the box, which allows us to include all of the possible non-bonding interactions in our simulation). Because we include all interactions, there is a far greater number of non-bonding interactions available compared to the number of covalent bonds of the crosslinkers. Thus, this abundance of non-bonding interactions leads to greater inter-chain thermal conductance. In essence,

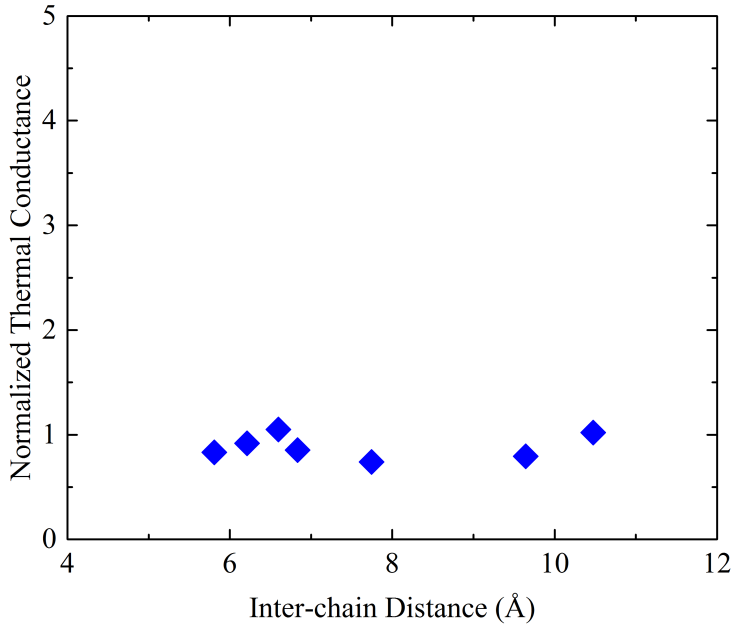

Figure 3.6: Thermal conductance between two PMMA chains crosslinked with carbine agent as a function of inter-chain distance

the crosslinking agents with a short length (comparable or smaller than the radius of effectiveness of non-bonding interactions) boost non-bonding interactions by reducing the inter-chain distance, and these enhanced non-bonding interactions (which are abundant in number) result in a large contribution to inter-chain thermal transport.

The findings of this section can be used to justify some of the discrepancies about heat transfer in crosslinked polymers that are reported in the literature. For example, in the study by Yu et al.[195], thermal conductivity of crosslinked polyethylene was reported to drop as the polymer was crosslinked with the dicumyl peroxide agent. Since the length of this crosslinking agent is relatively long, it may result in an increase in inter-chain distance between the chains, which would result in a lessening of non-bonding interactions between the chains. The reduced density reported after crosslinking the polyethylene chains could be an indication of increased inter-chain distance. As another example, Kikugawa et al.[78] reported that the simulated thermal conductivity of crosslinked polystyrene did not increase even at high crosslinking

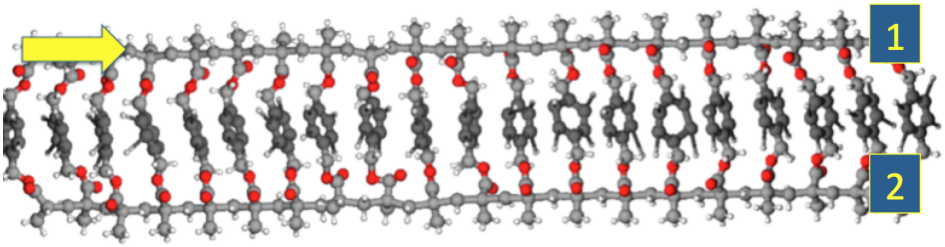

Figure 3.7: Simulation system to analyze the wave propagation velocity in the polymer system. The initial point where propagation began is shown at the top left. The wave is later detected at locations 1 and 2.

densities. Based on the results in this section, this could be due to the large size of the benzene ring at the side of the polystyrene mers. Such a bulky side group would prevent the chains moving closer together, resulting in almost no change in thermal conductivity even at high crosslinking densities. A question that arises here is how can non-bonding interactions affect thermal conductance between the chains?

The long rage nature of non-bonding interactions (compared to the short range nature of covalent bonds) gives them interesting properties for thermal transport in polymer chains. The impact of this long-range nature of non-bonding interactions on wave propagation in polymers is studied through analysis of propagation of a wave between the chains of a crosslinked polymer. The simulation system is shown in Figure 3.7. The temperature of the system is cooled down to 0K in order to avoid any thermal molecular motion. Then, a 1 THz wave is created at the "pump" location. This 1 THz wave represents a wave that carries heat at room temperature [137, 134].

The results for this wave propagation analysis are shown in Table 3.2. A 9-fold increase in wave propagation velocity in the polymer chains is observed when the non-bonding interactions are present compared to the case where non-bonding interactions are removed from the system.

The results of the wave propagation analysis agree with previous results for heat transfer in crosslinked polymers in this section. Indeed, the wave propagation analysis shows that non-bonding interactions can transfer energy at a faster rate due to

Table 3.2: Normalized wave propagation velocities in polymer system in the presence and absence of non-bonding interactions

Probe Location	All bonding included	Non-bonding excluded
1	1.00	0.17
2	0.84	0.09

their long-range nature, however they do this most effectively when they are strong. Further wave propagation analysis showed that acoustic waves with relatively low frequencies (∼10THz) propagate faster in the presence of non-bonding interactions, however high frequency oscillations (∼100THz) mostly travel through covalent bonds even in the presence of non-bonding interactions.

3.3.2 Effects of Vibrational Density of States of Crosslinkers on Inter-chain Heat Transfer

The results of the previous section showed that thermal transport in crosslinked polymer chains is significantly affected by non-bonding interactions and shorter crosslinkers that enhance these interactions should result in a higher inter-chain thermal conductance. However, some of the results in Figure 3.6(b) show slight differences with this conclusion. For instance, polymer chains crosslinked with CH_2 have a higher thermal conductance than polymers crosslinked with Carbon I bond, while the inter-chain distance for the former is slightly greater than that of the latter. In order to find the underlying reason for this deviation, we studied the vibrational density of states (VDOS) of the crosslinking agents and the polymer chains. Velocity autocorrelation method was used to calculate the VDOS of these systems [130] using the following equation:

$$VDOS(\omega) = \frac{1}{\sqrt{(2\pi)}} \int_0^{+\infty} e^{-i\omega t} \frac{< v_t \times v_0 >}{< v_0 \times v_0 >} dt \tag{3.6}$$

Previous studies have used this method to calculate the VDOS of different materials [71, 153, 128, 117, 37, 44, 97, 98, 196, 86, 134]. After analyzing the atomic

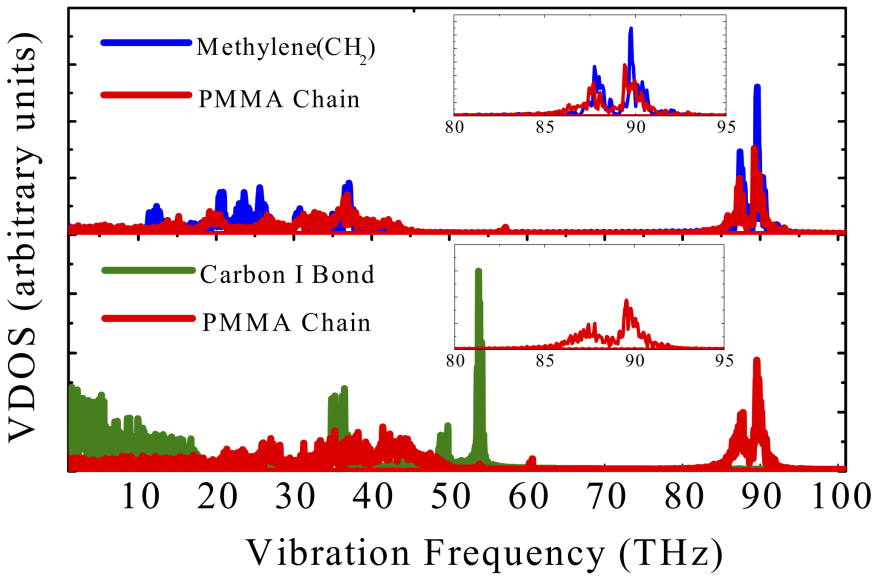

Figure 3.8: VDOS of different crosslinkers and PMMA chains.

trajectories, the VDOS values are calculated using Equation 3.6. The partial VDOS results are shown in Figure 3.8. This figure compares the VDOS of the crosslinking agent with the VDOS of the main polymer chain. A substantial overlap in the VDOS of PMMA chain and the VDOS of the CH_2 agent is observed. However, the VDOS of the carbon I bond crosslinking agent does not have as large of an overlap with the main PMMA chain as carbenes VDOS. The overlap of common modes results in higher rates of heat transfer between the materials. This has been observed in previous studies as well [134, 39, 51]. It is important to consider that MD simulations carried out here are in the classical physics domain. Therefore, although the population of phonons with a frequency around 80 THz should be low at room temperature, the MD simulations do not consider quantized effects.

3.3.3 Effects of Density of Crosslinking on Heat Transfer in Crosslinked Polymer

Previously in this chapter it was mentioned that while high crosslinking densities near 100% are usually seen in epoxies and resins [78], PMMA chains crosslinked up to 100% may not be practical. However, we studied the effects of crosslinkers on heat transfer in a 100% crosslinked PMMA system in order to understand the maximum effect of crosslinking on heat transfer. In this section, PMMA chains with lower crosslinking densities are examined in order to ensure that the finding in the previous section still holds at lower crosslinking densities. For these simulations, two PMMA chains crosslinked with carbine at various crosslinking densities are modeled. Then, the inter-chain thermal conductance for these systems is calculated twice, once in the presence of all bonding types and once in the absence of non-bonding interactions. The results for inter-chain thermal conductance in these two cases are shown in Figure 3.9.

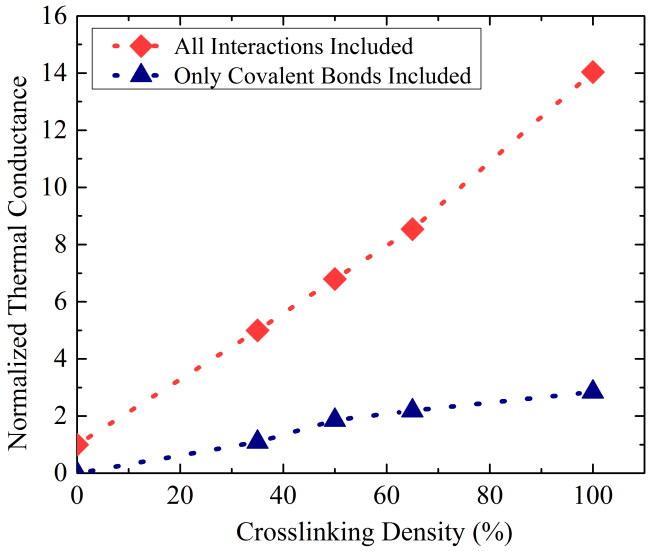

Figure 3.9: Inter-chain thermal conductance as a function of crosslinking density. A near linear relation between the crosslinking density and inter-chain thermal conductance is observed up to a crosslinking density of ∼65%. For crosslinking densities above 65%, a slight deviation from the linear relation is evident. This deviation is likely due to short inter-chain distances at 100% crosslinking density, that have happened due to the tacticity of polymers in this simulation.

As expected, as crosslinking density is increased, thermal conductance between the chains is also increased. This is due to the addition of new heat pathways between the chains, either through covalent bonds of crosslinkers or the enhanced non-bonding interactions between the chains. It should also be noted that the increased crosslinking density might increase the stiffness of the entire structure, which could in turn increase the thermal conductance in the material.

In order to understand the impact of non-bonding interactions on heat transfer between the chains for various crosslinking densities, the inter-chain distance as a function of crosslinking density is plotted in Figure 3.10. An inverse proportionality between the inter-chain distance results and the inter-chain thermal conductance results is observed across different crosslinking densities. This means that as the crosslinking density is increased, the inter-chain distance is reduced, which in turn

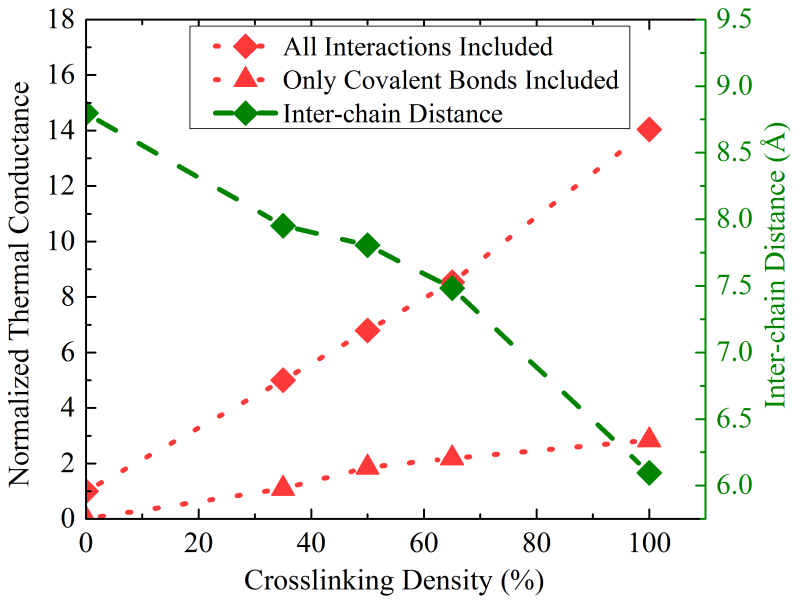

Figure 3.10: Dependence of heat transfer and inter-chain distance on crosslinking density. PMMA polymer chains in this simulation are crosslinked with CH_2

enhances the inter-chain non-bonding interactions. These enhanced interactions allow a higher rate of heat transfer between the chains.

3.3.4 Effects on Non-bonding Interactions on Inter-chain Heat Transfer in the Absence of Crosslinkers

In the previous section, the effect of crosslinkers on heat transfer between the polymer chains were studied. It was shown that heat transfer through non-bonding interactions plays an important role in heat transfer in crosslinked polymers. Thus, a short crosslinker that can bring the chains closer will result in a higher enhancement in thermal conductance at the junction of the polymer chains. Thus, a question that comes up is this: if non-bonding interactions are responsible for enhanced heat transfer in crosslinked polymers that are crosslinked with a short crosslinking agent, would they increase heat transfer between two polymer chains in the absence of crosslinkers, if the distance between polymer chains were manually changed? Furthermore, the re-

sults of Figure 3.9 suggest that the amount of heat transfer between polymer chains scales linearly with respect to the crosslinking density, regardless of the presence or absence of non-bonding interactions. Given this observation, how does the inter-chain heat transfer through only non-bonding interactions scale with respect to inter-chain distance?

To answer these questions, two long parallel polymer chains were simulated. Each polymer chain possessed 120 mers. Three different polymers, namely, PMMA, PE, and PVA, were studied to ensure the generality of our results. The geometry and input data files for polymer chains were created using nanoHUB Polymer Modeler[56]. The force field for PE chains was also derived from [56]. The force field values were current at the time of simulation. Force field is DREIDING [104]. The Lennard-Jones parameters from OPLS [72] force field were used here, since they produced better bulk properties. In order to model the PVA chains, the force-field developed by Muller[112] was used; however, since this force field considers constant bond lengths, the stiffness values for the bonds where taken from the OPLS force field[72]. In order to ensure that using these stiffness values did not change the equilibrium bond lengths described in [112], the length of these bonds during simulation are calculated and reported in Figure 3.11. This figure confirms that using the stiffness values from OPLS model, the bond lengths remain near their equilibrium values. The reason behind using a variety of force fields[56, 23, 112] is to ensure the results are not force field dependent. Similar to previous sections, NEMD was used to calculate the inter-chain thermal conductance. In this section, a time step of 0.5 fs was used, instead of the 1fs time step that was used previously. Similar to the previous section, cut-off values for the non-bonding interactions were chosen to be longer than the simulation box. The inter-chain interactions were calculated by analyzing the atomic trajectories. In order to quantify the interactions between the monomers in different chains, the following method is defined. The distance between the centers of mass of different monomers

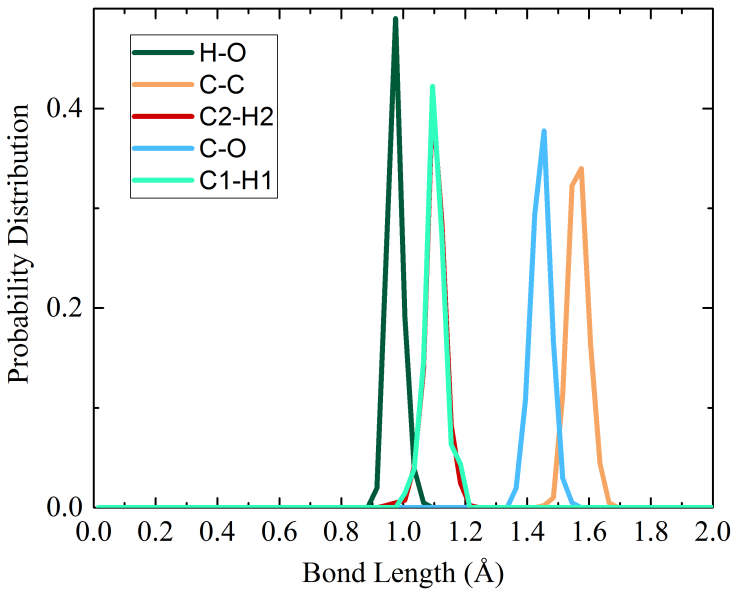

Figure 3.11: Bond length for PVA during simulation in order to confirm that choosing OPLS force field values for bond stiffness does not change average bond length.

is calculated. Then, any two monomers whose centers of mass are in a distance of less than the radius of effectiveness of non-bonding interactions [168] are considered interacting monomers. Figure 3.12 is a visual representation of the method used to calculate the number of interacting monomers.

After calculating the number of monomers that are in interaction, the average of interactions per monomer is calculated for each system. Next, the thermal conductance values are plotted as a function of the number of interacting monomers. The results are reported in Figure 3.13.

Figure 3.13 shows that the inter-chain thermal conductance between the chains has a linear relation with respect to the number of monomers interacting between the chains. Additionally, each type of polymer chains possesses its own unique slope. These slopes could be used to derive new theoretical models for heat transfer in polymers or could be used to enhance the existing models [206, 75]. In addition, there is a convincing relation between the number and strength of the non-bonding

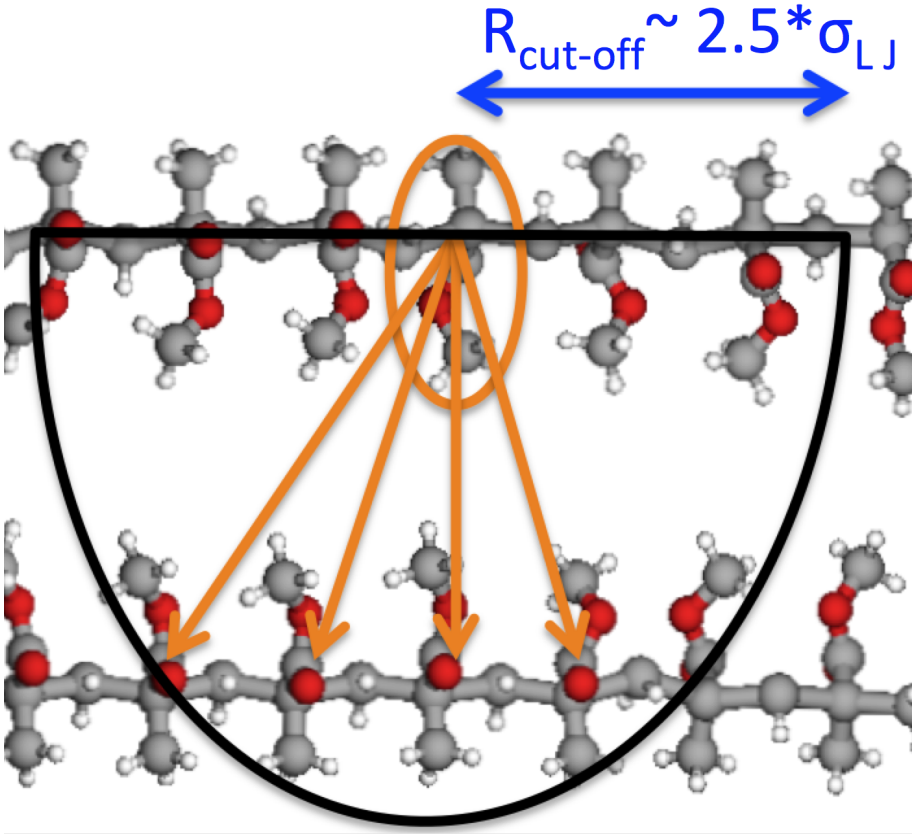

Figure 3.12: Method of finding the number of monomer that is interacting. First, centers of mass of monomers are calculated. Then, the distance between the center of mass of one monomer with other monomers is compared with the radius of effectiveness of vdW interactions. If the distance is smaller than radius of effectiveness, the monomers are counted as interacting.

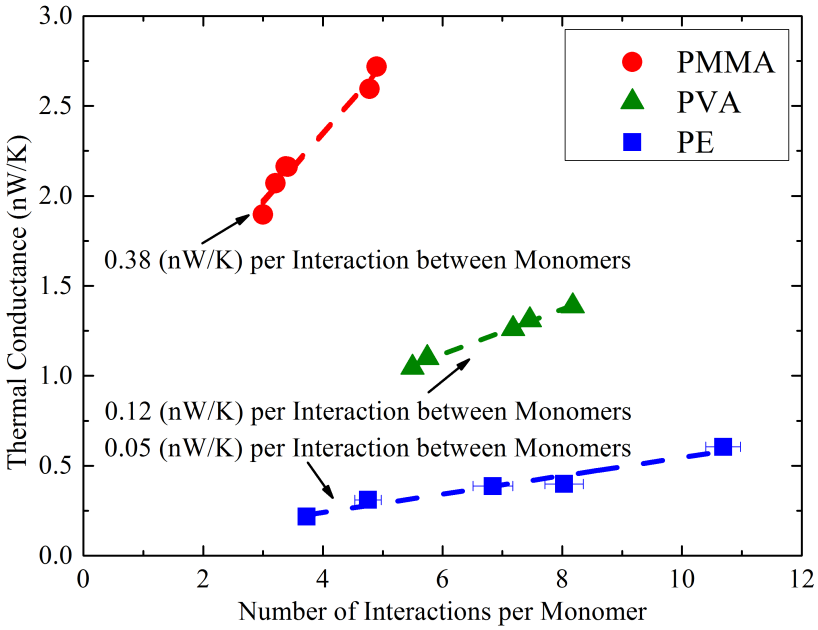

Figure 3.13: Inter-chain thermal conductance as a function of average number of monomers in one chain that are interacting with monomers from the other chain. The results are linear and a unique slope is observed for each polymer type.

interactions of the three different polymers studied here and the slopes shown in Figure 3.13. For example, the PE polymer has only 6 atoms per monomer, thus if two monomers from this polymer interact, there will be 6x6 non-bonding interaction pathways for heat transfer. However, this number is 7x7 for PVA and it is 15x15 for PMMA. Thus, PMMA would have the highest number of pathways per interacting monomers.

3.3.5 Effects on Ionic Bonding on Heat Transfer in Polymers

As a means to control the inter-chain interactions, the previous section examined the effects of vdW, electrostatic, and covalent bonds on heat transfer in polymers. Ionic bonding is another type of inter-atomic interaction that can affect the inter-chain interactions. As discussed above, weak inter-chain interactions are the main bottleneck for low thermal conductivity of polymers. Furthermore, the wave transport

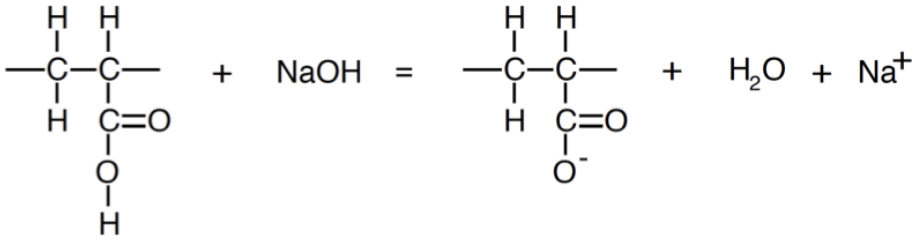

Figure 3.14: Ionization reaction of PAA and NaOH

study in a previous section shows that a stretched and straight polymer backbone would be ideal to enhance heat transfer along the polymer chain. In fact, both experimental and numerical studies have also shown that stretched polymer chains can have very high thermal conductivity. Most of the previous studies have stretched the polymer chains using mechanical force or methods such as electrospinning. However, recent studies show that some polymers may exhibit chain stretching without the need of mechanical force. In this section, we study the effects of ionic bonding on the conformation of the polymer chains, and ultimately on heat transfer. In a previous study, ionization of PAA polymer chains is shown to result in increased persistence length of the polymer [31]. This increase in radius of gyration could result in enhanced heat transfer along the polymer chain.

We use a system made of PAA polymer chains ionized with NaOH. The reaction is shown in Figure 3.14. Periodic boundary conditions are used and the EMD method described in section 2.2 was used to calculate the thermal conductivity of the system. The results are shown in the Table 3.3. The results here show that the ionic bonds between the polymer chains and the sodium ions have stretched the polymer chains. This stretch in the radius of gyration shows that the chains are being stretched and thus heat transfer along the chains is improved. Similar behavior has recently been reported through experimental results [152].

Table 3.3: Effects of Ionic Bonding between Polymer Chains on Heat Transfer in Polymers. k represents thermal conductivity.

Material	Radius of Gyration (Å)	Density (g/cm3)	k (W/mK)
PAA	7.89+/-0.67	1.47	0.29
Ionized PAA	9.28 +/- 0.9	1.73	0.56
Net Change	17.6%	19%	93%

CHAPTER IV

Machine Learning Algorithm for Fast Thermal Properties Prediction and Materials Discovery

4.1 Introduction

A bottleneck in the use of machine learning algorithms to predict material properties is the limited amount of data available to train them, relative to other machine learning applications such as face identification, digit recognition, text recognition, and natural language processing. This lack of training data arises from the time-consuming and expensive nature of computational and experimental techniques used to generate such data. For example, density functional theory (DFT) and molecular dynamics (MD), two methods widely used to generate materials databases, have significant computational requirements and often require hundreds of CPU hours to calculate the properties of a simple material. The challenge of relatively sparse training data is compounded for material properties that are associated with a large number of features, such as thermal property predictions that depend not only on material properties but also environmental properties (e.g., temperature).

In this work we demonstrate the encoding of physical laws in machine learning algorithms as a means to address the prediction of material properties for which training data is sparse relative to the number of features. This encoding constrains

the algorithm to search only the sample space where defined physical rules are valid, thus eliminating some of local minima that are known a priori as non-physical and improving the iteration path.

We choose thermal conductivity as platform for this technique, recognizing the numerous features on which thermal conductivity may depend as well as its technological importance for a wide range of applications including electronics packaging [45], thermal insulation, thermal interface materials, thermal barrier coatings, and thermoelectric energy conversion [80]. Heat can be conducted by electrons (as prevalent in metals) or vibrations (as prevalent in dielectric materials). Vibrational transport can occur by quantized, propagating collective excitations known as phonons (prevalent in crystalline solids) or short-range diffusive coupling (often prevalent in amorphous solids)

Heat is primarily carried in electrically non-conducting crystalline materials by a spectrum of phonons, quantized vibrational modes of atoms that each have a certain frequency, lifetime, and velocity. These characteristics, which determine the amount of heat each mode carries [107], depend on a number of material and environmental parameters[172] including atomic mass, density, temperature, lattice structure[172], atomic number, sample size [134], sample morphology, and type of bonding between atoms [133]. The large number of these parameters and the complex manner in which they affect thermal conductivity have impeded the understanding of thermal transport in existing materials and hampered the design of novel materials.

To determine thermal conductivity, both numerical methods [89, 166], such as density functional theory and molecular dynamics, and experimental methods, such as the three-omega technique[14] and time-domain thermoreflectance (TDTR) [19, 15], have been developed. Drawbacks of these methods include significant time requirements, expensive equipment, inaccuracy due to approximations (e.g., existing numerical force fields are usually only suitable for pure materials and not available for all materials),

length scale limitations, and numerical rounding errors.

Calculation of thermal conductivity consists of several steps that may differ greatly in their computational requirements. For instance, of the three frequency-dependent parameters(phonon velocity, heat capacity, and lifetime) that must be calculated in order to in turn calculate the total thermal conductivity, computation of phonon velocities and phononic heat capacity only requires the calculation of harmonic force constants between the atoms, which is relatively fast. However, in order to estimate the phonon lifetimes, we need to calculate anharmonic force constants, which require higher order force calculations[89]. Accelerating these calculations would not only significantly enhance our understanding of existing materials but also increase the capability for high throughput materials discovery with desired properties[134, 133, 131].

This task may be achieved using machine learning (ML) algorithms, which are usually applied to derive very complex underlying relations in a dataset[47, 88, 93]. In this work, we demonstrate the application of ML algorithms to learn the relationships between material thermal conductivities and easily measurable material properties (such as mass, density, atomic number, phonon velocity, etc.). These relationships will allow us to predict material thermal conductivities without performing time-consuming third-order force constant calculations. We also use ML to calculate the relative contributions of phonon modes with different frequencies to the total thermal conductivity, recognizing the importance of this frequency dependence to the design of materials for phonon filtering [82, 113], improved thermal boundary resistance in heterostructures[134, 52], phonovoltaic devices [108], and thermoelectric devices [80].

These predictions help us to understand the relationships between the numerous relevant material parameters as well as facilitate the more rapid design of materials with desired thermal properties. In a recent study, analytical models were developed to predict phonon lifetimes based on second order force constants [157]. The main

drawback of this method is that the total thermal conductivity of a material must be known beforehand in order to calculate its phonon lifetimes, which limits its application to materials discovery. Here we demonstrate a method that after training can achieve this task without any previous knowledge about a materials total thermal conductivity.

We apply supervised learning techniques with total thermal conductivity as the output of the algorithm. However, the network is set up in such a way that frequency dependent thermal conductivity values should be derived from internal parts of the network. This is because the network must follow the physical rules that we have encoded in it. Thus, for frequency dependent thermal conductivity predictions stand point, the algorithm could be considered "semi-supervised". This is because the network does not need to explicitly know the frequency dependent thermal conductivity values for training. This stands in contrast to previous applications of ML for materials discovery, which have primarily been based on supervised learning [67, 123, 160, 209, 140, 178, 34, 129, 50, 109, 124, 193, 20, 10, 36, 12, 32, 101, 21, 149, 141, 111, 99, 183, 91], a method in which the machine learns how to generate outputs from inputs after seeing a certain number of input/output pairs. The disadvantage of supervised learning is that we need to have input data that is labeled with a corresponding output value. For example, when generating the frequency-dependent contributions to thermal conductivity, these values are unknown and thus we cannot use supervised learning to train the algorithm. Thus, we have developed a custom designed algorithm to address this issue. Furthermore, we developed a fully automated model in which the machine only directly receives graphical images of a material's phonon dispersion curves and learns how to relate features in these curves to thermal conductivity. A brief description of machine learning is given in the following section.

4.1.1 Machine Learning Overview

Machine learning algorithms are methods that are able to learn the underlying relations in a dataset without being previously programmed to know such relations [70]. In machine learning, a set of inputs (features) can be used to find functions that would map these inputs to desired outputs. Machine learning algorithms can be classified into three general brackets: supervised learning, unsupervised learning, and semi-supervised learning [70].

Supervised learning algorithms find relations between input features that are labeled with an output value. Unsupervised learning algorithms find relations in input features that are not explicitly assigned to a label. Clustering algorithms are usually unsupervised learning. These algorithms try to cluster the dataset in different categories based on the distribution of different features. Finally, semi-supervised algorithms use both supervised learning and unsupervised learning. Usually when only a small portion of the data is labeled and the majority of data is unlabeled, semi-supervised learning methods can be helpful to take advantage of both labeled and unlabeled datasets. More information can be found here [70, 3].

During the process of training, the learning algorithm finds the underlying relations in the dataset by finding relations that best describe the underlying distributions in the dataset. After training, the trained model can be deployed to make predictions for input values that it has not seen a priori. This capability of machine learning algorithms to make predictions based on historical data has made them applicable in many areas including materials science [178, 34, 129, 50, 109, 124, 193, 20, 10, 36, 12].

Among many algorithms, principle component analysis, regression trees, and neural networks are particularly used in this thesis for prediction of material properties. A brief introduction to these methods is provided in the following sections.

4.1.1.1 Principle Component Analysis

Usually a dataset has two main dimensions. The first dimension is the number of samples of data. For example, for a material dataset, the first dimension is the number of materials or examples in the dataset. The second dimension is features or predictors. The second dimension contains the parameters for each one of the data points in the first dimension. For the material dataset, the second dimension could be the material properties associated with each material. Often times we do not know the exact importance of the predictors for prediction of the target values. Thus, algorithms that would provide some information about the importance of each variable would be very useful in reducing the dimensionality of the training dataset. Dimensionality reduction not only would reduce the computational burden (due to a lesser number of predictors, once the unimportant predictors are removed), but may also avoid confusion of the machine learning algorithm and overfitting. Principle component analysis (PCA) is a method that can be used for dimensionality reduction in a dataset [70, 3]. Using dimensionality reduction methods could be very important for material datasets, where the features could be highly correlated. For example, mass, lattice constant, and density could be significantly correlated, thus the presence of all of them in a dataset as predictors may not really help the algorithm to find any new insight.

PCA is a method that finds the principle components of a dataset. PCA finds the principle axis through centering and rotation of axis. Principle components are along the axis that the variance of data is maximum along those axis. For example, let's assume that we have two predictor variables, x_1 and x_2. We construct both x_1 and x_2 such that they contain 100 integers from 1 to 100. We then add some random noise from a uniform distribution to the values (random noise values chosen have a range of 0-10). Figure 4.1 shows the values for each one of these predictors. For small amounts of noise, the values in predictor x_1 should linearly correlate with values in x_2 (for the

example shown in 4.1, the Pearson correlation between predictors is 0.99). Thus, the information in x_2 does not add any new information. If we rotate the axis of the dataset 45 degrees counter clock-wise (which would result in a new axis as shown in Figure 4.1(c)), we can capture most of the variation in the data, while the other axis would mostly represent the noise. Using this method, we have captured most of the variation in the data in one variables and if we discard the second principle component, we would not lose much information (in this example, almost no information is lost since the second component mostly shows the noise). The principle components are shown in Figure 4.2. Figure 4.2(c) shows that there is no correlation between the first and second principle components. As Figure 4.2 shows, the first principle component contains most of the information, while the second principle component mostly contains random noise. Thus, discarding the second principle component will not lead to a severe loss of information.

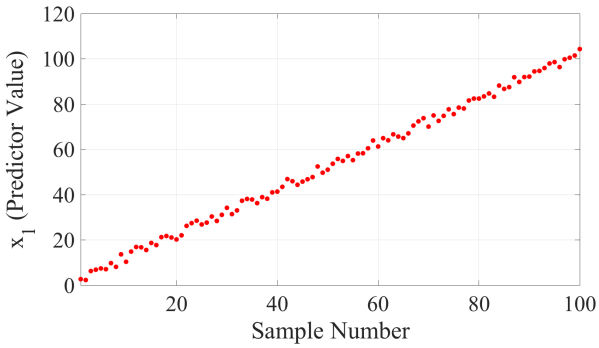

(a)

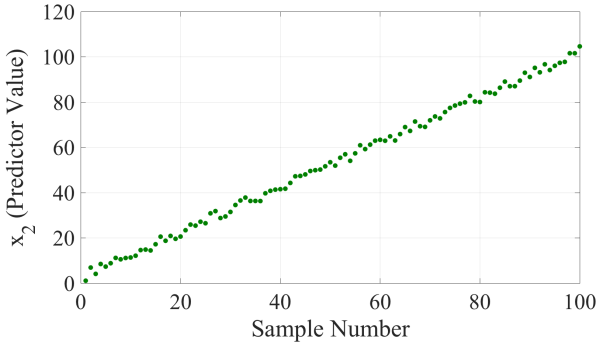

(b)

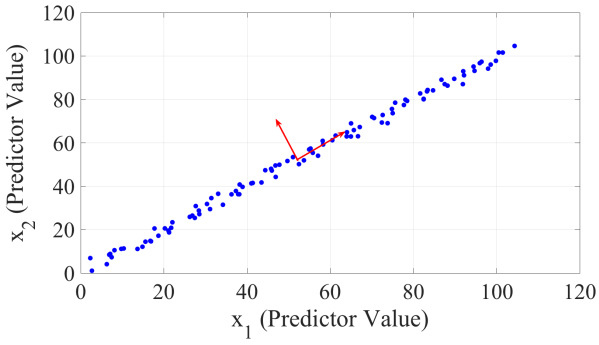

(c)

Figure 4.1

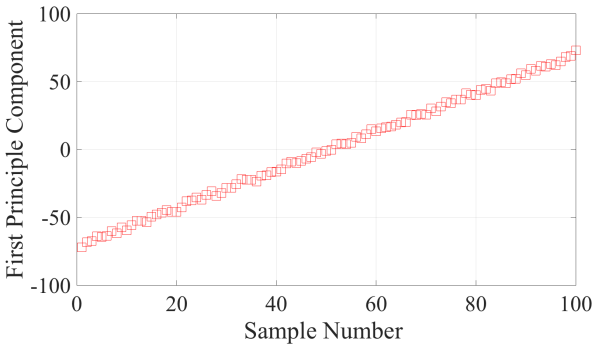

(a)

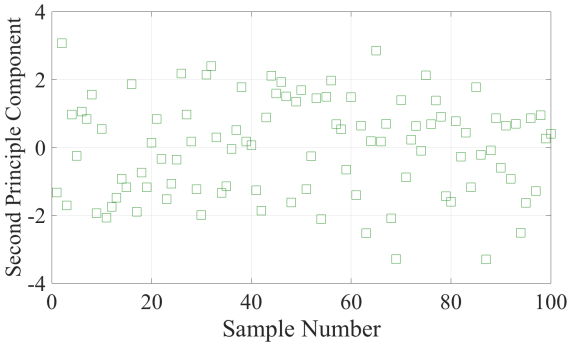

(b)

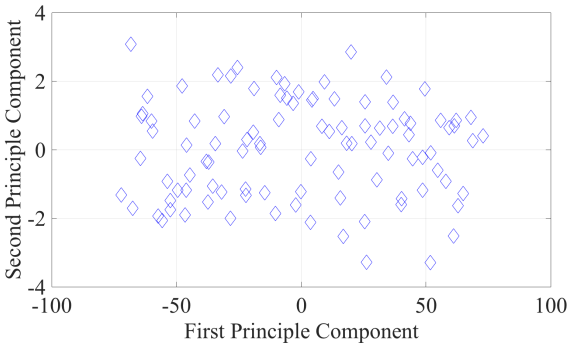

(c)

Figure 4.2

Principle components can be calculated using the covariance matrix.

4.1.1.2 Regression Trees

Regression trees are powerful machine learning algorithms that are used for both regression and classification problems. The difference between a regression tree and a classification tree is that the target values for a regression tree usually hold a continuous value, while for a classification tree, the target value is usually discrete, i.e., a class. Since thermal conductivity of materials is a continuous variable, in order to predict thermal conductivity, in this thesis we have used regression trees.

A regression tree is a tree-like structure, where the nodes are decision points. Based on the value of a predictor at the node, the algorithm decides which branch of the tree should be explored. Figure 4.3 shows a schematic view of a simple regression tree. In this figure, we have used temperature and mass of a material as predictors for thermal conductivity. Based on the values of mass and temperature, the tree guides us towards an end branch (leaf) that contains either a single value for the thermal conductivity or a simple regression model to calculate thermal conductivity.

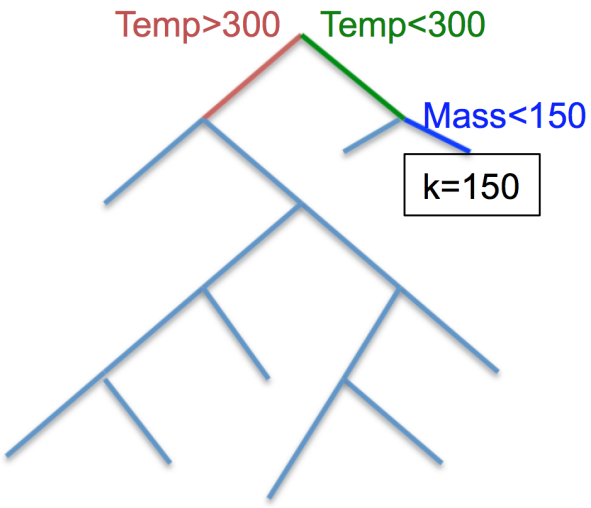

Figure 4.3: A schematic view of a regression tree for thermal conductivity predictions based on temperature and mass of the material. Based on material features, the regression tree searches its branches in order to estimate the values of thermal conductivity. The value of thermal conductivity is given at the last node (leaf) of the tree.

In order to achieve a regression tree as shown in Figure 4.3, we need to train the regression tree based on the training dataset. The training process for a regression tree consists of finding the best conditions and splits at each node of the tree. There are different methods to train a tree. One method is to start with a single initial node. Then, we can find the best split that results in smallest error in the prediction. We continue this process until the tree is trained [70, 3].

4.1.1.3 Neural Networks

Neural networks are one of the most versatile machine learning algorithms, which resemble the human nervous networks. A schematic view of a neural network is shown in Figure 4.4. Sometimes neural networks have a constant value, known as bias term. This bias term will be learned during the training process.

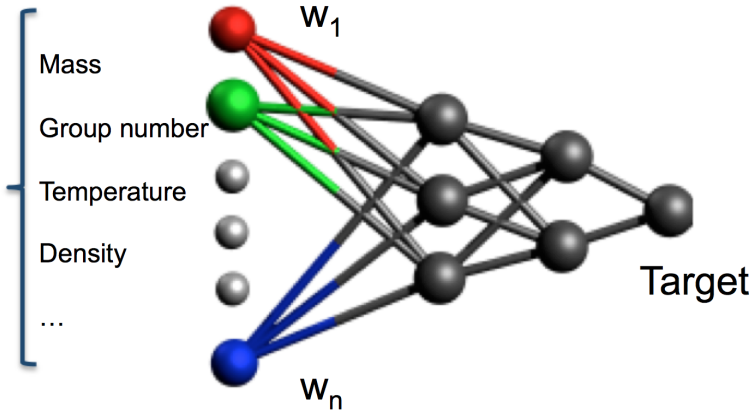

Figure 4.4: Schematic view of a multiplayer neural networks with a single output. The two middle layers are the hidden nodes. The first layer from the left side is the inputs layer and the right most layer is the output node.

Each node, or neuron, contains a computational function (activation function), several inputs, and outputs. For each input to a neuron, there is a weight that determines that relative importance of that particular input. Usually the inputs are multiplied by the corresponding weight factors and then summed up. The resulting value will be used as input to the activation function of the neuron to calculate a

value to be used in the output of the neuron.

4.2 Methods and Algorithms

We use state-of-the-art customized deep learning algorithms [88] for mining our materials property dataset for prediction of frequency-dependent thermal conductivity. Our custom designed deep neural networks will result in simultaneous prediction of bulk thermal conductivity in a supervised manner, while the algorithm will also generate the frequency-dependent thermal conductivity of materials in an unsupervised manner. We call this network specifically designed for thermal conductivity predictions: K-net (K for thermal conductivity). Neural networks are general function predictors. It is proven that given enough number of neurons, neural networks can predict any function [63]. Here, we are interested in predicting functions that can best approximate thermal conductivity of materials based on easily measurable materials properties such as mass, group number in periodic table, density, phonon velocities, specific heat capacity, phonon density of states, lattice constant, Gruneissen number, and more. All of these parameters are either easily measurable or can be calculated from second order force constants. Now to find such functions we formulate our problem in a mathematical form as shown below:

$$\exists f \in R^{+} | \tau = f(mass, latticeconstant, velocity, temperature, ...) \tag{4.1}$$

Finding such functions using neural networks requires a significant amount of training data, which is currently unavailable to us. To solve this problem, we design restricted custom designed networks based on physical restrictions of the parameter we are predicting (for example relaxation times have to be non-negative). This will allow us to eliminate some of the functions in our function space in order to find more realistic functions using significantly less amount of training data.

4.2.1 Network Architecture

We design a customized neural network for our problem with the help of the formula for thermal conductivity based on simple kinetic theory [106]:

$$K = 1/3 \sum v^2(\omega)\tau(\omega)c_v(\omega) \tag{4.2}$$

where τ is the phonon relaxation time, v is the phonon velocity, c_v is the heat capacity, and ω is the desired frequency. We define a neural network with different branches that can predict the thermal conductivity contribution for each frequency. This is somewhat similar to using convolutional neural networks [88] for image classification where each filter tries to find a certain feature in the image. Here each branch of the network tries to find the contribution of a certain frequency and then add these up to predict total thermal conductivity. In this structure, the output of the network is the total thermal conductivity, the input of the network is the materials properties, and the frequency-dependent thermal conductivity is retrieved from the hidden layers of the neural network. Figure 4.5 shows the overall structure of our network. By disconnecting (i.e. pruning) the neurons in each branch we make sure that each branch can predict the contribution of a certain frequency to thermal conductivity.

Given the formula in Equation 4.2, we try to organize each branch of the network in such a way that the initial layers are forced to predict the relaxation time for each frequency. We then take the signal from that neuron to another hidden layer where frequency-dependent velocity and specific heat information is given to the network and multiplied together to generate the contribution of that particular frequency. We then add another hidden layer to the right side of all of these branches with a single neuron to add up all of the values received from the branches to make up the overall thermal conductivity. This single node will be our output node for the network where we use it for training the network. Although our current network should have the

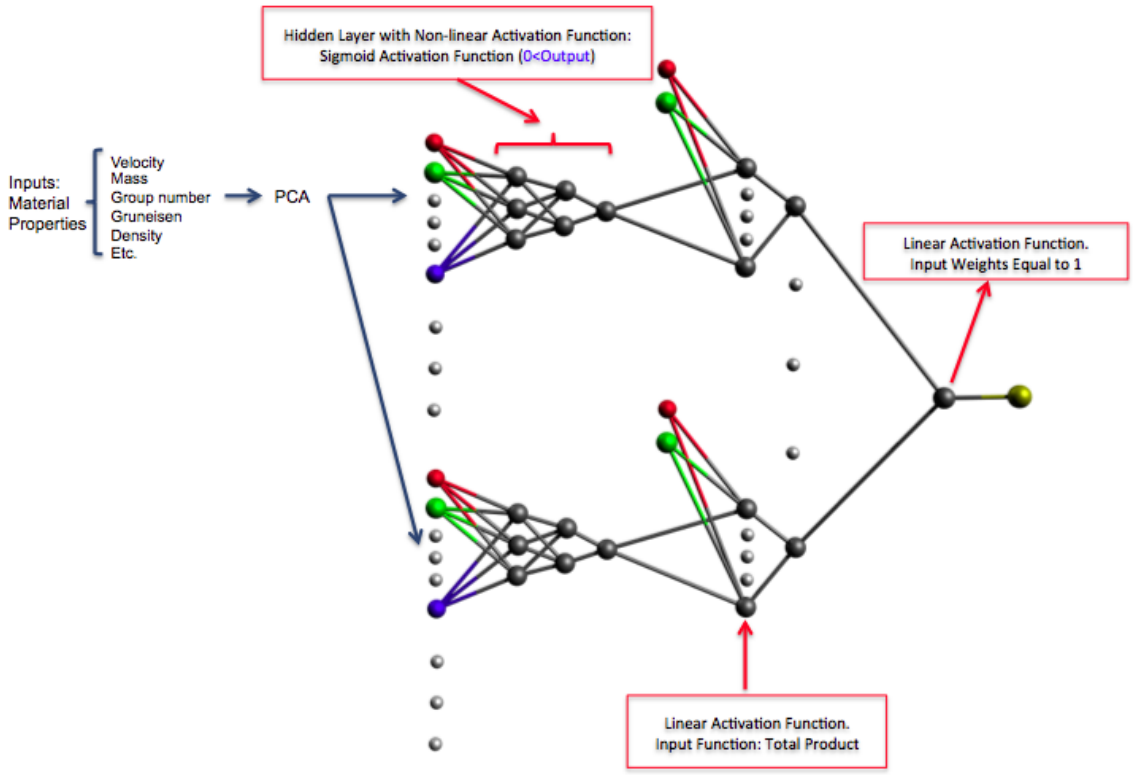

Figure 4.5: The K-net neural network architecture and data input structure. Each one of the branches in this network will predict the contribution of each frequency to the total thermal conductivity. Finally the values are all added up together to achieve the overall thermal conductivity

capability to predict the phonon lifetimes and contribution of each frequency as well as the overall thermal conductivity of materials, we would need a significant amount of data to be able to train such network. The approach to add physical rules to the network is essentially the basis for Bayesian statistics; we are constraining the function domain or the joint probability.

Considering the Spearman and Pearson rank correlations as well as other formulas reported in the literature for the relationship between phonon lifetime and material properties, we know that there could be a non-linear relationship between the input parameters and the phonons lifetimes. Using non-linear activation functions between the input features and the hidden layers connected to them, we ensure that non-linearity is provided.

Additionally, we add two hidden layers with more than one neuron after the input layers so the network would be available to explore a larger set of non-linear functions. After the input features pass through these two hidden layers, we expect the network to have predicted the phonon lifetimes. These lifetimes should be real non-negative values, thus we need to restrict the results in this node to be positive. Adding a sigmoid activation function to this layer assures that we will always have non-negative values at this node. Using such restriction will eliminate a large number of functions that the network could have explored.

Another restriction we should impose on our network is the weights of the last neuron to the right (the output neuron). These neurons should all have a fixed weights equal to one. This is because we are trying to force each branch to mine the dataset for contributions of a specific frequency. The learning rate of these weights is set to zero so that they are not updated during the training. We also chose a simple linear activation function for the output neuron so that the contributions of each frequency are simply added together to get the overall output of the network. We let the network learn the weights for the multiplication of phonon lifetime, velocity, and specific heat.

This is because the 1/3 factor is an approximation for more real cases. We also allow the network to scale the lifetime values to avoid any limitations associated with choosing the sigmoid transfer function (the output values of this function are limited to 0-1).

After setting up the network architecture, we train the network using the back-propagation method with a mean square root error function. We use Bayesian regularization for our training. This will allow us to prevent over-fitting by minimizing the weights factors as much as possible.

4.3 Data Preprocessing

The dataset in this study is provided through accurate DFT calculations, therefore for the most part our data is clean. However, we need to process our input vector to make sure that we have selected relevant features. We use Principal Component Analysis (PCA) on our input vector to reduce the dimensionality of our data. PCA transforms our data to a new basis where new features are created and ordered to give the highest variance to lowest. For DFT calculations Quantum Espresso package is used [48, 49]. We used the pseudo-potentials from http://www.quantum-espresso.org. The list of potentials is reported in Appendix A.

4.4 Results

In order to produce training data and also test the performance of the machine learning algorithm, we used DFT calculations to generate frequency-dependent thermal conductivity data for different materials. We generate a database of thermal conductivity data for materials with a cubic unit cell having two atoms in their basis as reported in Appendix B. Our database (which we restrict to temperatures between 300K and 500K) spans a range of thermal conductivities, with values as

low as a few W/mK and as high as thousands of W/mK (diamond). We solve the Boltzmann transport equation to calculate the frequency-dependent thermal conductivities of these materials over a range of 0-44 THz in 0.5 THz steps using ShengBTE [89]. Our neural network architecture therefore has 85 separate branches that each approximates the contribution of one of these frequencies.

For each material, we consider 16 input features per frequency branch to train our neural network for thermal conductivity predictions (overall our input vector has 16x85 values). First, we calculate linear correlations between the frequency-dependent thermal conductivity of materials and known or easily measurable materials properties. Figure 4.6 shows the results for Pearson correlation and Spearman rank correlations. The horizontal axis for all plots shows the phonon frequency. The vertical axis shows the correlation between the contribution of that frequency to thermal conductivity and the material parameter that is indicated on top of each plot.

The values from these correlations show how strongly we can find a linear relation between the portions of thermal conductivity that are carried at a certain frequency with a specific materials property. Figure 4.6 only shows linear relationships between input and the outputs and it considers all the input variables to be completely independent. This figure shows us that at least some linear correlation exists between the parameters, which increases the possibility of a converged algorithm. There are interesting physical insights from Figure 4.6. For example, there is a positive correlation between phonon occupation and thermal conductivity. This is indeed a correct observation, since as we increase the occupation of a mode, its contribution to thermal conductivity should generally increase. We see similar behavior for phonon velocities at moderate and high frequencies. This is also expected, since generally if phonons travel faster we should see higher thermal conductivity. An interesting observation is that materials from higher period numbers generally have lower thermal conductivities.

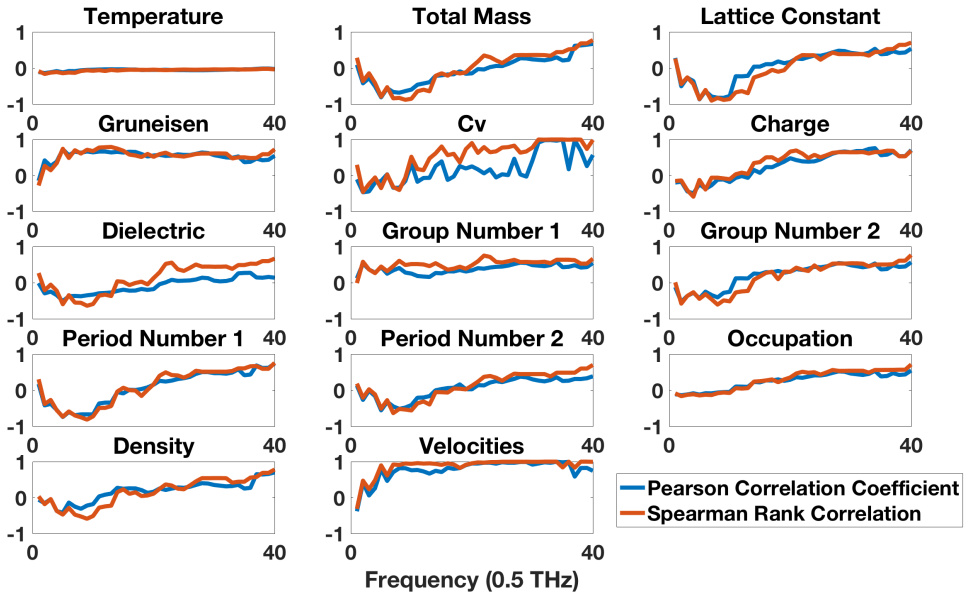

Figure 4.6: Spearman rank and Pearson correlations between input parameters and the frequency-dependent thermal conductivity values for different materials. The thermal conductivity values here are calculated using density functional theory and the solution of the Boltzmann transport equation

We see that below 20THz, if we increase the mass or lattice constant of the system, contributions of those modes to thermal conductivity decreases, however for >20THz phonons this is the opposite. The strong negative correlation around 10THz suggests that lighter materials such as silicon compared to germanium have a higher thermal conductivity at room temperature. This is because phonons with >20THz frequency have relatively high population around room temperature and the their abundance could lead to higher thermal transport. This correlation could mean that forcing lighter atoms to vibrate at room temperature might be easier and hence thermal conductivity might be higher. However, this is only a single parameter and the correlation does not take into account other parameters that can affect the thermal transport of light materials.

The most important point of Figure 4.6 is that it shows that there is some relationship between the materials properties we have chosen, and the thermal conductivity. It is also obvious that such relations are frequency-dependent and hence a single equa-

tion is not sufficient to predict frequency-dependent thermal conductivity. In order to find those functions we use the neural network architecture that is extensively explained in the methods section.

After training the network based on our database, we analyze the results. We compare the frequency-dependent thermal conductivity values that our network predicts with the values from DFT calculations. The results are shown in Figure 4.7. We see a good agreement between our results and the results from the DFT calculations. Using this methods we were able to find the frequency-dependent thermal conductivity of over 400 cases within only 100s hours of simulation. This would have taken approximately 6000 hours if we had calculated these values separately. Thus we see 10x faster calculations of thermal properties. It must be noted that the processors used for DFT and ML calculations were slightly different. Another advantage of this method is that after the network is trained, we can use it to predict thermal properties of other materials in a matter of a few seconds!

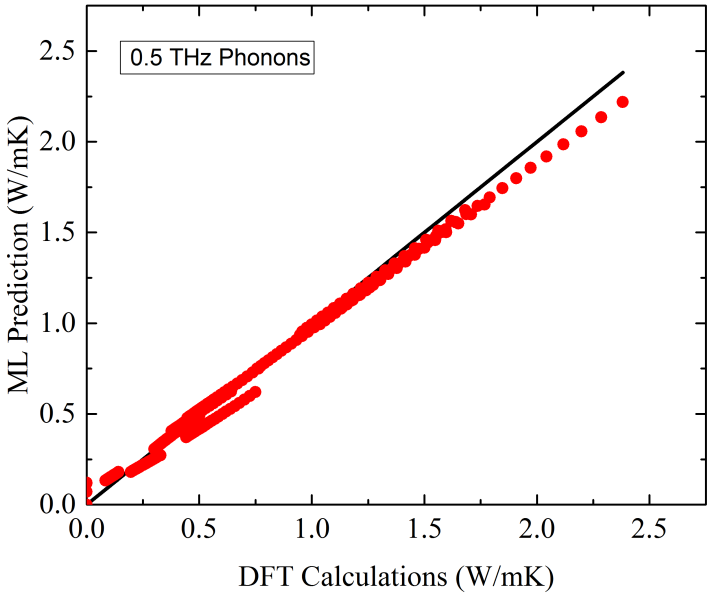

(a)

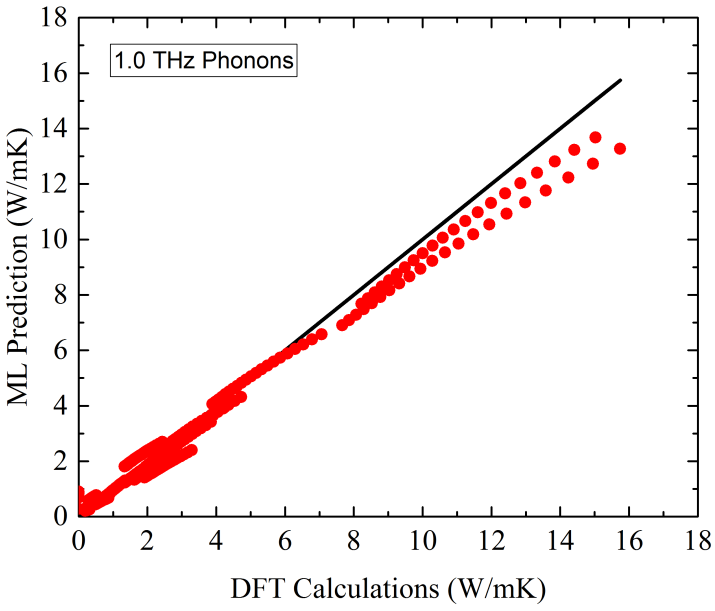

(b)

Figure 4.7: Comparison of the predicted values using machine learning algorithms developed here and the values obtained from DFT calculations.

CHAPTER V

Conclusions and Future Work

5.1 Conclusions

In this thesis, we studied nano-scale heat transfer in polymers and semiconductors. We also developed machine learning algorithms for rapid prediction of thermal properties. Our algorithms use physical rules in order to avoid exploring function areas where physical rules are broken. The results reported in different chapters of this thesis are summarized in three main areas below.

First, we used molecular dynamics to simulate strain relaxation in Si/Ge single-junction and multi-junction hetero-structures, focusing on effects of strain relaxation and interface bonds on thermal properties of these structures. Our results show that the strain at the interface of the two materials relaxes about two nanometers away from the junction. Our numerical results for strain relaxation length are in good agreement with previous experimental reports [11, 182]. This short relaxation length suggests that for a superlattice with a period length smaller than four nanometers, the strain at the interface does not fully relax. This leads to a more uniform lattice structure across the superlattice. Our numerical studies on the effects of strain on thermal boundary resistance at the interface of materials shows that the effects of varying strain on TBR are not significant. Additionally, we observe that strain relaxation does not have a significant impact on thermal conductivities of Si/Ge su-

perlattices. We observe that thermal conductivity of Si/Ge superlattices decreases as the period lengths decrease, up to a period length around strain relaxation length. Reducing the period length beyond strain relaxation length, leads to an enhancement in thermal conductivity of the superlattice. This implies that the enhancement in thermal conductivity of Si/Ge superlattices for period lengths smaller than strain relaxation length may be in part caused by uniform lattice structure due to lack of strain relaxation.

Furthermore, we calculate the PDOS of silicon and germanium in Si/Ge superlattice structures with different period lengths. We observe a new vibrational peak (12THz-15THz) in both silicon and germanium at small period lengths (comparable to strain relaxation length). Since this vibrational mode is present in both silicon and germanium, it is not significantly scattered at the interface and can transfer through the interface with ease. This leads to higher thermal conductivities for superlattices with short period lengths. These new vibrational modes are associated with Si-Ge bonds at the interface. The density of these vibrational modes increases as the number of interfaces increases for superlattices with short period lengths 2.8.

Second, our investigation of conductive heat transfer in polymers through non-bonding and bonding interactions suggests that non-bonding interactions are very important for thermal transport in polymers. Contrary to previous beliefs that introduction of strong covalent bonds between polymer chains should increase heat transfer, studies have reported both enhancement ([78]) and reduction ([195]) in the thermal conductivities of polymers upon crosslinking (i.e., formation of strong covalent bonds between chains). We observe that heat transfer along the covalent bonds of the crosslinkers between polymer chains is not the primary inter-chain heat transfer mechanism in crosslinked polymers. We observe that if the crosslinker agent has a short enough length to bring the polymer chains close to each other, non-bonding interactions between the chains are significantly enhanced. The large number of

enhanced inter-chain non-bonding interactions, leads to a significant contribution to inter-chain thermal conductance. This is reasonable, since the number of non-bonding interactions in the system is significantly higher than the number of covalent bonds. For example, an order of magnitude enhancement in thermal conductivity of polymers is observed upon formation of hydrogen bonds between the polymer chains ([81]).

Furthermore, in order to study the impact of non-bonding interactions on heat transfer in crosslinked polymers, we study wave propagation in polymer chains, in the presence and absence of non-bonding interactions. Our results show that acoustic waves travel at significantly faster speeds when non-bonding interactions are included compared to when non-bonding interactions are excluded, due to the long-range nature of non-bonding interactions. Additionally, we show that the introduction of ionic bonds between polymer chains can increase their thermal conductivity by a factor of about two. This is due to enhanced inter-chain bonding, an increase in the radius of gyration of the chains, and increased density. Previous experiments have also have shown enhancements in thermal conductivity of ionically bonded polymers [152].

Finally, machine learning algorithms were developed for fast discovery of materials. We have encoded physical rules in the algorithms such that the algorithms cannot explore function spaces where physical rules are broken. The addition of physical rules to the network allows us to train the algorithms with a smaller dataset (since part of the function space is eliminated by the physical rules already encoded in the algorithm). The algorithms in our work are used for prediction of thermal properties such as total thermal conductivity and frequency-dependent thermal conductivity. After training the networks, it only takes seconds to predict the thermal properties of an unknown material using this algorithm. The development of this method could lead to fast discovery of unprecedented materials.

Similar machine learning algorithms based on our work could be used to extend the applicability of this method towards predicting third-order force constants between

atoms, bridging the gap between nano-scale and macro-scale materials properties, heat diffusivity, and more.

5.2 Future Work

We suggest using the results of this dissertation to develop experiments that could further elucidate the effects of crosslinkers on thermal transport in polymers. For example, experiments could be designed to measure thermal conductivity of a polymer crosslinked with various crosslinkers in order to show the impact of crosslinker length. We also suggest an experiment on other hetero-structures, where the two materials in the structure have a significant difference in their phonon spectra. After these two dissimilar materials form interfaces, we could study the impact of interface bonds on heat transfer in this structure as the period length decreases. This could be used as a means to control thermal conductivity of superlattice structures used in applications such as thermoelectrics.

Additionally, there is a lot of room for using machine learning algorithms for materials discovery. One of these areas is using computer vision algorithms for extraction of non-trivial features from graphical databases. This would streamline the materials discovery process even more than the algorithms that were developed in this thesis. In order to show this application in a nutshell, we have provided the dispersion curve images for the materials studied in this chapter in Appendix B. Machine learning algorithms such as auto-encoders and convolutional neural networks could be used to learn the relationships between these images and the material thermal properties. Our preliminary results show that computer vision algorithms are capable of learning simple relations between thermal conductivity and the shape of dispersion curves. For instance, the algorithms recognize that a higher slope for the acoustic bands of the phonons dispersion curve may indicate a higher thermal conductivity. In the future, more complicated algorithms may reveal complicated relationships between features

of dispersion curves and thermal conductivity. For example, the possible relationship between thermal conductivity and the band gap between acoustic and optical phonons could be revealed using this approach.

Another area for future work would be to use the algorithms in this thesis in order to predict the thermal conductivities of unprecedented materials from a large material database.

APPENDICES

APPENDIX A

Force Field Parameters and Pseudo Potentials

PMMA (OPLS force field)[72, 74]:

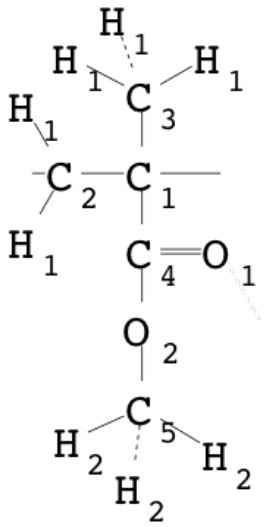

Figure A.1: PMMA monomer structure

Table A.1: Non-bonding Coefficients for Equation 3.2

Atom	q(e.c.)	$\sigma(\mathring{A})$	ϵ (kCal/mol)
C_1	0.00	3.20	0.051
C_2	-0.09	3.52	0.067
C_3	-0.135	3.52	0.067
C_4	0.51	3.75	0.0105
C_5	0.16	3.50	0.066
O_1	-0.43	2.96	0.200
O_2	-0.33	3.00	0.170
H_1	0.045	2.50	0.030
H_2	0.03	2.42	0.0150

Table A.2: Bond Stretch Coefficients for Equation 3.3

Bonds	K_{bond} (kcal/mol/$\mathring{A}$2)	$r_{ij}^0(\mathring{A})$
$C_1 - C_3$	368	1.539
$C_1 - C_2$	300	1.5491
$C_1 - C_4$	326	1.517
$O_1 - C_4$	968	1.209
$O_2 - C_4$	471	1.360
$C_{2(3,5)} - H_{1(2)}$	331	1.09
$O_2 - C_5$	342	1.446

Table A.3: Bond Bend Coefficients for Equation 3.4

Bends	$K_{bending}$ (kcal/mol/rad^2)	$\theta^0_{ij}(rad)$
$C_1 - C_2 - C_1$	89.5	113.3
$C_{2(3)} - C - C_{2(3)}$	87.9	109.47
$C_{2(3)} - C_1 - C_4$	87.9	109.47
$C_1 - C_4 - O_2$	74.5	111.4
$C_1 - C_4 - O_1$	63.3	125.6
$O_1 - C_4 - O_2$	126.5	123.0
$C_4 - O_2 - C_5$	84.8	116.4
$H_1 - C_{2(3)} - C_1$	35.0	109.5
$H_1 - C_{2(3)} - H_1$	35.0	109.5
$H_2 - C_5 - H_2$	35.0	109.5
$H_2 - C_5 - O_2$	56.0	110.1

Table A.4: Torsion Coefficients, for Equation 3.5

Torsion	K_1	K_2	K_3	K_4
$C_{2(3)} - C_1 - C_2 - C_1$	0.27792	0.000	0.000	-0.27792
$C_4 - C_1 - C_2 - C_1$	0.27792	0.000	0.000	-0.27792
$C_{2(3)} - C_1 - C_4 - O_2$	0.80784	0.000	0.000	-0.80784
$C_{2(3)} - C_1 - C_4 - O_1$	2.600	0.050	-2.550	0.000
$C_5 - O_2 - C_4 - C_1$	2.020	-1.000	-0.700	-0.320

PVA [112]:

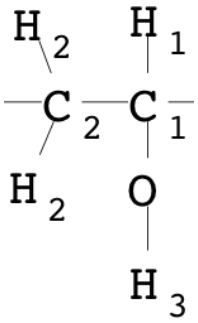

Figure A.2: PVA monomer structure

Table A.5: Non-bonding Coefficients for Equation 3.2

Atom	q(e.c.)	$\sigma(\mathring{A})$	ϵ (kCal/mol)
H_3	0.4	0	0
O	-0.7	3.17	0.155
C_1	0.3	3.5	0.080
C_2	0	3.5	0.080
$H_{1(2)}$	0	2.57	0.05

Table A.6: Bond Stretch Coefficients for Equation 3.3

Bonds	K_{bond} (kcal/mol/$\mathring{A}^2$)	$r_{ij}^0(\mathring{A})$
$H-O$	553	0.97
$C-O$	320	1.431
$C-C$	268	1.53
$C_{1(2)}-H_{1(2)}$	340	1.1

Table A.7: Bond Bend Coefficients for Equation 3.4

Bends	$K_{bending}$ (kcal/mol/rad^2)	$\theta^0_{ij}(rad)$
$H-O-C$	76.6	105
$C-C-C$	115.4	109.45
$O-C-C$	110	107.8
$O-C-H$	83.7	108
$C-C-H$	87.8	110
$H-C-H$	73.2	108

Table A.8: Torsion Coefficients

Torsion	K (kCal/mol)	ϕ_0(degrees)
$H-O-C-C$	1.4354	180
$C-C-C-C$	2.7512	180
$C-C-C-H$	2.7512	180

PE [56]:

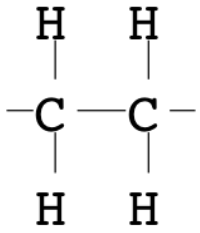

Figure A.3: PE monomer structure

Table A.9: Non-bonding Coefficients for Equation 3.2

Atom	q(e.c.)	$\sigma(\AA)$	ϵ (kCal/mol)
H	0.02742	2.5	0.03
C	-0.05484	3.52	0.067

Table A.10: Bond Stretch Coefficients for Equation 3.3

Bonds	K_{bond} (kcal/mol/$\mathring{A}^2$)	$r_{ij}^0(\mathring{A})$
C-H	350	1.09
C-C	350	1.53

Table A.11: Bond Bend Coefficients for Equation 3.4

Bends	$K_{bending}$ (kcal/mol/rad^2)	$\theta_{ij}^0(rad)$
$C(H)-C-C(X)$	50	109.471

Table A.12: Torsion Coefficients

Torsion	K (kCal/mol)	d	n
$C(H)-C-C-C(H)$	0.111111	1	3

The following pseudo-potentials were used from http://www.quantum-espresso.org. For some of the materials multiple pseudo-potentials were used for comparison, however only one was used for final calculations:

Al.pw-mt_fhi.upf, Al.pz-hgh.upf, As.pw-mt_fhi.upf, As.pz-bhs.upf, As.pz-hgh.upf, B.pw-mt_fhi.upf, B.pz-bhs.upf, B.pz-hgh.upf, Ba.pw-mt_fhi.upf, Be.pw-mt_fhi.upf, Be.pz-hgh.UPF, Bi.pw-mt_fhi.upf, Bi.pz-hgh.upf, Br.pw-mt_fhi.upf, Br.pz-hgh.upf, C.pw-mt_fhi.upf, C.pz-hgh.upf, C.pz-kjpaw.upf, Ca.pw-mt_fhi.upf, Ca.pz-hgh.UPF, Cd.pw-mt_fhi.upf, Cl.pw-mt_fhi.upf, Cs.pw-mt_fhi.upf, F.pw-mt_fhi.upf, Ga.pw-d-mt_fhi.upf, Ga.pw-mt_fhi.upf, Ga.pz-bhs.upf, Ge.pw-mt_fhi.upf, Ge.pz-bhs.upf, I.pw-mt_fhi.upf, I.rel-pz-n-kjpaw_psl.0.2.2.UPF, In.pw-d-mt_fhi.upf, In.pw-mt_fhi.upf, In.pz-bhs.upf, K.pw-mt_fhi.upf, K.pz-hgh.UPF, Li.pw-mt_fhi.upf, Li.pz-hgh.UPF, Mg.pw-mt_fhi.upf, Mg.pz-bhs.UPF, Mg.pz-hgh.UPF, N.pw-mt_fhi.upf, N.pz-hgh.upf, Na.pw-mt_fhi.upf, Na.pz-hgh.UPF, O.pw-mt_fhi.upf, O.pz-hgh.upf, O.pz-kjpaw.upf, P.pw-mt_fhi.upf, P.pz-

bhs.upf, Pb.pw-mt_fhi.upf, Rb.pw-mt_fhi.upf, S.pw-mt_fhi.upf, S.pz-bhs.upf, Sb.pw-mt_fhi.upf, Sb.pz-bhs.upf, Sb.pz-hgh.upf, Se.pw-mt_fhi.upf, Se.pz-bhs.upf, Se.pz-hgh.upf, Si.pw-mt_fhi.upf, Si.pz-hgh.upf, Sn.pw-mt_fhi.upf, Sn.pz-bhs.upf, Te.pw-mt_fhi.upf, Ti.pw-mt_fhi.upf, Zn.pw-mt_fhi.upf

APPENDIX B

Some of Training Data for Machine Learning

Table B.1: Properties of some of the materials used in this thesis. GN = Group Number, PN = Period Number in Periodic Table. Here We Study Systems with Two Atoms in Their Unit Cell. 1st and 2nd Refer to Those Atoms.

Material	Mass	Lattice Const.(nm)	GN 1st	GN 2nd	PN 1st	PN 2nd	Density (kg/m^3)
AlAs	101.9031	0.56191	13	15	3	4	3720
AlN	40.9882	0.43009	13	15	3	2	3260
AlP	57.9553	0.54094	13	15	3	3	2850
AlSb	148.7415	0.60738	13	15	3	5	4260
BAs	85.7326	0.47311	13	15	2	4	5220
BP	41.7848	0.44783	13	15	2	3	3450
CdS	144.476	0.5815	12	16	5	3	4820
CdSe	191.371	0.60643	12	16	5	3	5820
CdTe	240.011	0.6421	12	16	5	5	6200
GaAs	144.6446	0.55336	13	15	4	4	5320
GaN	83.7297	0.43087	13	15	4	2	6150
GaP	100.6968	0.5316	13	15	4	3	4138
GaSb	191.483	0.59596	13	15	4	5	5610
Ge	145.28	0.55697	14	14	4	4	5323
InSb	236.578	0.62961	13	15	5	5	5780
Si	56.171	0.53805	14	14	3	3	2329
SiC	40.0962	0.43068	14	14	3	2	3210
SiGe	100.7255	0.54663	14	14	3	4	3826
ZnS	97.455	0.53252	12	16	4	3	4090

Dispersion curve images for the materials in diamond crystal structure. All dispersion curves are color coded such that the shade of the lines corresponds to the occupation of the modes at that frequency based on Bose-Einstein distribution. The vertical axes shows the phonon frequencies. All curves are scaled such that the minimum frequency is 0 Hz and the maximum frequency is 44 THz. The horizontal axes shows the wave numbers for the phonons.

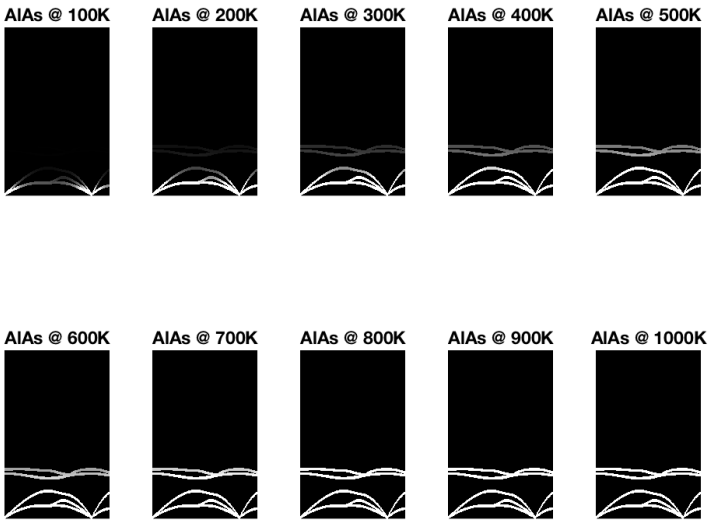

Figure B.1: Dispersion curve for AlAs

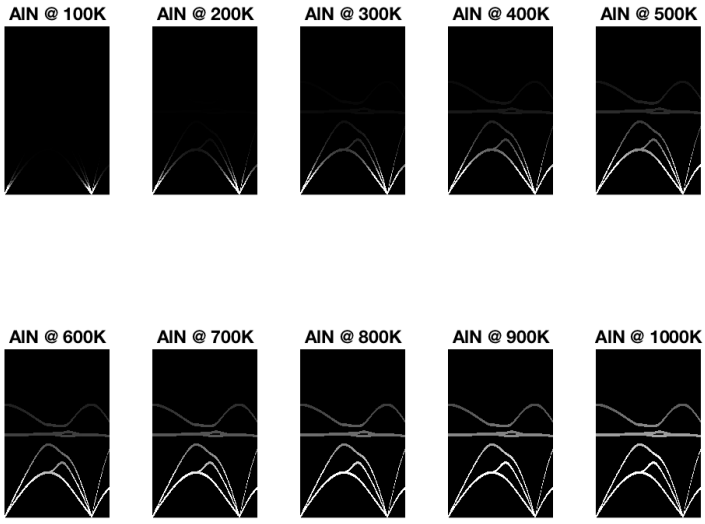

Figure B.2: Dispersion curve for AlN

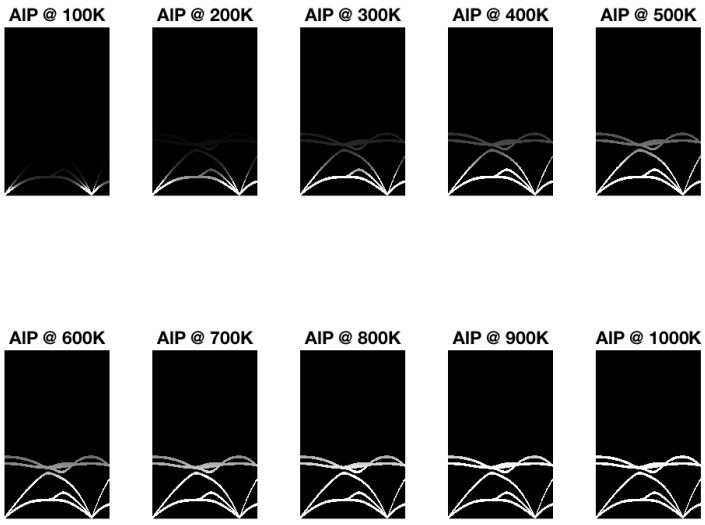

Figure B.3: Dispersion curve for AlP

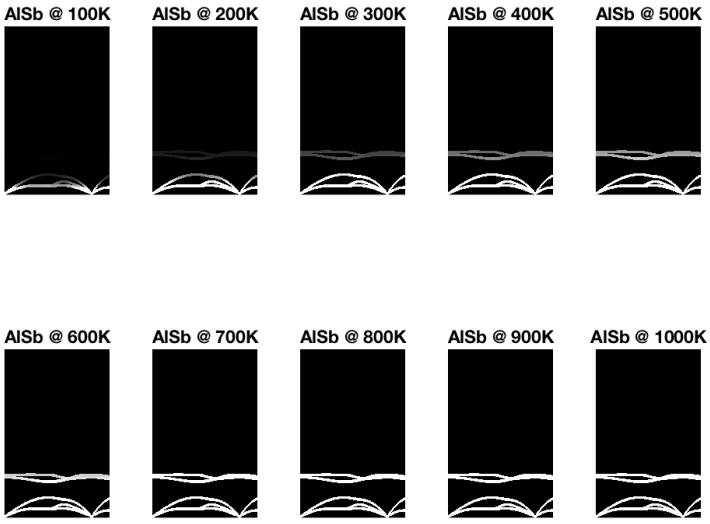

Figure B.4: Dispersion curve for AlSb

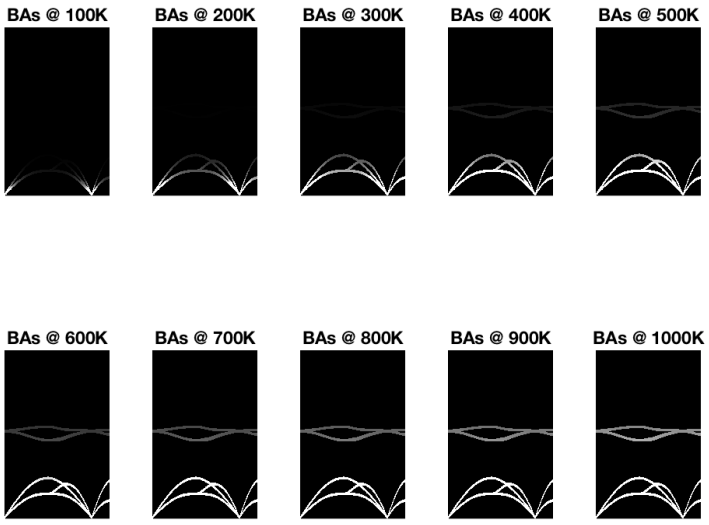

Figure B.5: Dispersion curve for BAs

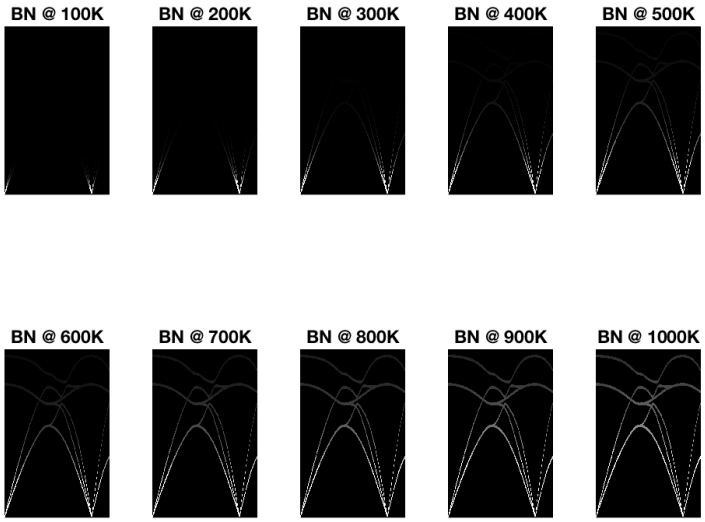

Figure B.6: Dispersion curve for BN

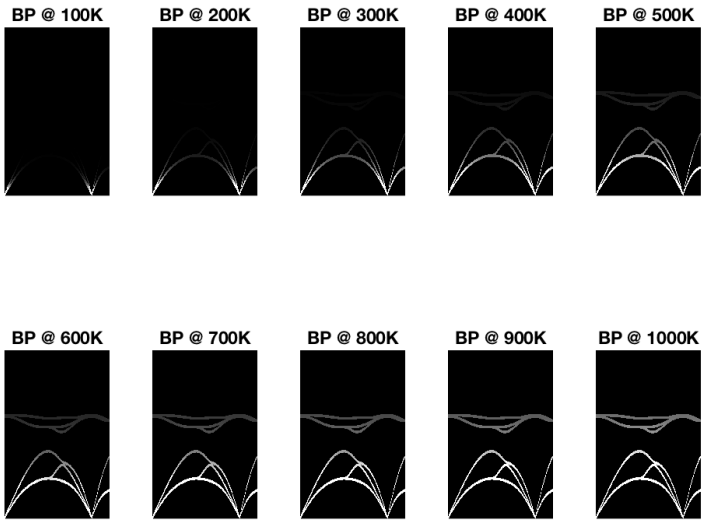

Figure B.7: Dispersion curve for BP

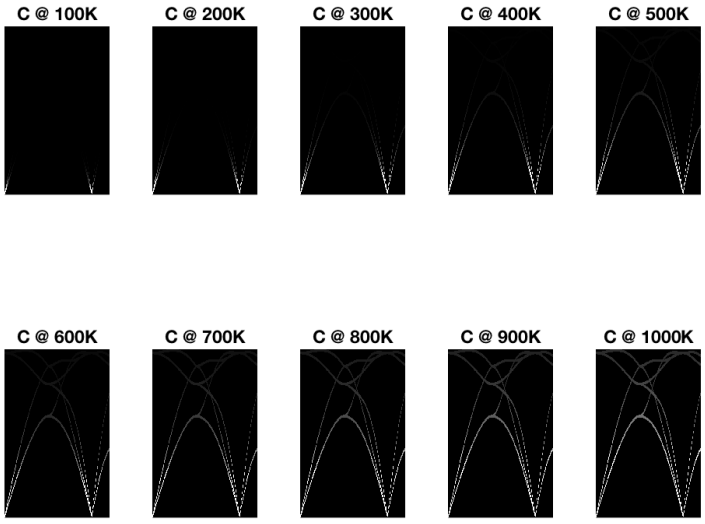

Figure B.8: Dispersion curve for diamond (carbon)

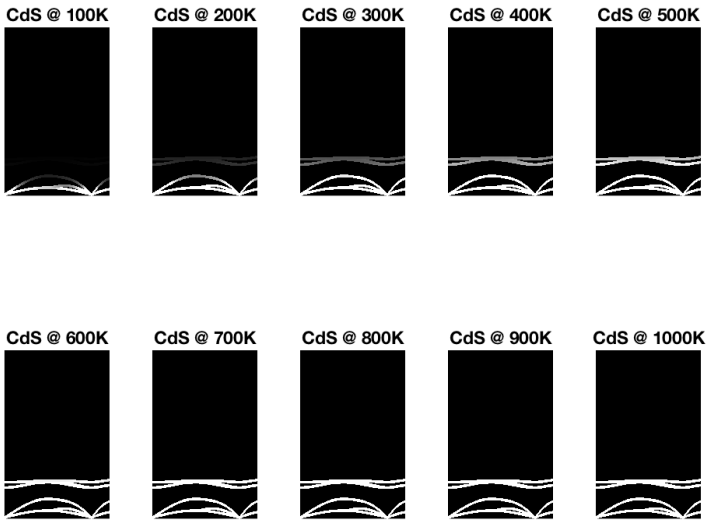

Figure B.9: Dispersion curve for CdS

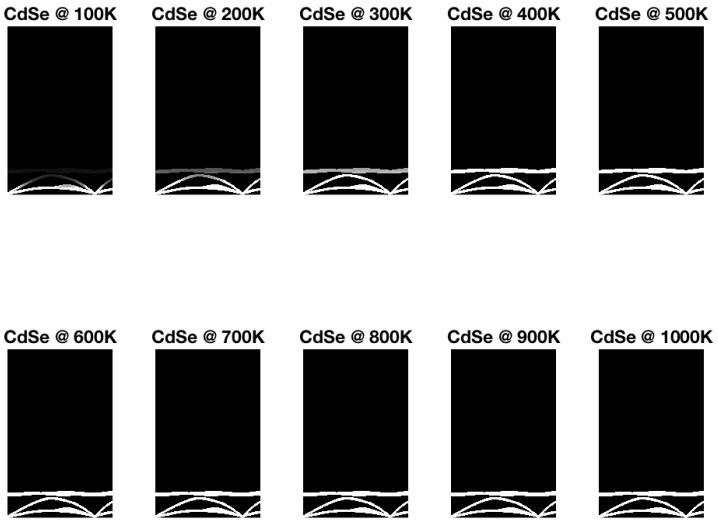

Figure B.10: Dispersion curve for CdSe

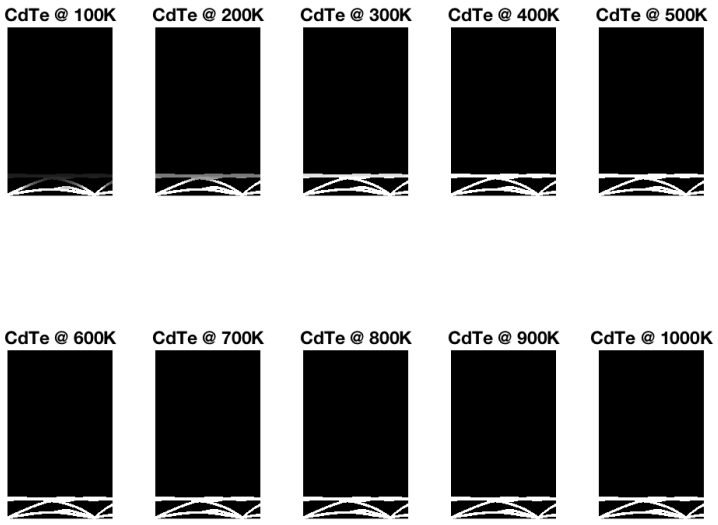

Figure B.11: Dispersion curve for CdTe

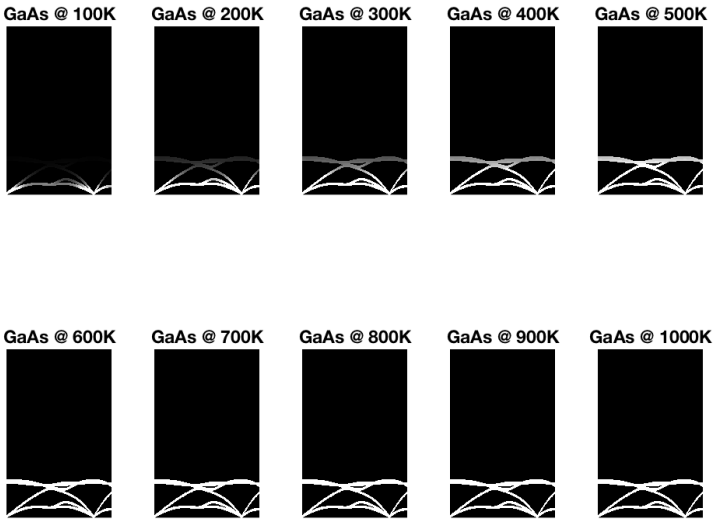

Figure B.12: Dispersion curve for GaAs

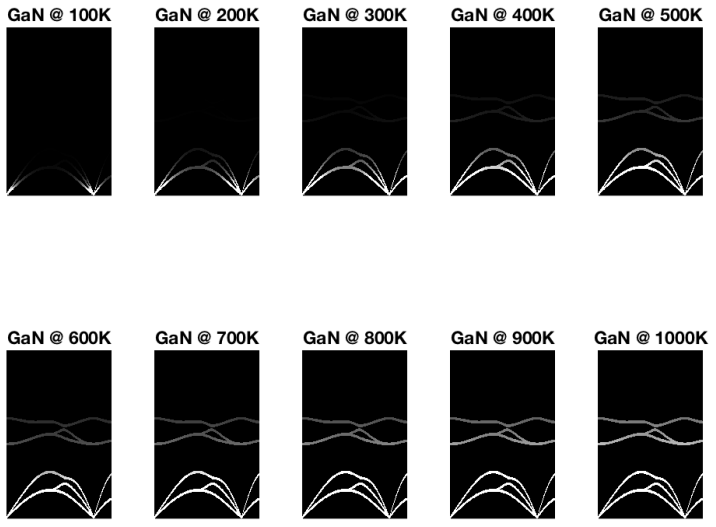

Figure B.13: Dispersion curve for GaN

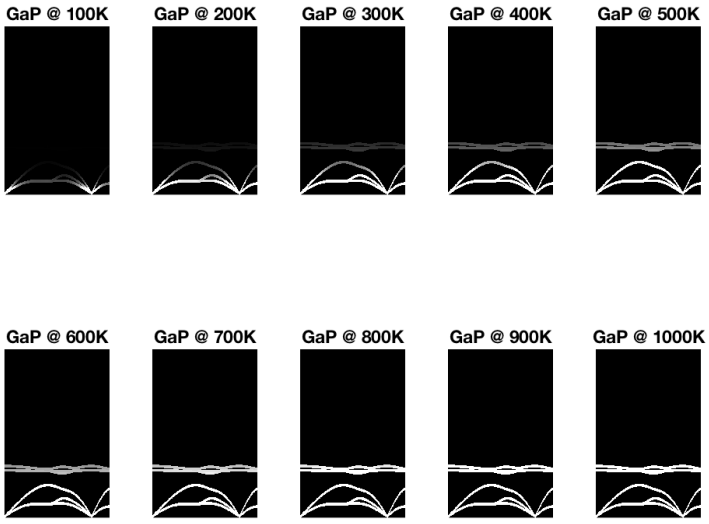

Figure B.14: Dispersion curve for GaP

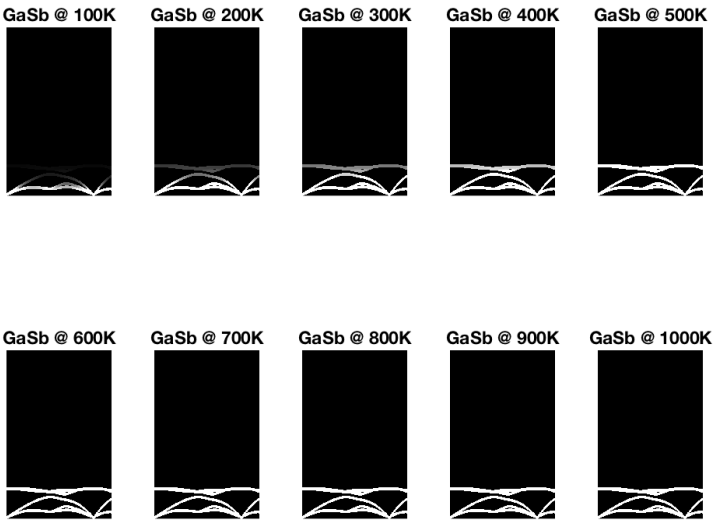

Figure B.15: Dispersion curve for GaSb

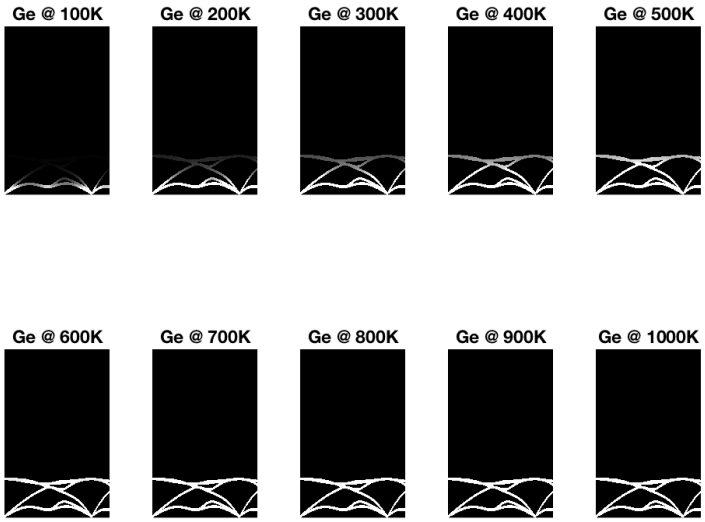

Figure B.16: Dispersion curve for germanium

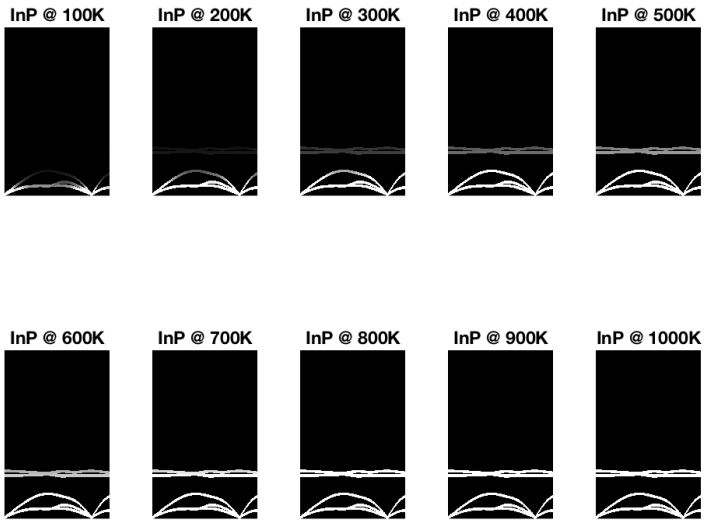

Figure B.17: Dispersion curve for InP

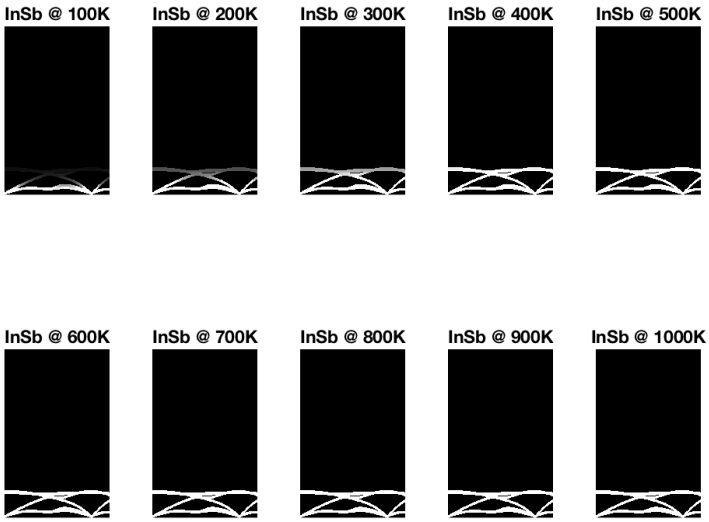

Figure B.18: Dispersion curve for InSb

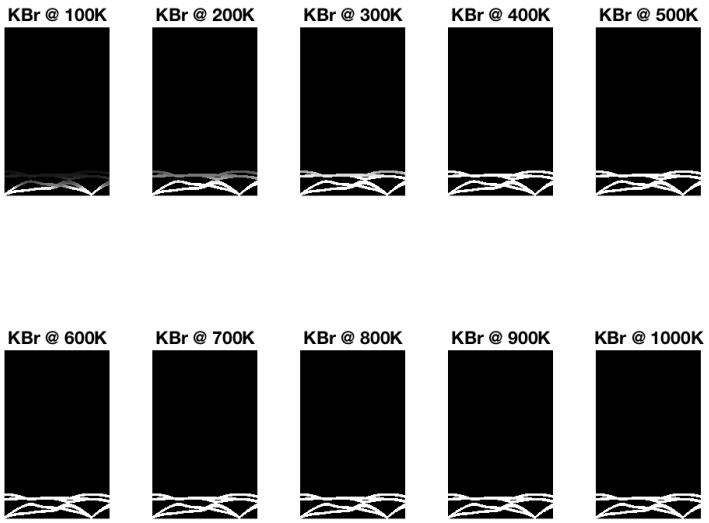

Figure B.19: Dispersion curve for KBr

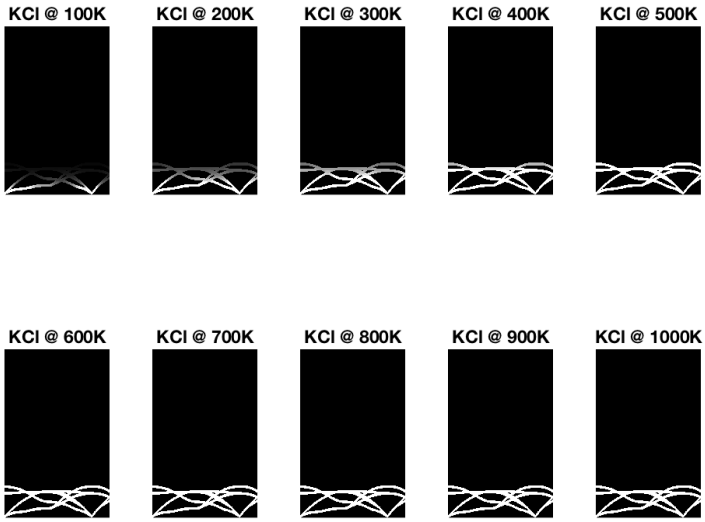

Figure B.20: Dispersion curve for KCl

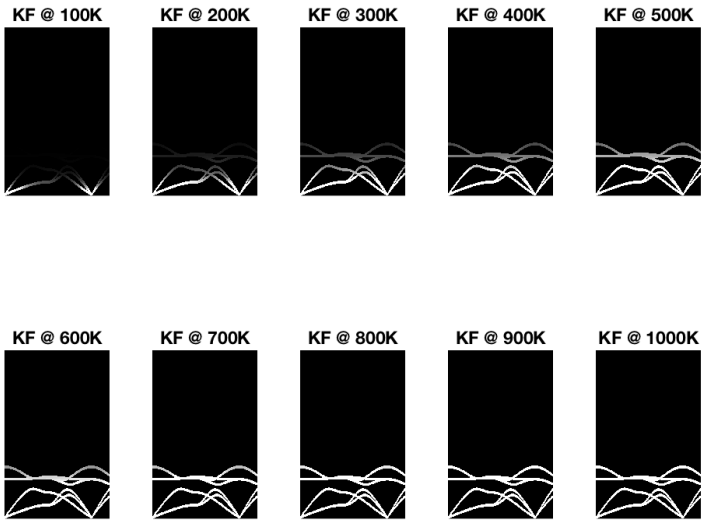

Figure B.21: Dispersion curve for KF

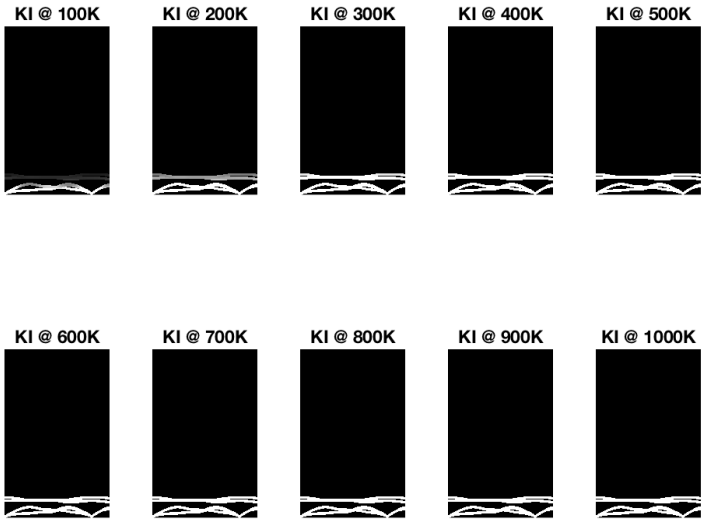

Figure B.22: Dispersion curve for KI

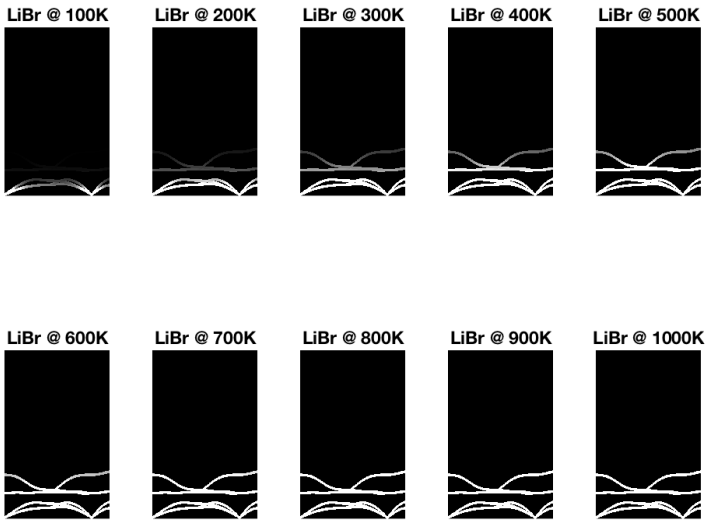

Figure B.23: Dispersion curve for LiBr

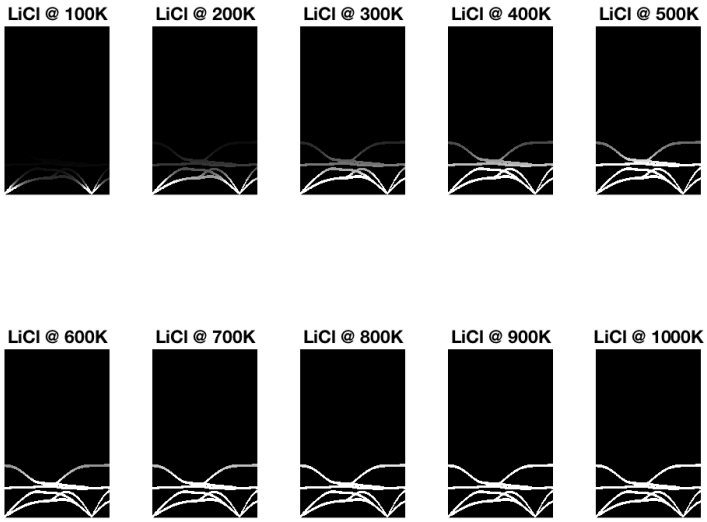

Figure B.24: Dispersion curve for LiCl

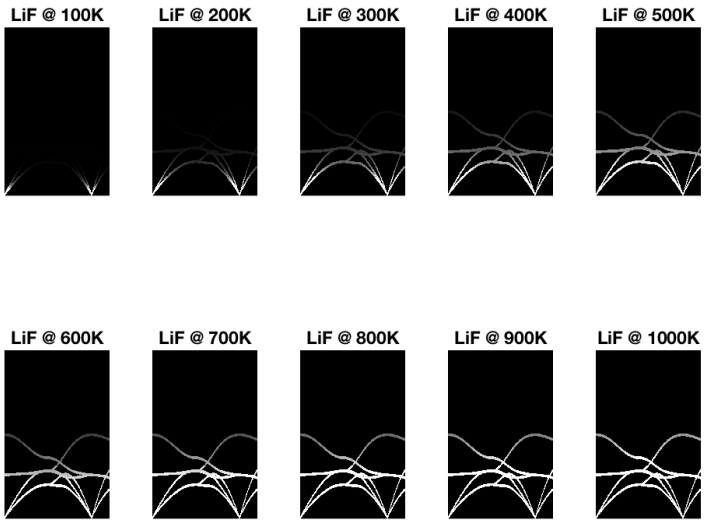

Figure B.25: Dispersion curve for LiF

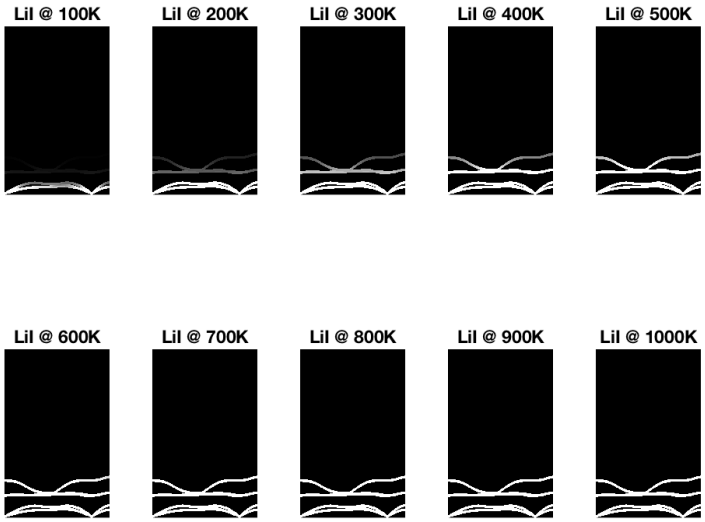

Figure B.26: Dispersion curve for LiI

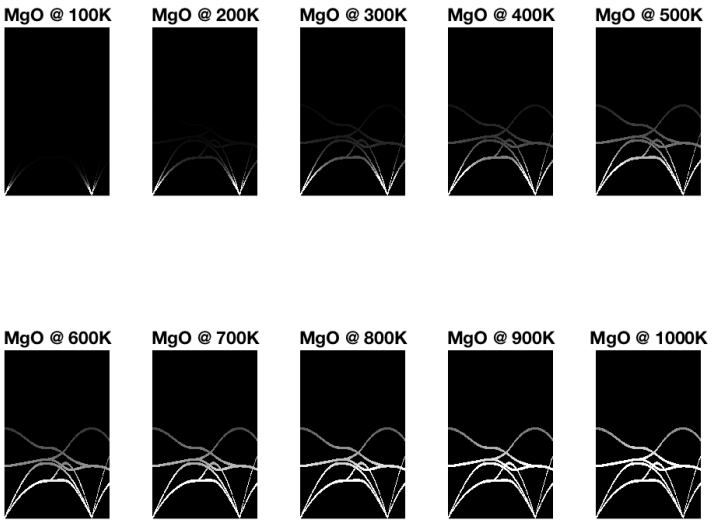

Figure B.27: Dispersion curve for MgO

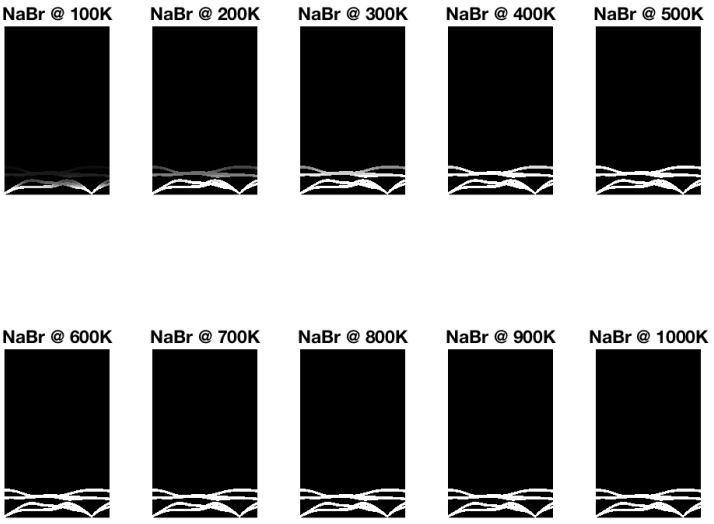

Figure B.28: Dispersion curve for NaBr

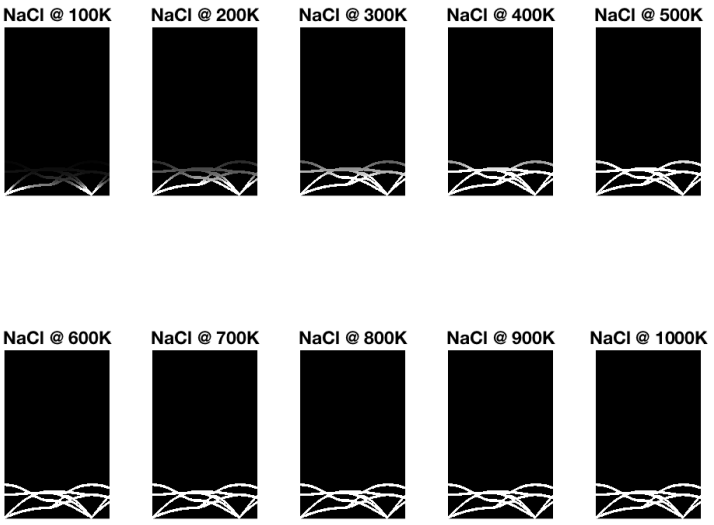

Figure B.29: Dispersion curve for NaCl

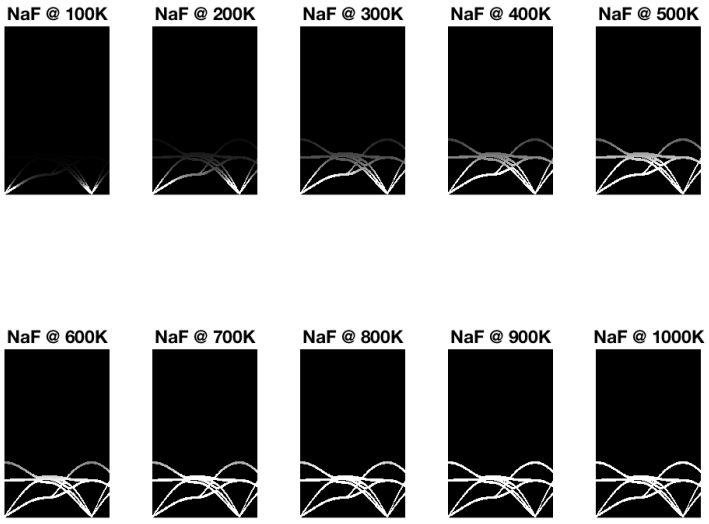

Figure B.30: Dispersion curve for NaF

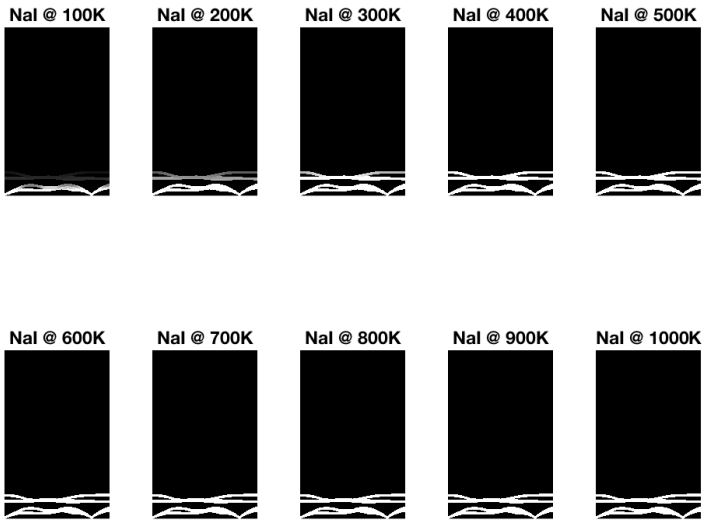

Figure B.31: Dispersion curve for NaI

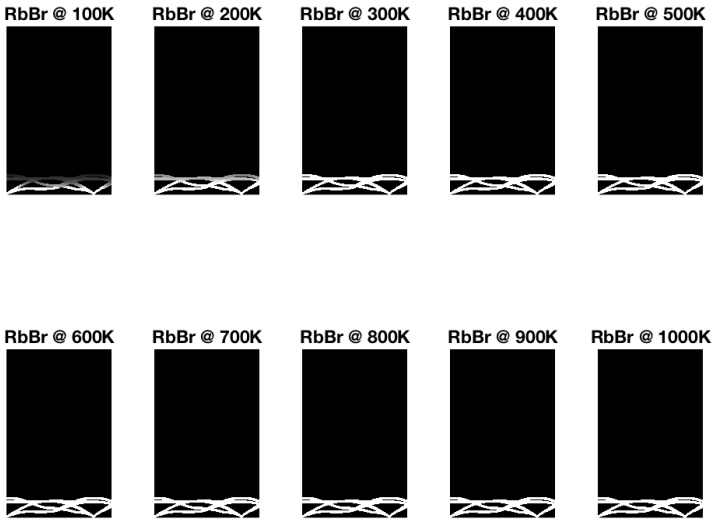

Figure B.32: Dispersion curve for RbBr

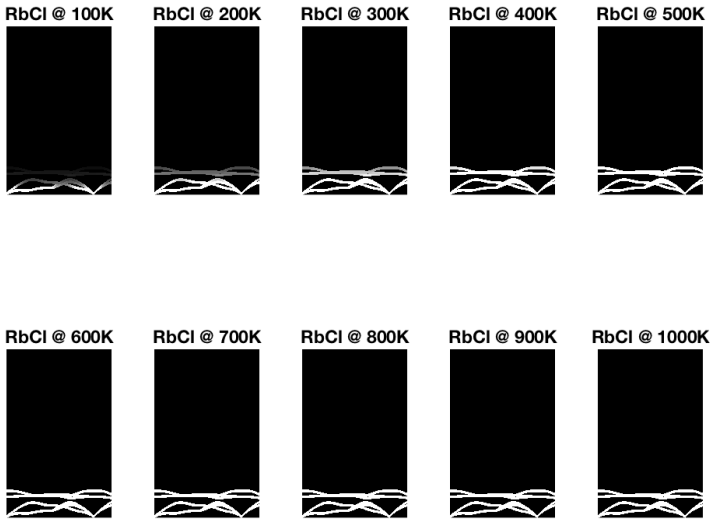

Figure B.33: Dispersion curve for RbCl

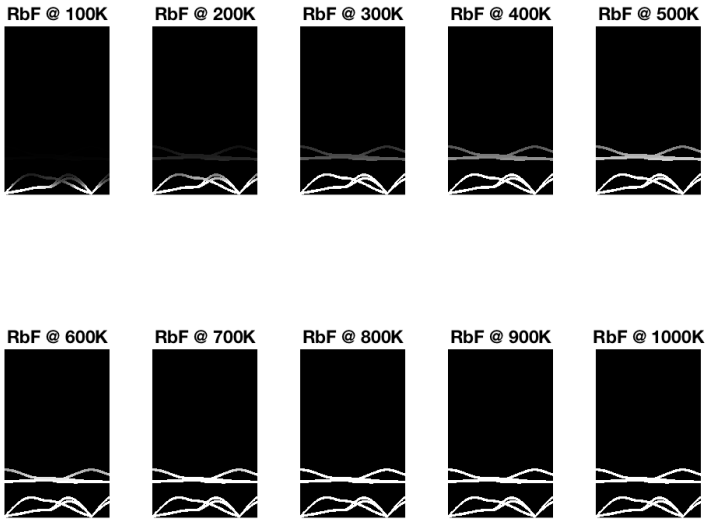

Figure B.34: Dispersion curve for RbF

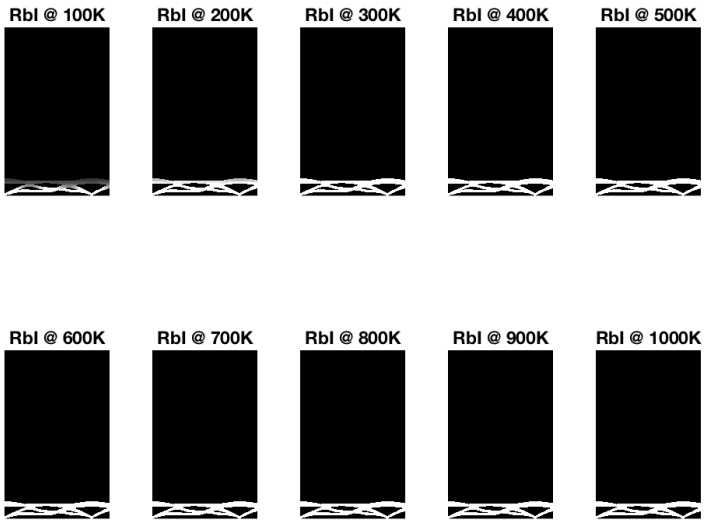

Figure B.35: Dispersion curve for RbI

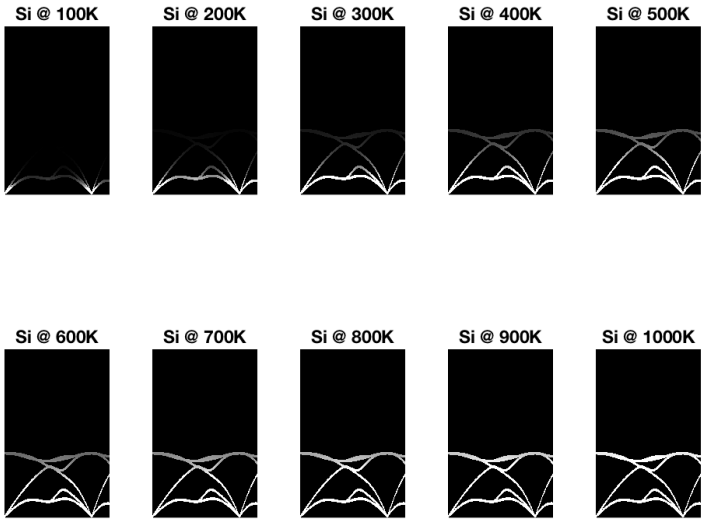

Figure B.36: Dispersion curve for silicon

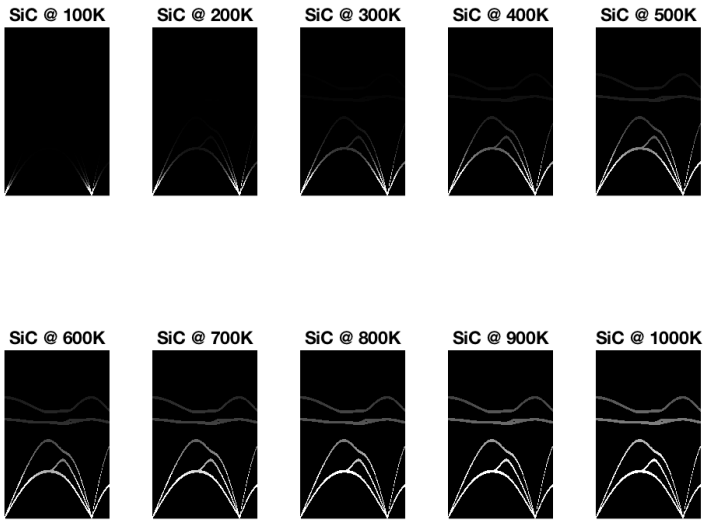

Figure B.37: Dispersion curve for SiC

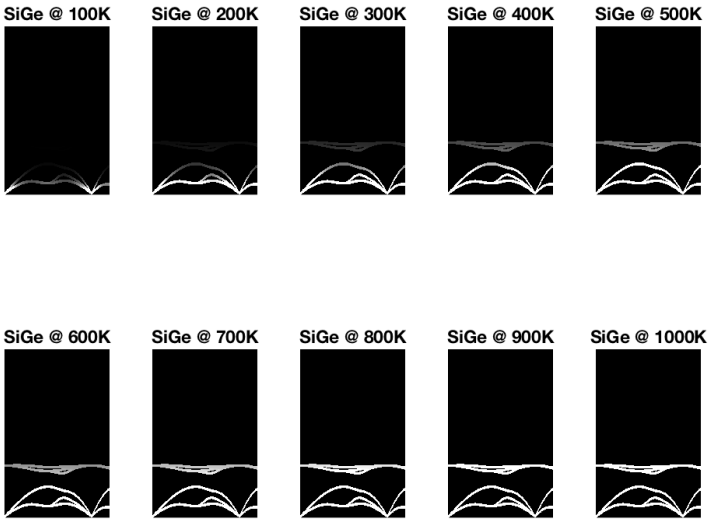

Figure B.38: Dispersion curve for SiGe

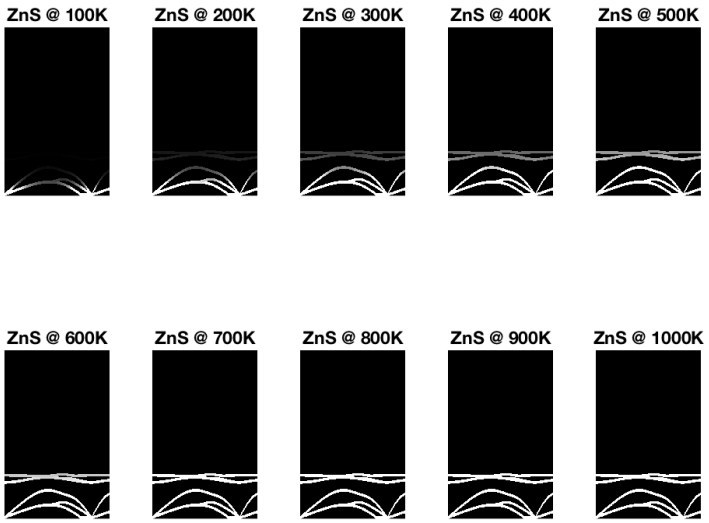

Figure B.39: Dispersion curve for ZnS

BIBLIOGRAPHY

BIBLIOGRAPHY

[1] Persistence of vision pty. ltd. (2004). persistence of vision (tm) ray-tracer. persistence of vision pty. ltd., williamstown, victoria, australia. *http://www.povray.org/*.

[2] Hari Acharya, Nicholas J. Mozdzierz, Pawel Keblinski, and Shekhar Garde. How chemistry, nanoscale roughness, and the direction of heat flow affect thermal conductance of solid–water interfaces. *Ind. Eng Chem. Res.*, 51(4):1767–1773, 2012.

[3] Charu C. Aggarwal. *Data Mining*. Springer International Publishing, 1 edition, 2015.

[4] Cheol Hyoun Ahn, Karuppanan Senthil, Hyung Koun Cho, and Sang Yeol Lee. Artificial semiconductor/insulator superlattice channel structure for high-performance oxide thin-film transistors. *Scientific Reports*, 3:2737 EP –, 09 2013.

[5] M. F. A. Alias, N. N. Rammo, and M. N. Makadsi. Lattice parameter and density of ge–si solid solutions. *RENEWABLE ENERGY*, 24:347–351, 2001.

[6] Kah-Wee Ang, Hock-Chun Chin, King-Jien Chui, Ming-Fu Li, Ganesh S. Samudra, and Yee-Chia Yeo. Carrier backscattering characteristics of strained silicon-on-insulator n-mosfets featuring silicon–carbon source/drain regions. *Solid-State Electronics*, 51(11):1444 – 1449, 2007. Special Issue: Papers Selected from the 36th European Solid-State Device Research Conference - ESSDERC'06.

[7] Henry Asegun. Thermal transport in polymers. *Ann. Rev. Heat Transfer*, 17(Chapter 13):485–520, 2014.

[8] Kosata B. bkchem, 2009.

[9] Akbar Bagri, Sang-Pil Kim, Rodney S. Ruoff, and Vivek B. Shenoy. Thermal transport across twin grain boundaries in polycrystalline graphene from nonequilibrium molecular dynamics simulations. *Nano Lett.*, 11(9):3917–3921, 2011. PMID: 21863804.

[10] Zachary S. Ballard, Daniel Shir, Aashish Bhardwaj, Sarah Bazargan, Shyama Sathianathan, and Aydogan Ozcan. Computational sensing using low-cost and mobile plasmonic readers designed by machine learning. *ACS Nano*, 11(2):2266–2274, 2017. PMID: 28128933.

[11] S W Bedell, K Fogel, D K Sadana, and H Chen. Defects and strain relaxation in silicon-germanium-on-insulator formed by defects and strain relaxation in silicon-germanium-on-insulator formed by high-temperature oxidation. *APPLIED PHYSICS LETTERS*, 85(24), 2004.

[12] V. Botu, R. Batra, J. Chapman, and R. Ramprasad. Machine learning force fields: Construction, validation, and outlook. *The Journal of Physical Chemistry C*, 121(1):511–522, 2017.

[13] Olga Bubnova, Zia Ullah Khan, Abdellah Malti, Slawomir Braun, Mats Fahlman, Magnus Berggren, and Xavier Crispin. Optimization of the thermoelectric figure of merit in the conducting polymer poly(3,4-ethylenedioxythiophene). *Nat. Mater.*, 10(6):429–433, 06 2011.

[14] David G. Cahill. Thermal conductivity measurement from 30 to 750 k: the 3 method. *Review of Scientific Instruments*, 61(2):802–808, 1990.

[15] David G. Cahill, Wayne K. Ford, Kenneth E. Goodson, Gerald D. Mahan, Arun Majumdar, Humphrey J. Maris, Roberto Merlin, and Simon R. Phillpot. Nanoscale thermal transport. *Journal of Applied Physics*, 93(2):793–818, 2003.

[16] Carlo Canetta, Samuel Guo, and Arvind Narayanaswamy. Measuring thermal conductivity of polystyrene nanowires using the dual-cantilever technique. *Rev. Sci. Instrum.*, 85(10):104901, 2014.

[17] Bing-Yang Cao, Yuan-Wei Li, Jie Kong, Heng Chen, Yan Xu, Kai-Leung Yung, and An Cai. High thermal conductivity of polyethylene nanowire arrays fabricated by an improved nanoporous template wetting technique. *Polymer*, 52(8):1711–1715, 2011.

[18] F. Capasso, A. Tredicucci, C. Gmachl, D. L. Sivco, A. L. Hutchinson, A. Y. Cho, and G. Scamarcio. High-performance superlattice quantum cascade lasers. *IEEE Journal of Selected Topics in Quantum Electronics*, 5(3):792–807, 1999.

[19] William S. Capinski and Humphrey J. Maris. Improved apparatus for picosecond pumpandprobe optical measurements. *Review of Scientific Instruments*, 67(8):2720–2726, 1996.

[20] Juan Carrasquilla and Roger G. Melko. Machine learning phases of matter. *Nat Phys*, 13(5):431–434, 05 2017.

[21] Jesús Carrete, Wu Li, Natalio Mingo, Shidong Wang, and Stefano Curtarolo. Finding unprecedentedly low-thermal-conductivity half-heusler semiconductors via high-throughput materials modeling. *Phys. Rev. X*, 4:011019, Feb 2014.

[22] Y Chalopin, K Esfarjani, A Henry, S Volz, and G Chen. Thermal interface conductance in si/ge superlattices by equilibrium molecular dynamics. *PHYSICAL REVIEW B*, 85(195302), 2012.

[23] Chunxia Chen, Janna K. Maranas, and Victoria García-Sakai. Local dynamics of syndiotactic poly(methyl methacrylate) using molecular dynamics simulation. *Macromolecules*, 39(26):9630–9640, 2006.

[24] Xiangxu Chen, Matheus A. Dam, Kanji Ono, Ajit Mal, Hongbin Shen, Steven R. Nutt, Kevin Sheran, and Fred Wudl. A thermally re-mendable cross-linked polymeric material. *Science*, 295(5560):1698–1702, 2002.

[25] Xiaoling Chen, Antonio Munjiza, Kai Zhang, and Dongsheng Wen. Molecular dynamics simulation of heat transfer from a gold nanoparticle to a water pool. *J. Phys. Chem. C*, 118(2):1285–1293, 2014.

[26] Yunfei Chen, Deyu Li, Jennifer R. Lukes, Zhonghua Ni, and Minhua Chen. Minimum superlattice thermal conductivity from molecular dynamics. *Phys. Rev. B*, 72:174302, Nov 2005.

[27] Eliodoro Chiavazzo and Pietro Asinari. Enhancing surface heat transfer by carbon nanofins: Towards an alternative to nanofluids? *Nanoscale Res. Lett.*, 6(1):1–13, 2011.

[28] Kamesh Chilukuri, Michael J Mori, Carl L Dohrman, and Eugene A Fitzgerald. Monolithic cmos-compatible algainp visible led arrays on silicon on lattice-engineered substrates (soles). *Semiconductor Science and Technology*, 22(2):29, 2007.

[29] C. L. Choy, S. P. Wong, and K. Young. Model calculation of the thermal conductivity of polymer crystals. *J. Polym. Sci. Pol. Phys.*, 23(8):1495–1504, 1985.

[30] C. L. Choy, Y. W. Wong, G. W. Yang, and Tetsuo Kanamoto. Elastic modulus and thermal conductivity of ultradrawn polyethylene. *J. Polym. Sci. Pol. Phys.*, 37(23):3359–3367, 1999.

[31] Steven W. Cranford and Markus J. Buehler. Variation of weak polyelectrolyte persistence length through an electrostatic contour length. *Macromolecules*, 45(19):8067–8082, 2012.

[32] E. D. Cubuk, S. S. Schoenholz, J. M. Rieser, B. D. Malone, J. Rottler, D. J. Durian, E. Kaxiras, and A. J. Liu. Identifying structural flow defects in disordered solids using machine-learning methods. *Phys. Rev. Lett.*, 114:108001, Mar 2015.

[33] Mario Culebras, Clara M. Gómez, and Andrés Cantarero. Review on polymers for thermoelectric applications. *Materials*, 7(9):6701–6732, 2014.

[34] Stefano Curtarolo, Gus L. W. Hart, Marco Buongiorno Nardelli, Natalio Mingo, Stefano Sanvito, and Ohad Levy. The high-throughput highway to computational materials design. *Nat Mater*, 12(3):191–201, 03 2013.

[35] Smita Dayal, Nikos Kopidakis, Dana C. Olson, David S. Ginley, and Garry Rumbles. Photovoltaic devices with a low band gap polymer and cdse nanostructures exceeding 3% efficiency. *Nano Lett.*, 10(1):239–242, 2010. PMID: 20000623.

[36] Volker L. Deringer and Gábor Csányi. Machine learning based interatomic potential for amorphous carbon. *Phys. Rev. B*, 95:094203, Mar 2017.

[37] Zhiwei Ding, Qing-Xiang Pei, Jin-Wu Jiang, and Yong-Wei Zhang. Manipulating the thermal conductivity of monolayer mos2 via lattice defect and strain engineering. *J. Phys. Chem. C*, 119(28):16358–16365, 2015.

[38] K. Eiermann. Modellmäßige deutung der wärmeleitfähigkeit von hochpolymeren. *Colloid. Polym. Sci. (Kolloid-Zeitschrift und Zeitschrift für Polymere)*, 198(1-2):5–16, 1964.

[39] Timothy S. English, John C. Duda, Justin L. Smoyer, Donald A. Jordan, Pamela M. Norris, and Leonid V. Zhigilei. Enhancing and tuning phonon transport at vibrationally mismatched solid-solid interfaces. *Phys. Rev. B*, 85:035438, Jan 2012.

[40] J. J. Freeman, G. J. Morgan, and C. A. Cullen. Thermal conductivity of a single polymer chain. *Phys. Rev. B*, 35:7627–7635, May 1987.

[41] Hiroyuki Fujishiro, Manabu Ikebe, Toshihiro Kashima, and Atsuhiko Yamanaka. Drawing effect on thermal properties of high-strength polyethylene fibers. *Jpn. J. Appl. Phys.*, 37(4A):1994–1995, 1998.

[42] Chen Gang. *Nanoscale energy transport and conversion - A parallel treatment of electrons, molecules, phonons, and photons.* Oxford University Press: New York, 2005.

[43] Weimin Gao, Lingxue Kong, and Peter Hodgson. Atomic interaction of functionalized carbon nanotube-based nanofluids with a heating surface and its effect on heat transfer. *Int. J. Heat Mass Tran.*, 55:5007–5015, 2012.

[44] Yuan Gao and Baoxing Xu. Probing thermal conductivity of fullerene c60 hosting a single water molecule. *J. Phys. Chem. C*, 119(35):20466–20473, 2015.

[45] S. V. Garimella, A. S. Fleischer, J. Y. Murthy, A. Keshavarzi, R. Prasher, C. Patel, S. H. Bhavnani, R. Venkatasubramanian, R. Mahajan, Y. Joshi, B. Sammakia, B. A. Myers, L. Chorosinski, M. Baelmans, P. Sathyamurthy, and P. E. Raad. Thermal challenges in next-generation electronic systems. *IEEE Transactions on Components and Packaging Technologies*, 31(4):801–815, Dec 2008.

[46] Haixiong Ge, Wei Wu, Zhiyong Li, Gun-Young Jung, Deirdre Olynick, Yanfeng Chen, J. Alexander Liddle, Shih-Yuan Wang, and R. Stanley Williams. Crosslinked polymer replica of a nanoimprint mold at 30 nm half-pitch. *Nano Lett.*, 5(1):179–182, 2005. PMID: 15792435.

[47] Zoubin Ghahramani. Probabilistic machine learning and artificial intelligence. *Nature*, 521(7553):452–459, 05 2015.

[48] P Giannozzi, O Andreussi, T Brumme, O Bunau, M Buongiorno Nardelli, M Calandra, R Car, C Cavazzoni, D Ceresoli, M Cococcioni, N Colonna, I Carnimeo, A Dal Corso, S de Gironcoli, P Delugas, R A DiStasio Jr, A Ferretti, A Floris, G Fratesi, G Fugallo, R Gebauer, U Gerstmann, F Giustino, T Gorni, J Jia, M Kawamura, H-Y Ko, A Kokalj, E Küçükbenli, M Lazzeri, M Marsili, N Marzari, F Mauri, N L Nguyen, H-V Nguyen, A Otero de-la Roza, L Paulatto, S Poncé, D Rocca, R Sabatini, B Santra, M Schlipf, A P Seitsonen, A Smogunov, I Timrov, T Thonhauser, P Umari, N Vast, X Wu, and S Baroni. Advanced capabilities for materials modelling with q uantum espresso. *Journal of Physics: Condensed Matter*, 29(46):465901, 2017.

[49] Paolo Giannozzi, Stefano Baroni, Nicola Bonini, Matteo Calandra, Roberto Car, Carlo Cavazzoni, Davide Ceresoli, Guido L Chiarotti, Matteo Cococcioni, Ismaila Dabo, Andrea Dal Corso, Stefano de Gironcoli, Stefano Fabris, Guido Fratesi, Ralph Gebauer, Uwe Gerstmann, Christos Gougoussis, Anton Kokalj, Michele Lazzeri, Layla Martin-Samos, Nicola Marzari, Francesco Mauri, Riccardo Mazzarello, Stefano Paolini, Alfredo Pasquarello, Lorenzo Paulatto, Carlo Sbraccia, Sandro Scandolo, Gabriele Sclauzero, Ari P Seitsonen, Alexander Smogunov, Paolo Umari, and Renata M Wentzcovitch. Quantum espresso: a modular and open-source software project for quantum simulations of materials. *Journal of Physics: Condensed Matter*, 21(39):395502 (19pp), 2009.

[50] Rafael Gomez-Bombarelli, Jorge Aguilera-Iparraguirre, Timothy D. Hirzel, David Duvenaud, Dougal Maclaurin, Martin A. Blood-Forsythe, Hyun Sik Chae, Markus Einzinger, Dong-Gwang Ha, Tony Wu, Georgios Markopoulos, Soonok Jeon, Hosuk Kang, Hiroshi Miyazaki, Masaki Numata, Sunghan Kim, Wenliang Huang, Seong Ik Hong, Marc Baldo, Ryan P. Adams, and Alan Aspuru-Guzik. Design of efficient molecular organic light-emitting diodes by a high-throughput virtual screening and experimental approach. *Nat Mater*, 15(10):1120–1127, 10 2016.

[51] Kiarash Gordiz and Asegun Henry. Interface conductance modal analysis of lattice matched ingaas/inp. *Appl. Phys. Lett.*, 108(18):181606, 2016.

[52] Kiarash Gordiz and Asegun Henry. Phonon transport at crystalline si/ge interfaces: The role of interfacial modes of vibration. 6:23139 EP –, 03 2016.

[53] Michael A. Gosselin, Wenjin Guo, and Robert J. Lee. Efficient gene transfer using reversibly cross-linked low molecular weight polyethylenimine. *Bioconjugate Chem.*, 12(6):989–994, 2001. PMID: 11716690.

[54] Brian A. Gregg and Adam Heller. Cross-linked redox gels containing glucose oxidase for amperometric biosensor applications. *Anal. Chem.*, 62(3):258–263, 1990.

[55] Zhi Guo, Doyun Lee, Yi Liu, Fangyuan Sun, Anna Sliwinski, Haifeng Gao, Peter C. Burns, Libai Huang, and Tengfei Luo. Tuning the thermal conductivity of solar cell polymers through side chain engineering. *Phys. Chem. Chem. Phys.*, 16:7764–7771, 2014.

[56] Benjamin P Haley, Nate Wilson, Chunyu Li, Andrea Arguelles, Eugenio Jaramillo, and Alejandro Strachan. Polymer modeler. *https://nanohub.org/resources/polymod*, (DOI: 10.4231/D3JD4PQ7T), 2017.

[57] MarcusD Hanwell, DonaldE Curtis, DavidC Lonie, Tim Vandermeersch, Eva Zurek, and GeoffreyR Hutchison. Avogadro: an advanced semantic chemical editor, visualization, and analysis platform. *J. Cheminform.*, 4(1), 2012.

[58] S. Hashemi and J.G. Williams. A fracture toughness study on low density and linear low density polyethylenes. *Polymer*, 27(3):384–392, 1986.

[59] Guang S. He, Kie-Soo Kim, Lixiang Yuan, Ning Cheng, and Paras N. Prasad. Two-photon pumped partially cross-linked polymer laser. *Appl. Phys. Lett.*, 71(12):1619–1621, 1997.

[60] Asegun Henry and Gang Chen. High thermal conductivity of single polyethylene chains using molecular dynamics simulations. *Phys. Rev. Lett.*, 101:235502, Dec 2008.

[61] J. P. Holman. *Heat Transfer*. Number 1-12. McGraw Hill, 1989.

[62] William G. Hoover. Canonical dynamics: Equilibrium phase-space distributions. *Phys. Rev. A*, 31:1695–1697, Mar 1985.

[63] Kurt Hornik. Approximation capabilities of multilayer feedforward networks. *Neural Networks*, 4(2):251 – 257, 1991.

[64] W P Hsieh, A S Lyons, E Pop, P Keblinski, and D G Cahill. Pressure tuning of the thermal conductance of weak interfaces. *PHYSICAL REVIEW B*, 84(184107), 2011.

[65] Ming Hu and Dimos Poulikakos. Si/ge superlattice nanowires with ultralow thermal conductivity. *Nano Letters*, 12(11):5487–5494, 2012. PMID: 23106449.

[66] Zhijun Hu, Mingwen Tian, Bernard Nysten, and Alain M. Jonas. Regular arrays of highly ordered ferroelectric polymer nanostructures for non-volatile low-voltage memories. *Nat. Mater.*, 8(1):62–67, 01 2009.

[67] Tran Doan Huan, Rohit Batra, James Chapman, Sridevi Krishnan, Lihua Chen, and Rampi Ramprasad. A universal strategy for the creation of machine learning-based atomistic force fields. *npj Computational Materials*, 3(1):37, 2017.

[68] William Humphrey, Andrew Dalke, and Klaus Schulten. Vmd: Visual molecular dynamics. *J. Mol. Graphycs*, 14(1):33–38, 1996.

[69] Scott T. Huxtable, Alexis R. Abramson, Chang-Lin Tien, Arun Majumdar, Chris LaBounty, Xiaofeng Fan, Gehong Zeng, John E. Bowers, Ali Shakouri, and Edward T. Croke. Thermal conductivity of si/sige and sige/sige superlattices. *Applied Physics Letters*, 80(10):1737–1739, 2002.

[70] Gareth James, Daniela Witten, Trevor Hastie, and Robert Tibshirani. *An Introduction to Statistical Learning*. 1431-875X. Springer-Verlag New York, 1 edition, 2013.

[71] H. Jiang and K. D. Jordan. Comparison of the properties of xenon, methane, and carbon dioxide hydrates from equilibrium and nonequilibrium molecular dynamics simulations. *J. Phys. Chem. C*, 114(12):5555–5564, 2010.

[72] William L. Jorgensen, David S. Maxwell, , and Julian Tirado-Rives. Development and testing of the opls all-atom force field on conformational energetics and properties of organic liquids. *J. Am. Chem. Soc.*, 118(45):11225–11236, 1996.

[73] Shin-Pon Ju, Meng-Hsiung Weng, Wen-Jay Lee, and Jenn-Sen Lin. Phonon spectra in ultrathin gold nanowire under stretching. *Computational Materials Science*, 42(4):595 – 599, 2008.

[74] Kalju Kahn and Thomas C. Bruice. Parameterization of opls–aa force field for the conformational analysis of macrocyclic polyketides. *J. Comput. Chem.*, 23(10):977–996, 2002.

[75] Katsuhiko Kanari and Takeo Ozawa. Thermal conductivity of epoxy resins cured with aliphatic amines. *Polym. J.*, 4(4):372–378, 05 1973.

[76] I. M. Khalatnikov. *Zh. Eksp. Teor. Fiz.*, 22(687), 1952.

[77] N. Khan and J. Li. Effects of compressive strain on optical properties of in x ga 1 x n ga n quantum wells. *APPLIED PHYSICS LETTERS*, 89(151916), 2006.

[78] Gota Kikugawa, Tapan G. Desai, Pawel Keblinski, and Taku Ohara. Effect of crosslink formation on heat conduction in amorphous polymers. *J. Appl. Phys.*, 114:034302, 2013.

[79] Gota Kikugawa, Taku Ohara, Toru Kawaguchi, Eiichi Torigoe, Yasumasa Hagiwara, and Yoichiro Matsumoto. A molecular dynamics study on heat transfer characteristics at the interfaces of alkanethiolate self-assembled monolayer and organic solvent. *J. Chem. Phys.*, 130(7):074706, 2009.

[80] G-H. Kim, L. Shao, K. Zhang, and K. P. Pipe. Engineered doping of organic semiconductors for enhanced thermoelectric efficiency. *Nat. Mater.*, 12(8):719–723, 08 2013.

[81] Gun-Ho Kim, Dongwook Lee, Apoorv Shanker, Lei Shao, Min Sang Kwon, David Gidley, Jinsang Kim, and Kevin P. Pipe. High thermal conductivity in amorphous polymer blends by engineered interchain interactions. *Nat. Mater.*, 14(3):295–300, 03 2015.

[82] Woochul Kim, Robert Wang, and Arun Majumdar. Nanostructuring expands thermal limits. *Nano Today*, 2(1):40 – 47, 2007.

[83] Hagen Klauk. Organic thin-film transistors. *Chem. Soc. Rev.*, 39:2643–2666, 2010.

[84] W. Knappe and O. Yamamoto. Effects of crosslinking and chain degradation on the thermal conductivity of polymers. *Colloid. Polym. Sci. (Kolloid-Zeitschrift und Zeitschrift für Polymere)*, 240(1-2):775–783, 1970.

[85] D. Konatham, D.V. Papavassiliou, and A. Striolo. Thermal boundary resistance at the graphene-graphene interface estimated by molecular dynamics simulations. *Chem. Phys. Lett.*, 527:47–50, 2012.

[86] Shenyu Kuang and J. Daniel Gezelter. Simulating interfacial thermal conductance at metal-solvent interfaces: The role of chemical capping agents. *J. Phys. Chem. C*, 115(45):22475–22483, 2011.

[87] E S Landry and A J H McGaughey. Thermal boundary resistance predictions from molecular dynamics simulations and theoretical calculations. *PHYSICAL REVIEW B*, 80(165304), 2009.

[88] Yann LeCun, Yoshua Bengio, and Geoffrey Hinton. Deep learning. *Nature*, 521(7553):436–444, 05 2015.

[89] Wu Li, Jesús Carrete, Nebil A. Katcho, and Natalio Mingo. Shengbte: A solver of the boltzmann transport equation for phonons. *Computer Physics Communications*, 185(6):1747 – 1758, 2014.

[90] X Li, K Maute, M L Dunn, and R Yang. Strain effects on the thermal conductivity of nanostructures. *PHYSICAL REVIEW B*, 81(245318), 2010.

[91] Zhenwei Li, James R. Kermode, and Alessandro De Vita. Molecular dynamics with on-the-fly machine learning of quantum-mechanical forces. *Phys. Rev. Lett.*, 114:096405, Mar 2015.

[92] Quanwen Liao, Zhichun Liu, Wei Liu, Chengcheng Deng, and Nuo Yang. Extremely high thermal conductivity of aligned carbon nanotube-polyethylene composites. *Sci. Rep.*, 5:16543, 11 2015.

[93] Michael L. Littman. Reinforcement learning improves behaviour from evaluative feedback. *Nature*, 521(7553):445–451, 05 2015.

[94] Dake Liu and C. Svensson. Power consumption estimation in cmos vlsi chips. *IEEE Journal of Solid-State Circuits*, 29(6):663–670, 1994.

[95] Jun Liu, Xiaojia Wang, Dongyao Li, Nelson E. Coates, Rachel A. Segalman, and David G. Cahill. Thermal conductivity and elastic constants of pedot:pss with high electrical conductivity. *Macromolecules*, 48(3):585–591, 2015.

[96] Jun Liu and Ronggui Yang. Length-dependent thermal conductivity of single extended polymer chains. *Phys. Rev. B*, 86:104307, Sep 2012.

[97] Xiangjun Liu, Gang Zhang, and Yong-Wei Zhang. Thermal conduction across graphene cross-linkers. *J. Phys. Chem. C*, 118(23):12541–12547, 2014.

[98] Yazhou Liu, Yanhui Feng, Zhi Huang, and Xinxin Zhang. Thermal conductivity of 3d boron-based covalent organic frameworks from molecular dynamics simulations. *J. Phys. Chem. C*, 120(30):17060–17068, 2016.

[99] Alejandro Lopez-Bezanilla and O. Anatole von Lilienfeld. Modeling electronic quantum transport with machine learning. *Phys. Rev. B*, 89:235411, Jun 2014.

[100] Tengfei Luo and John R. Lloyd. Non-equilibrium molecular dynamics study of thermal energy transport in au-sam-au junctions. *Int. J. Heat Mass Transfer*, 53:1–11, 2010.

[101] Easwar Magesan, Jay M. Gambetta, A. D. Córcoles, and Jerry M. Chow. Machine learning for discriminating quantum measurement trajectories and improving readout. *Phys. Rev. Lett.*, 114:200501, May 2015.

[102] Amy M. Marconnet, Namiko Yamamoto, Matthew A. Panzer, Brian L. Wardle, and Kenneth E. Goodson. Thermal conduction in aligned carbon nanotube–polymer nanocomposites with high packing density. *ACS Nano*, 5(6):4818–4825, 2011. PMID: 21598962.

[103] James E. Mark. *Physical Properties of Polymers Handbook*. Springer: New York, 2 edition, 2006.

[104] Stephen L. Mayo, Barry D. Olafson, and William A. Goddard. Dreiding: a generic force field for molecular simulations. *The Journal of Physical Chemistry*, 94(26):8897–8909, 1990.

[105] A J H McGaughey and M Kaviany. Phonon transport in molecular dynamics simulations: Formulation and thermal conductivity prediction. *ADVANCES IN HEAT TRANSFER*, 39:169–255, 2006.

[106] A.J.H. McGaughey and M. Kaviany. Thermal conductivity decomposition and analysis using molecular dynamics simulations. part i. lennard-jones argon. *International Journal of Heat and Mass Transfer*, 47(8):1783 – 1798, 2004.

[107] A.J.H. McGaughey and M. Kaviany. Phonon transport in molecular dynamics simulations: Formulation and thermal conductivity prediction. *Advances in Heat Transfer*, 39:169 – 255, 2006.

[108] Corey Melnick and Massoud Kaviany. Phonovoltaic. ii. tuning band gap to optical phonon in graphite. *Phys. Rev. B*, 93:125203, Mar 2016.

[109] B. Meredig, A. Agrawal, S. Kirklin, J. E. Saal, J. W. Doak, A. Thompson, K. Zhang, A. Choudhary, and C. Wolverton. Combinatorial screening for new materials in unconstrained composition space with machine learning. *Phys. Rev. B*, 89:094104, Mar 2014.

[110] Arden L. Moore and Li Shi. Emerging challenges and materials for thermal management of electronics. *Materials Today*, 17(4):163 – 174, 2014.

[111] Jonathan E. Moussa. Comment on "fast and accurate modeling of molecular atomization energies with machine learning". *Phys. Rev. Lett.*, 109:059801, Aug 2012.

[112] Florian Muller-Plathe and Wilfred F. van Gunsteren. Solvation of poly(vinyl alcohol) in water, ethanol and an equimolar water-ethanol mixture: Structure and dynamics studied by molecular dynamics simulation. *Polymer*, 38(9):2259–2268, 1997.

[113] V. Narayanamurti, H. L. Störmer, M. A. Chin, A. C. Gossard, and W. Wiegmann. Selective transmission of high-frequency phonons by a superlattice: The "dielectric" phonon filter. *Phys. Rev. Lett.*, 43:2012–2016, Dec 1979.

[114] B. Ni, T. Watanabe, and S. R. Phillpot. Thermal transport in polyethylene and at polyethylene–diamond interfaces investigated using molecular dynamics simulation. *J. Phys-Condens. Mat.*, 21(8):084219, 2009.

[115] Shūichi Nosé. A molecular dynamics method for simulations in the canonical ensemble. *Mol. Phys.*, 52(2):255–268, 1984.

[116] Timothy J. Ohara, Ravi Rajagopalan, and Adam Heller. Glucose electrodes based on cross-linked bis(2,2'-bipyridine)chloroosmium(+/2+) complexed poly(1-vinylimidazole) films. *Anal. Chem.*, 65(23):3512–3517, 1993.

[117] Wee-Liat Ong, Shubhaditya Majumdar, Jonathan A. Malen, and Alan J. H. McGaughey. Coupling of organic and inorganic vibrational states and their thermal transport in nanocrystal arrays. *J. Phys. Chem. C*, 118(14):7288–7295, 2014.

[118] Souvik Pal and Ishvar K Puri. Thermal rectification in a polymer-functionalized single-wall carbon nanotube. *Nanotechnology*, 25(345401):345401, 2014.

[119] T. Palacios, A. Chakraborty, S. Rajan, C. Poblenz, S. Keller, S. P. DenBaars, J. S. Speck, and U. K. Mishra. High-power algan/gan hemts for ka-band applications. *IEEE Electron Device Letters*, 26(11):781–783, 2005.

[120] H. Peelaers and C. G. Van de Walle. Effects of strain on band structure and effective masses in mos2. *PHYSICAL REVIEW B*, 86(241401(R)), 2012.

[121] Kris K. Perkin, Jeffrey L. Turner, Karen L. Wooley, and Stephen Mann. Fabrication of hybrid nanocapsules by calcium phosphate mineralization of shell cross-linked polymer micelles and nanocages. *Nano Lett.*, 5(7):1457–1461, 2005. PMID: 16178257.

[122] Amy M. Peterson, Robert E. Jensen, and Giuseppe R. Palmese. Reversibly cross-linked polymer gels as healing agents for epoxy-amine thermosets. *ACS Appl. Mater. Inter.*, 1(5):992–995, 2009. PMID: 20355883.

[123] G. Pilania, A. Mannodi-Kanakkithodi, B. P. Uberuaga, R. Ramprasad, J. E. Gubernatis, and T. Lookman. Machine learning bandgaps of double perovskites. 6:19375 EP –, 01 2016.

[124] Ghanshyam Pilania, Chenchen Wang, Xun Jiang, Sanguthevar Rajasekaran, and Ramamurthy Ramprasad. Accelerating materials property predictions using machine learning. 3:2810 EP –, 09 2013.

[125] S. Plimpton. Fast parallel algorithms for short-range molecular dynamics. *JOURNAL OF COMPUTATIONAL PHYSICS*, 117:1 to 19, 1995.

[126] Steve Plimpton. Fast parallel algorithms for short-range molecular dynamics. *J. Comput. Phys.*, 117(1):1–19, 1995.

[127] E. Pop, S. Sinha, and K. E. Goodson. Heat generation and transport in nanometer-scale transistors. *Proceedings of the IEEE*, 94(8):1587–1601, 2006.

[128] Xin Qian, Xiaokun Gu, and Ronggui Yang. Anisotropic thermal transport in organic-inorganic hybrid crystal -znte(en)0.5. *J. Phys. Chem. C*, 119(51):28300–28308, 2015.

[129] Paul Raccuglia, Katherine C. Elbert, Philip D. F. Adler, Casey Falk, Malia B. Wenny, Aurelio Mollo, Matthias Zeller, Sorelle A. Friedler, Joshua Schrier, and Alexander J. Norquist. Machine-learning-assisted materials discovery using failed experiments. *Nature*, 533(7601):73–76, 05 2016.

[130] A. Rahman, M. J. Mandell, and J. P. McTague. Molecular dynamics study of an amorphous lennard-jones system at low temperature. *J. Chem. Phys.*, 64(4):1564–1568, 1976.

[131] V. Rashidi, E. Coyle, J. Kieffer, and K. Pipe. Engineering thermal conductivity in polymer blends. In *APS Meeting Abstracts*, 2016.

[132] Vahid Rashidi, Eleanor Coyle, John Kieffer, and Kevin Pipe. Effects of vdw and electrostatic interactions on phonon velocity and thermal transport in polymers. volume 62, http://meetings.aps.org/link/BAPS.2017.MAR.L8.11, 2017.

[133] Vahid Rashidi, Eleanor J. Coyle, Katherine Sebeck, John Kieffer, and Kevin P. Pipe. Thermal conductance in cross-linked polymers: Effects of non-bonding interactions. *The Journal of Physical Chemistry B*, 121(17):4600–4609, 2017. PMID: 28362103.

[134] Vahid Rashidi and Kevin P. Pipe. Contributions of strain relaxation and interface modes to thermal transport in superlattices. *Comp. Mater. Sci.*, 107:151–156, 2015.

[135] Pramod Reddy, Kenneth Castelino, and Arun Majumdar. Diffuse mismatch model of thermal boundary conductance using exact phonon dispersion. *Applied Physics Letters*, 87(21):211908, 2005.

[136] Cuilan Ren, Wei Zhang, Zijian Xu, Zhiyuan Zhu, and Ping Huai. Thermal conductivity of single-walled carbon nanotubes under axial stress. *J. Phys. Chem. C*, 114(13):5786–5791, 2010.

[137] Andrew B. Robbins and Austin J. Minnich. Crystalline polymers with exceptionally low thermal conductivity studied using molecular dynamics. *Appl. Phys. Lett.*, 107(20):201908, 2015.

[138] Mark E. Roberts, Núria Queraltó, Stefan C. B. Mannsfeld, Benjamin N. Reinecke, Wolfgang Knoll, and Zhenan Bao. Cross-linked polymer gate dielectric films for low-voltage organic transistors. *Chem. Mater.*, 21(11):2292–2299, 2009.

[139] Miguel Munoz Rojo, Jaime Martin, Stephane Grauby, Theodorian Borca-Tasciuc, Stefan Dilhaire, and Marisol Martin-Gonzalez. Decrease in thermal conductivity in polymeric p3ht nanowires by size-reduction induced by crystal orientation: New approaches towards thermal transport engineering of organic materials. *Nanoscale*, 6:7858–7865, 2014.

[140] Conrad W. Rosenbrock, Eric R. Homer, GÃ!'bor CsÃ!'nyi, and Gus L. W. Hart. Discovering the building blocks of atomic systems using machine learning: application to grain boundaries. *npj Computational Materials*, 3(1):29, 2017.

[141] Matthias Rupp, Alexandre Tkatchenko, Klaus-Robert Müller, and O. Anatole von Lilienfeld. Fast and accurate modeling of molecular atomization energies with machine learning. *Phys. Rev. Lett.*, 108:058301, Jan 2012.

[142] Ja-Hyoung Ryu, Reuben T. Chacko, Siriporn Jiwpanich, Sean Bickerton, R. Prakash Babu, and S. Thayumanavan. Self-cross-linked polymer nanogels: A versatile nanoscopic drug delivery platform. *J. Am. Chem. Soc.*, 132(48):17227–17235, 2010. PMID: 21077674.

[143] Patrick K. Schelling, Simon R. Phillpot, and Pawel Keblinski. Comparison of atomic-level simulation methods for computing thermal conductivity. *Phys. Rev. B*, 65:144306, Apr 2002.

[144] T. Schneider and E. Stoll. Molecular-dynamics study of a three-dimensional one-component model for distortive phase transitions. *Phys. Rev. B*, 17:1302–1322, Feb 1978.

[145] T Schneider and E Stoll. Molecular-dynamics study of s three-dimensionsl one-component model for distortive pitsse trallsitions. *PHYSICAL REVIEW B*, 17(3):1302, 1978.

[146] Timothy F. Scott, Andrew D. Schneider, Wayne D. Cook, and Christopher N. Bowman. Photoinduced plasticity in cross-linked polymers. *Science*, 308(5728):1615–1617, 2005.

[147] Kevin C. See, Joseph P. Feser, Cynthia E. Chen, Arun Majumdar, Jeffrey J. Urban, and Rachel A. Segalman. Water-processable polymer-nanocrystal hybrids for thermoelectrics. *Nano Lett.*, 10(11):4664–4667, 2010. PMID: 20923178.

[148] Tian Long See, Rui Xing Feng, Cheuk Yu Lee, and Z.H. Stachurski. Phonon thermal conductivity of a nanowire with amorphous structure. *Computational Materials Science*, 59(Supplement C):152 – 157, 2012.

[149] Atsuto Seko, Tomoya Maekawa, Koji Tsuda, and Isao Tanaka. Machine learning with systematic density-functional theory calculations: Application to melting temperatures of single- and binary-component solids. *Phys. Rev. B*, 89:054303, Feb 2014.

[150] A A Selezeneva, A Y Aleinikova, P V Ermakova, N S Ganchuka, S N Ganchuka, and R E Jones. Moleculardynamics calculation of the thermal conductivity coefficient of the germanium single crystal. *PHYSICS OF THE SOLID STATE*, 54:462–467, 2012.

[151] Raymond B. Seymour. Plastics. *Ind. Eng. Chem.*, 58(8):61–73, 1966.

[152] Apoorv Shanker, Chen Li, Gun-Ho Kim, David Gidley, Kevin P. Pipe, and Jinsang Kim. High thermal conductivity in electrostatically engineered amorphous polymers. *Science Advances*, 3(7), 2017.

[153] Chen Shao, Yansha Jin, Kevin Pipe, Max Shtein, and John Kieffer. Simulation of crystalline and amorphous copper phthalocyanine: Force field development and analysis of thermal transport mechanisms. *J. Phys. Chem. C*, 118(19):9861–9870, 2014.

[154] M Shen, W J Evans, D Cahill, and P Keblinski. Bonding and pressure-tunable interfacial thermal conductance. *PHYSICAL REVIEW B*, 84(195432), 2011.

[155] Sheng Shen, Asegun Henry, Jonathan Tong, Ruiting Zheng, and Gang Chen. Polyethylene nanofibres with very high thermal conductivities. *Nat. Nano.*, 5(4):251–255, 04 2010.

[156] Wen Shi, Jianming Chen, Jinyang Xi, Dong Wang, and Zhigang Shuai. Search for organic thermoelectric materials with high mobility: The case of 2,7-dialkyl[1]benzothieno[3,2-b][1]benzothiophene derivatives. *Chemistry of Materials*, 26(8):2669–2677, 04 2014.

[157] Takuma Shiga, Daisuke Aketo, Lei Feng, and Junichiro Shiomi. Harmonic phonon theory for calculating thermal conductivity spectrum from first-principles dispersion relations. *Applied Physics Letters*, 108(20):201903, 2016.

[158] David J. Singh, Qiang Xu, and Khuong P. Ong. Strain effects on the band gap and optical properties of perovskite srsno3 and basno3. *APPLIED PHYSICS LETTERS*, 104(011910), 2014.

[159] Virendra Singh, Thomas L. Bougher, Annie Weathers, Ye Cai, Kedong Bi, Michael T. Pettes, Sally A. McMenamin, Wei Lv, Daniel P. Resler, Todd R. Gattuso, David H. Altman, Kenneth H. Sandhage, Li Shi, Asegun Henry, and Baratunde A. Cola. High thermal conductivity of chain-oriented amorphous polythiophene. *Nat. Nano.*, 9(5):384–390, 05 2014.

[160] G. SkoraczyÅski, P. Dittwald, B. Miasojedow, S. SzymkuÄ, E. P. Gajewska, B. A. Grzybowski, and A. Gambin. Predicting the outcomes of organic reactions via machine learning: are current descriptors sufficient? *Scientific Reports*, 7(1):3582, 2017.

[161] Kannan Srinivasan, Chris Pohl, and Nebojsa Avdalovic. Cross-linked polymer coatings for capillary electrophoresis and application to analysis of basic proteins, acidic proteins, and inorganic ions. *Anal. Chem.*, 69(14):2798–2805, 1997.

[162] F H Stillinger and T A Weber. Computer simulation of local order in condensed phases of silicon. *PHYSICAL REVIEW B*, 31(8):5262, 1985.

[163] E. T. Swartz and R. O. Pohl. Thermal boundary resistance. *Rev. Mod. Phys.*, 61(3):605–668, Jul 1989.

[164] William C. Swope, Hans C. Andersen, Peter H. Berens, and Kent R. Wilson. A computer simulation method for the calculation of equilibrium constants for the formation of physical clusters of molecules: Application to small water clusters. *The Journal of Chemical Physics*, 76(1):637–649, 1982.

[165] Chuanbing Tang, Erin M. Lennon, Glenn H. Fredrickson, Edward J. Kramer, and Craig J. Hawker. Evolution of block copolymer lithography to highly ordered square arrays. *Science*, 322(5900):429–432, 2008.

[166] John A. Thomas, Joseph E. Turney, Ryan M. Iutzi, Cristina H. Amon, and Alan J. H. McGaughey. Predicting phonon dispersion relations and lifetimes from the spectral energy density. *Phys. Rev. B*, 81:081411, Feb 2010.

[167] J. N. Tomlinson, D. E. Kline, and J. A. Sauer. Effect of nuclear radiation on the thermal conductivity of polyethylene. *Polym. Eng. Sci.*, 5(1):44–48, 1965.

[168] Søren Toxvaerd and Jeppe C. Dyre. Communication: Shifted forces in molecular dynamics. *J. Chem. Phys.*, 134(8), 2011.

[169] A. Tredicucci, C. Gmachl, F. Capasso, D.L. Sivco, A.L. Hutchinson, and A.Y. Cho. A multiwavelength semiconductor laser. *Nature*, 396(6709):350–353, 1998. cited By 85.

[170] Mikael Trollsås, Christian Orrenius, Fredrik Sahlén, Ulf W. Gedde, Torbjörn Norin, Anders Hult, David Hermann, Per Rudquist, Lachezar Komitov, Sven T. Lagerwall, and Jan Lindström. Preparation of a novel cross-linked polymer for second-order nonlinear optics. *J. Am. Chem. Soc.*, 118(36):8542–8548, 1996.

[171] Masayoshi Umeno, Takashi Egawa, and Hiroyasu Ishikawa. Gan-based optoelectronic devices on sapphire and si substrates. *Materials Science in Semiconductor Processing*, 4(6):459 – 466, 2001. papers presented at the ICMAT 2001 Symposium N:Materials for Opto electronics and High frequency Electronics applications.

[172] Ambroise van Roekeghem, Jesús Carrete, Corey Oses, Stefano Curtarolo, and Natalio Mingo. High-throughput computation of thermal conductivity of high-temperature solid phases: The case of oxide and fluoride perovskites. *Phys. Rev. X*, 6:041061, Dec 2016.

[173] Vikas Varshney, Soumya S. Patnaik, Ajit K. Roy, and Barry L. Farmer. Modeling of thermal conductance at transverse cnt-cnt interfaces. *J. Phys. Chem. C*, 114(39):16223–16228, 2010.

[174] Vikas Varshney, Soumya S. Patnaik, Ajit K. Roy, George Froudakis, and Barry L. Farmer. Modeling of thermal transport in pillared-graphene architectures. *ACS Nano*, 4(2):1153–1161, 2010. PMID: 20112924.

[175] R. Venkatasubramanian, E. Siivola, T. Colpitts, and B. O'Quinn. Thin-film thermoelectric devices with high room-temperature figures of merit. *NATURE*, 413:597–602, 2001.

[176] Xiaojia Wang, Victor Ho, Rachel A. Segalman, and David G. Cahill. Thermal conductivity of high-modulus polymer fibers. *Macromolecules*, 46(12):4937–4943, 2013.

[177] Zhaohui Wang, Jeffrey A. Carter, Alexei Lagutchev, Yee Kan Koh, Nak-Hyun Seong, David G. Cahill, and Dana D. Dlott. Ultrafast flash thermal conductance of molecular chains. *Science*, 317(5839):787–790, 2007.

[178] Logan Ward, Ankit Agrawal, Alok Choudhary, and Christopher Wolverton. A general-purpose machine learning framework for predicting properties of inorganic materials. 2:16028 EP –, 08 2016.

[179] Michael J. Waters, Katherine Sebeck, Eleanor J. Coyle, and Avi Bregman. Kirke. kieffer group, ann arbor, mi., 2012.

[180] Annie Weathers, Zia Ullah Khan, Robert Brooke, Drew Evans, Michael T. Pettes, Jens Wenzel Andreasen, Xavier Crispin, and Li Shi. Significant electronic thermal transport in the conducting polymer poly(3,4-ethylenedioxythiophene). *Adv. Mater.*, 27(12):2101–2106, 2015.

[181] J Welser, J L Hoyt, S Takagi, and J F Gibbons. Strain dependence of the performance enhancement in strained-si n-mosfets. *IEDM TECHNICAL DIGEST*, pages 373–376, 1994.

[182] T F Wietler, E Bugiel, and K R Hofmann. Residual strain in ge films grown by surfactant-mediated epitaxy on si(1 1 1) and si(0 0 1) substrates. *MATERIALS SCIENCE IN SEMICONDUCTOR PROCESSING*, 9:659–663, 2006.

[183] K. Wu, N. Sukumar, N. A. Lanzillo, C. Wang, Ramamurthy "Rampi" Ramprasad, R. Ma, A. F. Baldwin, G. Sotzing, and C. Breneman. Prediction of polymer properties using infinite chain descriptors (icd) and machine learning: Toward optimized dielectric polymeric materials. *Journal of Polymer Science Part B: Polymer Physics*, 54(20):2082–2091, 2016.

[184] Yanjun Xiao, Wenyan Wang, Ting Lin, Xijia Chen, Yutong Zhang, Jinghui Yang, Yong Wang, and Zuowan Zhou. Largely enhanced thermal conductivity and high dielectric constant of poly(vinylidene fluoride)/boron nitride composites achieved by adding a few carbon nanotubes. *J. Phys. Chem. C*, 120(12):6344–6355, 2016.

[185] Guofeng Xie, Yuan Guo, Baohua Li, Liwen Yang, Kaiwang Zhang, Minghua Tang, and Gang Zhang. Phonon surface scattering controlled length dependence of thermal conductivity of silicon nanowires. *Phys. Chem. Chem. Phys.*, 15:14647–14652, 2013.

[186] Xu Xie, Dongyao Li, Tsung-Han Tsai, Jun Liu, Paul V. Braun, and David G. Cahill. Thermal conductivity, heat capacity, and elastic constants of water-soluble polymers and polymer blends. *Macromolecules*, 49(3):972–978, 2016.

[187] Kai Xiong, Xiaohui Liu, Chuanwei Li, and Jianfeng Gu. Phonon instability of co single crystal in uniaxial tension and nanoindentation. *Computational Materials Science*, 99(Supplement C):47 – 56, 2015.

[188] Zhiping Xu and Markus J. Buehler. Nanoengineering heat transfer performance at carbon nanotube interfaces. *ACS Nano*, 3(9):2767–2775, 2009. PMID: 19702296.

[189] Osamu Yamamoto. Thermal conductivity of cross-linked polymers. *Polym. J.*, 2(4):509–517, 07 1971.

[190] Osamu Yamamoto and Hirotaro Kambe. Thermal conductivity of cross-linked polymers. a comparison between measured and calculated thermal conductivities. *Polym. J.*, 2(5):623–628, 09 1971.

[191] Chuanghua Yang, Zhongyuan Yu, Pengfei Lu, Yumin Liu, Han Ye, and Tao Gao. Phonon instability and ideal strength of silicene under tension. *Computational Materials Science*, 95(Supplement C):420 – 428, 2014.

[192] Nuo Yang, Gang Zhang, , and Baowen Li. Ultralow thermal conductivity of isotope-doped silicon nanowires. *Nano Lett.*, 8(1):276–280, 2008. PMID: 18095735.

[193] Shujiang Yang, Mohammed Lach-hab, Iosif I. Vaisman, and Estela Blaisten-Barojas. Identifying zeolite frameworks with a machine learning approach. *The Journal of Physical Chemistry C*, 113(52):21721–21725, 2009.

[194] Choongho Yu, Yeon Seok Kim, Dasaroyong Kim, and Jaime C. Grunlan. Thermoelectric behavior of segregated-network polymer nanocomposites. *Nano Lett.*, 8(12):4428–4432, 2008. PMID: 18959450.

[195] Seunggun Yu, Cheolmin Park, Soon Man Hong, and Chong Min Koo. Thermal conduction behaviors of chemically cross-linked high-density polyethylenes. *Thermochim. Acta*, 583:67–71, 2014.

[196] Haifei Zhan, Yingyan Zhang, John M. Bell, and Yuantong Gu. Suppressed thermal conductivity of bilayer graphene with vacancy-initiated linkages. *J. Phys. Chem. C*, 119(4):1748–1752, 2015.

[197] Hengji Zhang, Alexandre F. Fonseca, and Kyeongjae Cho. Tailoring thermal transport property of graphene through oxygen functionalization. *J. Phys. Chem. C*, 118(3):1436–1442, 2014.

[198] Lin Zhang, Teli Chen, Heng Ban, and Ling Liu. Hydrogen bonding-assisted thermal conduction in [small beta]-sheet crystals of spider silk protein. *Nanoscale*, 6:7786–7791, 2014.

[199] Teng Zhang and Tengfei Luo. Morphology-influenced thermal conductivity of polyethylene single chains and crystalline fibers. *J. Appl. Phys.*, 112(9):094304, 2012.

[200] Teng Zhang and Tengfei Luo. High-contrast, reversible thermal conductivity regulation utilizing the phase transition of polyethylene nanofibers. *ACS Nano*, 7(9):7592–7600, 2013. PMID: 23944835.

[201] Teng Zhang and Tengfei Luo. Role of chain morphology and stiffness in thermal conductivity of amorphous polymers. *J. Phys. Chem. B*, 120(4):803–812, 2016. PMID: 26751002.

[202] Teng Zhang, Xufei Wu, and Tengfei Luo. Polymer nanofibers with outstanding thermal conductivity and thermal stability: Fundamental linkage between molecular characteristics and macroscopic thermal properties. *J. Phys. Chem. C*, 118(36):21148–21159, 2014.

[203] Xiaoni Zhang, Sherry D. Ryan, Victor R. Prybutok, and Leon Kappelman. Perceived obsolescence, organizational embeddedness, and turnover of it workers: An empirical study. *SIGMIS Database*, 43(4):12–32, November 2012.

[204] Xing Zhang and Motoo Fujii. Measurements of the thermal conductivity and thermal diffusivity of polymers. *Polym. Eng. Sci.*, 43(11):1755–1764, 2003.

[205] Junhua Zhao, Jin-Wu Jiang, Ning Wei, Yancheng Zhang, and Timon Rabczuk. Thermal conductivity dependence on chain length in amorphous polymers. *J. Appl. Phys.*, 113(18):184304, 2013.

[206] Chongli Zhong, Qingyuan Yang, and Wenchuan Wang. Correlation and prediction of the thermal conductivity of amorphous polymers. *Fluid Phase Equilib.*, 181(1-2):195–202, 2001.

[207] Zhenxin Zhong, Matthew C. Wingert, Joseph Strzalka, Hsien-Hau Wang, Tao Sun, Jin Wang, Renkun Chen, and Zhang Jiang. Structure-induced enhancement of thermal conductivities in electrospun polymer nanofibers. *Nanoscale*, 6:8283–8291, 2014.

[208] Xiao Wang Zhou, Reese E. Jones, Christopher James Kimmer, John C. Duda, and Patrick E. Hopkins. Relationship of thermal boundary conductance to structure from an analytical model plus molecular dynamics simulations. *Phys. Rev. B*, 87:094303, Mar 2013.

[209] Maxim Ziatdinov, Artem Maksov, and Sergei V. Kalinin. Learning surface molecular structures via machine vision. *npj Computational Materials*, 3(1):31, 2017.